The Development of Low-Order Models for the Study of Fluid-Structure Interactions

Thesis by

Andrew A. Tchieu

In Partial Fulfillment of the Requirements

for the Degree of

Doctor of Philosophy

California Institute of Technology

Pasadena, California

2010

(Defended September 3, 2010)

Acknowledgments

First and foremost, I would like to thank my advisor, Professor Anthony Leonard. He is a beacon of kindness, has always been very supportive through all my endeavors, and genuinely cares for my overall wellbeing. I can say without any doubt that his guidance and encouragement helped me through many difficult times during my life. For that I am immensely indebted to him. It has been an honor to be his student and a part of him will forever be instilled in me.

I would also like to express gratitude to my thesis committee members, Professors Beverley McKeon, Tim Colonius, and Dale Pullin. I have had the pleasure to take courses from each one of them and all have had an important part in my academic development.

I also want to thank several Professors associated with Caltech. Professor John Dabiri has been inspiring and has taken the time to play on the Aero basketball team together with me among other things. Professors Hans Hornung and Joe Shepherd have always been very interactive with the members of our lab, constantly checking in to see how we are doing. In particular, I have had the privilege to play tennis with a great tennis player in Professor Hornung, who consistently outdueled me. Undoubtedly, he would have been a great tennis player if someone had not convinced him to study fluid mechanics. Thanks to Professor Darren Crowdy who gave me several ideas that contributed to the fourth chapter of this thesis. His enthusiasm for teaching has been contagious and I hope one day to replicate his passion in the classroom.

I am also grateful to have interacted with all members of the Iris and Puckett Laboratories. In particular, I met Hans Jonas as a visiting student in our lab, and he has been a great friend over the past few years.

My friends have been an unimaginably important part of my life. Perhaps the closest friends I

have and definitely the most influential during my experiences here at Caltech are my roommates. We have all shared many the same experiences and thoughts that have shaped my Ph.D. experience. Won Tae Joe and I come from the same background and had many profound conversations about school and life in this perspective. Jeff Hanna has been the person that I possibly spend the most time with here at Caltech, whether it be eating a lot of good food, drinking beer, or doing outdoor activities (mainly running or biking). Emily McDowell has been a very good friend and I cherish the dinners we have had talking about various things, both important and inconsequential. Dominic Rizzo has been a constant source of humor and entertainment. Thanks to all my other friends at Caltech, especially John Meier and Chris Kovalchick who I have had the pleasure of interacting with on and off campus, whether it be biking or just having a meal. I would also like to thank Francis Castillo and Kent Chau, who are two of my best friends from high school, for their support and friendship. You are all good friends and have shaped me to be who I am today, and I thank you from the bottom of my heart for being in my life.

I would also like to thank my girlfriend and best friend of all, Nancy Diep. I am the luckiest man in the world to have found my soul mate. She has been exceptionally supportive through all my mood swings while researching and writing my thesis. I will do everything in my power to make you the happiest woman in the world.

Last, but not least, I would like to thank my mom, dad, brother, and sister. They, above all, have been the most supportive throughout my whole education. When the times were rough, they were the ones constantly listening and comforting me while I was complaining and being dramatic. With their unconditional love and support, I was able to complete my Ph.D. degree. I love you all.

Abstract

In this work, several low-order models are derived to describe and simulate fluid-structure interaction problems with rigid bodies at a modest computational cost. The models are based on the inviscid flow assumption such that potential theory can be used with, in some cases, point vortices in the flow. Three general areas of application are considered. First, a thin airfoil undergoing small-scale unsteady motions in the presence of a freestream flow is investigated. The low-order model that is developed has only one ordinary differential equation for the fluid dynamic variables. This model is used to briefly investigate vortex-induced flutter in the attached-flow regime and control of a free-flying airfoil using synthetic jet actuators. Second, the vortex-induced vibrations of an arbitrary bluff body in the presence of vortices, with or without a freestream flow, are considered. Several examples of the canonical mass-spring-damper system for a circular cylinder and a flat plate are given to demonstrate the use of the vortex-based model for these applications. Finally, the two-body problem in a potential flow is addressed. A relatively simple solution specific to the doubly connected domain is determined and its resulting force and moment are coupled to the rigid bodies to investigate the mutual interactions between the two bodies. Aspects of drafting behind a forced body, the role of the fluid in elastic collision, and flapping flight are discussed in this context. Although a few specific examples and applications are given for each chapter, the main purpose of the thesis is to present low-order potential flow methods that are applicable to a variety of situations.

Contents

List of Figures

List of Tables

Chapter 1

Introduction

1.1 Motivation and background

Research of fluid-structure interaction (FSI) has been an increasing area of active research, especially with the ever-growing computational power of computers. Historically, the study of fluid dynamics and structural dynamics, except for isolated examples, have remained partitioned. Methods involving the study of fluid dynamics have relied on approaches where the fluid is treated without regard to the dynamics of the structure such that walls or boundaries are fixed or moving with a prescribed motion. Likewise, the study of structural dynamics has been, for the most part, studied without coupling to a fluid although all terrestrial structures are submersed in a fluid. Although, some information can be inferred using partitioned approaches, such as acquiring steady forces that a fluid applies on a structure and subsequently determining the structure's response, a coupled approach may be necessary to accurately describe, simulate, and analyze the FSI problem. When the fluid and structure are coupled through their mutual boundary conditions, the problem at hand becomes increasingly difficult and the resulting fluid and structural motion may not be obvious.

FSI is ubiquitous in nature and daily life. The fluid-structure coupling between many of these situations becomes crucial for the understanding of the phenomena and few examples are given here. The quintessential example of coupled FSI is the induced instability resulting in the collapse of the Tacoma Narrows Bridge in 1940. In this instance, von Kármán determined that the structural failure was coupled to the Kármán vortex street that was shed off the bridge and convinced the

governor of Washington to halt reconstruction in favor of redesigning of the bridge (von Kármán and Edson, 1967). It can be claimed that this event itself paved the path for the advent of new fields of study that include bridge aerodynamics and vortex-induced vibrations, which continue to be extremely active areas of research. Perhaps the oldest and most well studied FSI problem, the fluttering of airfoils has been studied for nearly a century due to the emergence of powered flight. Its stability boundaries have been determined based on assumptions of periodic response and potential flow assumptions (Theodorsen, 1935) yet there are still many more avenues for research.

In addition, FSI is important for a variety biological and naturally occurring situations. The fluttering of flags and falling cards/leaves have been a source of constant interest (Michelin et al., 2008, Eloy et al., 2007). In internal biological flows, the FSI of bi-leaflet mechanical heart valves is studied to show that aorta geometry has a drastic effect on the opening and closing of the leaflets (Borazjani et al., 2010, Eldredge and Pisani, 2008). Fluid-structure interactions have also been essential in the study of locomotion of various genus such as fish, insects, and birds to name a few (e.g. Triantafyllou and Triantafyllou, 1995). Moreover, the interactions of several bodies in proximity have been studied in an effort to understand coordinated motion and passive locomotion (Nair and Kanso, 2007, Kanso and Newton, 2009).

Since fluid-structure interactions are pervasive in everyday life, it is essential to distinguish when the coupling of fluid and solid motions is important for the solution of the problem. When the fluid and structure problems can be separated, the problem is drastically simplified which leads to computational savings. Consider a fluid-structure problem where a deformable structure is immersed in a fluid. There are time scales associated with the internal dynamics of the structure (e.g. elastic waves), the motion of the structure (e.g. period of a flutter oscillation), and motion of the fluid (e.g. vortex turnover time or convective time). If the time scale associated with internal dynamics is much smaller than both the time scales of the motions of the structure and the fluid, then the elastic effects of the structure can be neglected and the body can be modeled as being a rigid structure. Although the study of flexible structures is a major interest in general, this thesis is restricted to the study of fluid interaction with rigid bodies.

Now if the time scale of the structure's rigid body motion is much greater than that of the time scale of the fluid, then the fluid can be thought to be steady in the sense that the rate of change of the fluid is much faster than that of the rate of change of the structure's position and orientation such that the unsteady motion of the fluid can be neglected because its effect is nearly instantaneous. In this case, quasi-steady approximations can be used to determine forces and moments on the body or bodies in place of solving the entire unsteady motion of the fluid in detail. The goal of this thesis is to look at situations where this approximation cannot be made and thus the coupled problem of the fluid and structure must be explicitly treated and solved with an unsteady model.

In many instances described above an incompressible assumption can be made without loss of generality. Additionally, we can assume that the fluid is Newtonian so that the equations of motion for the FSI problem for K rigid bodies can be written as

$$\frac{\partial \mathbf{u}}{\partial \mathbf{t}} + \mathbf{u} \cdot \nabla \mathbf{u} = -\nabla p + \frac{1}{\text{Re}} \nabla^2 \mathbf{u} \tag{1.1a}$$

$$\nabla \cdot \mathbf{u} = 0 \tag{1.1b}$$

$$\frac{\mathrm{d}^2 \mathbf{x}_k}{\mathrm{d}t^2} = \mathcal{F}_k + \mathcal{F}_{\mathrm{e},k} \tag{1.1c}$$

$$\frac{\mathrm{d}^2 \boldsymbol{\theta}_k}{\mathrm{d}t^2} = \mathcal{T}_k + \mathcal{T}_{\mathrm{e},k} \tag{1.1d}$$

for each body $k = 1, 2, \ldots, K$ where $\mathbf{u}$ is the velocity, p is the pressure, and Re is the Reynolds number for the fluid. Each rigid body motion is completely chracterized by the location $\mathbf{x}_k$ and orientation $\boldsymbol{\theta}_k$. $\mathcal{F}_k$, $\mathcal{T}_k$, $\mathcal{F}_{\mathrm{e},k}$, and $\mathcal{T}_{\mathrm{e},k}$ are the force and torque due to the fluid (pressure and shear) and external forcing, respectively. $\mathcal{F}_k$ and $\mathcal{T}_k$ are not only functions of the fluid variables but are also implicitly functions of the solid variables themselves. The boundary conditions for rigid body motion are

$$\mathbf{u}(\mathbf{x}) = \frac{\mathrm{d}\mathbf{x}_k}{\mathrm{d}t} + \frac{\mathrm{d}\boldsymbol{\theta}_k}{\mathrm{d}t} \times (\mathbf{x} - \mathbf{x}_k), \text{ for } \mathbf{x} \in \partial D_k. \tag{1.2}$$

The most accurate method of predicting FSI of rigid bodies is to numerically solve equations (1.1) subject to boundary conditions (1.2). Although there are many techniques to simulate these

equations, two specific computational methods have been rather successful in the context of FSI. The first uses body fitted grids to determine the fluid motion. In the case of rigid body motion, the flow can be solved in a moving/rotating frame of reference for a single body (Wang, 2000). This cannot be said with the introduction of several bodies. The second method to solve for the flow is to use immersed boundary methods. Here a Lagrangian grid of the body is overlaid on top of the Eulerian grid that is used for the solution for the fluid motion. The boundary conditions are interpolated from the flow to the Lagrangian points and consequently a boundary forcing is required on the body and is essentially diffused to the fluid in order to enforce the boundary conditions. Although initially pioneered by Peskin (1972) there now exist various manifestations of this method (see Mittal and Iaccarino, 2005, Taira and Colonius, 2007, for a review of various methods). To simulate FSI for rigid bodies, both methods use a separate solver for the rigid body dynamics to partition the problem into two distinct parts for each time step. Due to this fact, an iterative method is used to ensure that the accelerations of the fluid and body are consistent, thus making the solution to the FSI problem prohibitively expensive. When the mass ratio of the body compared to the same mass of the displaced fluid is high, the numerical solutions of the fluid and rigid body dynamics can nearly decouple from each other such that the iterative solver is unnecessary and an explicit solver can be used in its place at a more modest computational expense. One must be careful about the strict stability requirements on the time step in this case (Alben, 2008). When mass-ratios are low (or even vanishing) however, special considerations are required to accelerate the iterative solver (Borazjani et al., 2008). These low mass-ratio cases are extremely important for the study of vortex-induced vibration of marine structures.

There are also several simplifications that can be made to reduce the computational expense that seems to limit the effectiveness of simulating FSI at higher Re. For high Re, the viscous effects can be neglected and thus equations (1.1) reduce to the incompressible Euler equations. This is equivalent to interpreting that the increasing Re essentially confines the boundary layer to an infinitesimally thin layer on the surfaces of the rigid bodies. Additionally, for structures with a long spanwise symmetry one can effectively reduce the three-dimensional problem to two dimensions as a decent

approximation. Even in cases where this is not strictly true some generalizations may quite possibly be inferred from the two-dimensional dynamics.

In irrotational flow the solution to the two-dimensional Euler equations can elegantly be recast in complex variables as determining an analytic complex potential, $W = \Phi + i\Psi$, such that $\mathbf{u} = \nabla\Phi$, where $\mathbf{u}$ satisfies the zero normal-velocity boundary conditions. Φ and Ψ are known as the velocity potential and streamfunction, respectively. This greatly simplifies the problem to using the linear superposition principle to add together individual elements of the flow. In the absence of vortex-like structures, the solution can be determined without the need of solving any ordinary differential equations. The most simple of these models is to use the potential to determine added-masses for the treatment of a single accelerating body (Lamb, 1945, Newman, 1977). The treatment of the FSI problem for this case in essence reduces to solving the rigid body dynamics equations with an "added" mass that modifies the accelerations of the body. In the single rigid body case, the added-mass is not time dependent. For several bodies, the coefficients are dependent on the instantaneous configuration with respect to each other and thus are a function of time and are considerably more difficult to treat (Kanso et al., 2005). A special case of the multiple body problem is studied in Chapter 4.

Additionally, quasi-steady models have been proposed in place of determining the unsteady flow around the bodies. The most prominent example of this is the use of the Kutta-Joukowski theorem to predict that the unsteady forces, $\mathcal{F}$, on a single body will be $\rho_{\mathrm{f}} U \Gamma_0$ where ρ_{f} is defined as the density of the fluid, U is the velocity associated with the body, and Γ_0 is the circulation around the body. The circulation itself must be determined either by applying a Kutta condition or using some empirical information. For example Lighthill (1973) predicts the lift due to the Weis-Fogh mechanism in insect flight using quasi-steady values of Γ_0.

However, one of the shortcomings of this method is that it does not capture the required unsteadiness in myriad situations where vortex-body interactions and vortex shedding are important phenomena. Ideal point vortices (i.e. point singularities of vorticity) provide an ample representation of pre-existing and shed vortices and are conveniently accommodating to the potential flow

representation. They can be easily added to the potential and in general require a solution of an ordinary differential equation to determine its motion. Even with the added complexity of introducing point vortices, the equations that represent the fluid in (1.1) are reduced to the solution of a finite number of ordinary differential equations as opposed to solving a partial differential equation as in the higher order methods presented above. Several studies have considered the body-vortex interaction in the context of dynamical systems and the transition to chaos (Borisov et al., 2005, Roenby and Aref, 2010). Shashikanth (2005) even reduced the general N-vortex, single-body problem to become Hamiltonian in structure under special circumstances.

In cases involving viscous separation a sufficient model must be developed to capture its salient features. For bodies with sharp edges, a quite natural model is to have the fictitious boundary layer separate from the edge and form a sheet-like structure of concentrated vorticity. The vortex sheet representation is first used by Clements (1973) to model flow separating from a square-based section. The method is more rigorously pursued recently by Jones (2003) and Shukla and Eldredge (2007) for fixed and flexible plates with prescribed motion. Unfortunately, the solution for the sheet strength usually involves a non-trivial solution to an integro-differential equation which for FSI must then be coupled to the equations of motion for the bodies (e.g. using the Birkhoff-Rott equations, see Saffman, 1992, Pullin, 1978). A more simple model that is conducive to limiting the number of fluid variables was previously proposed by Edwards (1954) and Brown and Michael (1954), among others, where the entire vortex sheet is fundamentally rolled into a single vortex. After several years, this method is then diligently employed to study and control some aspects of flow separation off a semi-infinite and finite plate (Cortelezzi and Leonard, 1993, Cortelezzi et al., 1994, Cortelezzi, 1995, 1996). Many of these techniques are also adopted and extended by Michelin and Smith (2009b) for use in several aspects of FSI.

The reduction of the problem to the use of discrete point vortices reduces the problem to solving several ordinary differential equations with algebraic constraints (e.g. Kutta condition, conservation of circulation). Because of the simple mathematical representation of the problem using discrete point vortices, standard methods can be used with little trouble to integrate the coupled FSI problem.

Chapters 2 and 3 specifically address the coupled FSI in the presence of pre-existing and shed vortices. Specifically, many characteristics of Chapter 3 are drawn from work of Cortelezzi (1992) and Michelin and Smith (2009b).

This thesis focuses on introducing several low-order methods for the FSI with rigid bodies that can be further used in a more rigorous manner to analyze and understand the stability and non-linear behavior of the system. For now, a few examples are given along with the methods to demonstrate the use of these techniques. The goal is to develop low-order models that describe several aspects of FSI but at very modest computational cost. For example, these methods are ideal for use in rapid prediction, optimization, and model-based feedback control design.

1.2   Thesis outline

This thesis is divided into three main chapters, each covering a distinctly different FSI situation with a specific low-order potential model to combat the problem. To this end, Chapters 2-4 can stand individually with little reference to one another. Although the author has made a modest attempt to keep the notation consistent between all chapters, there may be small discrepancies that may occur between them.

In Chapter 2 we derive a low-order model for a thin airfoil undergoing small-scale unsteady motions in the presence of a freestream flow. The method is additionally coupled to the rigid body dynamics and used to characterize some aspects of vortex-induced flutter. In addition, the model is extended to account for synthetic jet actuators to control the free flight of the airfoil.

Chapter 3 discusses the development of a model for the vortex-induced interactions of an arbitrary solid body with vortices either generated or pre-existing in the flow. This is specifically applied to interactions of bluff bodies in the presence of freestream. Two specific examples are given in the context of canonical vortex-induced vibration.

In Chapter 4 a method to handle the doubly connected two-body problem in a potential flow is derived. The method is then coupled with the motion of the bodies. This method is used to analyze the interaction of two cylinders due to the forcing of both, one, or neither of the cylinders. A second

example of two flat plates flapping is presented to demonstrate some aspects of unsteady bi-wing

flight.

Finally, in Chapter 5 we offer some concluding remarks and reiterate the main contributions of

this thesis. Several future directions of research are discussed for each specific model presented in

Chapters 2-4.

Chapter 2

A simple discrete-vortex model for the non-uniform motion and control of a thin airfoil

2.1   Introduction

Two-dimensional unsteady airfoil theory for incompressible flows has had a history that spans nearly a century. The primary motivation for this work stems from a long interest in the prediction of unsteady forces and moments for the control of aircraft and aeroelastic phenomena, for example the flutter of aircraft wings. Although two-dimensional potential theory is a major simplification over actual aerodynamics of thin bodies, it nevertheless gives insight into the underlying aerodynamic mechanism of unsteady aerodynamics. The simplifications in complexity lead to a tractable problem that can usually be handled by standard mathematical approaches and limited computing resources.

Because of the simplicity in two-dimensional potential theory, pioneering work was conducted by Wagner (1925) to predict the initial response of an airfoil impulsively started from rest. This work was extended by Glauert (1929) for predicting the force and moment on an oscillating airfoil, but was left unfinished until it was first published with a complete solution by Theodorsen (1935). Part of the general solution to the oscillatory problem is given by an analytical expression that relates the effect of wake circulation on an airfoil lift in the frequency domain by the aptly called, Theodorsen function. Similarly, several European researchers developed theories (Küssner, 1936, Kassner and Fingado, 1936). Garrick (1936) later showed that Wagner's indicial function is related

to the Theodorsen function through a Fourier transform. Jones (1938) soon developed an operational treatment for general airfoil motions in the Laplace plane based on on Fourier-integral superposition of linear results for simple harmonic motion. Concurrently, von Kármán and Sears (1938) also developed a more consistent method based on the integral equations resulting from a continuous vortex sheet and Sears (1941) applied the method to several applications. An effective and thorough review of the theories of Wagner, Theodorsen, Jones, and von Kármán theories can be found in Bisplinghoff et al. (1955).

More recently there has been renewed interest centered on using finite approximations of Wagner and Theodorsen functions. In particular, Edwards et al. (1979) derived generalized Theodorsen functions relating motions of the circulatory part of the airloads to the motion of the airfoil and applied it to subcritical and supercritical flutter conditions. Peters (2008) gives additional information on several finite state models predicting forces and moments in the frequency domain although one major drawback of these methods is that they cannot be integrated in a fully coupled simulation of the FSI. In addition, the models are rather mathematically complicated and in most cases are only manageable for prescribed or assumed oscillatory motions.

The goal of this chapter is to create a low-order model for arbitrary thin airfoil motion and show its efficacy in applications to various fluid-structure phenomena. Furthermore, this study addresses the introduction of synthetic jet actuators for which a new model can be implemented for the control of an airfoil. Because of this, it is chosen to use discrete vortices to model the mean effect of the actuators. First, a tractable and simple aerodynamic model is presented to predict the forces and moment on a thin airfoil undergoing arbitrary motions in the absence of any actuation. This model is reduced to the solution of a single non-linear ODE and is validated with both experimental results and detached-eddy simulation numerical testing. Next, using this simple model, the onset of vortex-induced flutter of plunging and pitching airfoils is examined. Specifically, several examples are given including one showing a multi-modal transient response. Lastly, the control of an airfoil with synthetic jet actuators is investigated more closely. An actuator model is created and compared to experimental results in an experimental apparatus that simulates free flight of an airfoil. A simple
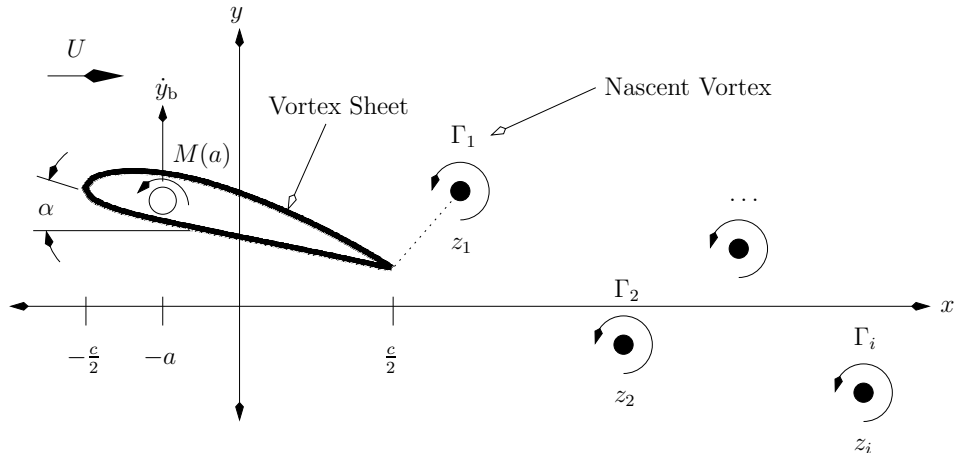
Figure 2.1: Schematic of the unsteady vortex dynamics model of an airfoil undergoing arbitrary motion in the presence of a freestream velocity. We note that the vortex strenghts Γ_i will have alternating sign although here they are depicted to clarify the convention that positive circulation results in a vortex that rotates in the counter-clockwise sense.

feedback scheme is then used to control the aforementioned vortex-induced vibrations highlighting one of many potential uses for the low-order model.

2.2 Aerodynamic model formulation

Here a model that is capable of predicting the forces and moments on a two-dimensional airfoil in motion is developed. The work in von Kármán and Sears (1938) lays the foundation of non-uniform motion of a thin airfoil by using the basic concepts of vortex theory available to an aeronautical engineer without much of the "unnecessary mathematical complications" that are commonly associated with the theories derived in the works of Theodorsen (1935) and Wagner (1925) among others. The theory presented here has been generalized to account for *any* airfoil motion as long as it remains small amplitude, as explained in Section 2.2.1, but closely follows the theory outlined in von Kármán and Sears (1938) to make it as concise and clear as possible.

Consider the incompressible flow around a thin airfoil of chord length c in a free-stream with an upstream velocity U_∞ that flows from left to right. The airfoil undergoes an arbitrary motion in both plunge and pitch defined by the body variables y_b and α, respectively. The pivot point for the rotational degree of freedom is located at $x = -a$ as shown in Figure 2.1. We model the unsteady
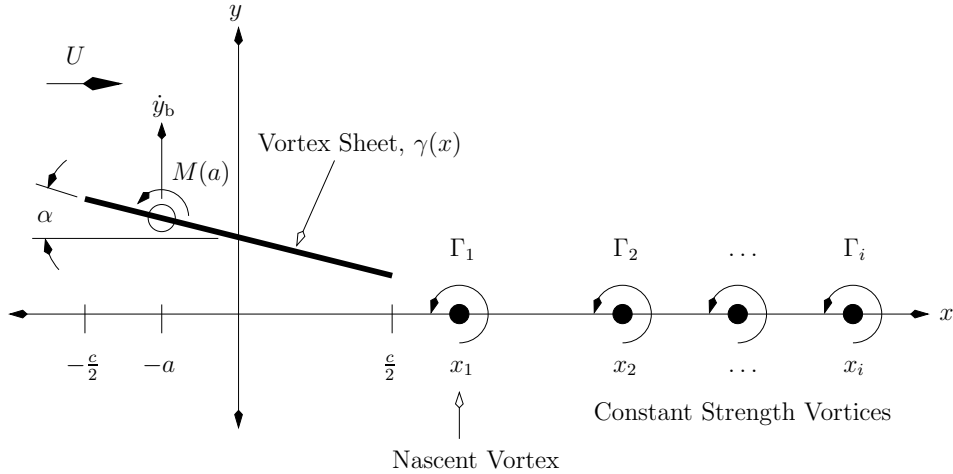
Figure 2.2: Schematic of the quasi one-dimensional simplification of Figure 2.2 after the application of assumptions given in Section 2.2.1.

motion of the airfoil by allowing the shear layer to separate into the wake as discrete and singular elements of vorticity with circulation strength Γ_j at location $z_j = (x_j, y_j)$.

2.2.1 Assumptions

Several assumptions are made so that a simple, closed-form, low-order model can be created to predict the forces and moment on a thin airfoil. The assumptions are listed and explained as follows:

1. The flow is considered high Reynolds number flow so that the boundary layer is sufficiently thin and the viscous effects can be neglected. Furthermore, it is reasonable to assume that the fluid remains irrotational except at the discrete points z_j. This allows us to use the potential flow description for the fluid. However, this leads to a conundrum since it is well known that forces and moments depend largely on the vortex-like structures that arise from viscous separation. Another view of the problem is to model the viscous boundary layer as an infinitesimally thin vortex layer, which is still a solution to the Euler equations, and allow this layer to separate into the flow at one or several discrete points (the details of separation are discussed in Section 2.2.4). This pseudo-viscous mechanism allows us to introduce inviscid vortex structures, whether represented by the sheet or several discrete point vortices, into the

flow while retaining the simplicity of the invicsid representation. The most natural separation point is at the trailing edge of the airfoil and in this research this point is chosen as the location where circulation is released into the fluid domain.

2. Motions of the thin airfoil are considered small-amplitude so that the leading-edge separation does not occur. This means that the characteristic motions must be $h/c \ll 1$ and $\dot{h}/U_\infty \ll 1$ where h is a characteristic length of the maneuver (in pitch this translates to $\alpha \ll 1$ and $\dot{\alpha}c/U_\infty \ll 1$ where the over-dot represents taking the time derivative of the quantity of interest). Even when this is not the case, evidence in Lewin and Haj-Hariri (2005) suggests that for a range of high frequency parameters (say with reduced frequency $k > 5$, where $k = 2\pi cf/U_\infty$ and f is the frequency of oscillation) the leading edge separation, although present, becomes reabsorbed into the boundary layer and subsequently separates off the trailing edge. The leading edge separation in these instances does not affect the lift and moment characteristics as severely as the trailing edge separation. In addition, the small-amplitude assumption allows another drastic reduction in complexity. For small-amplitude motions, the departure of any wake vortex elements in the transverse direction are considered small and thus the effect of its transverse motion can be justifiably neglected. Thus the wake vortex dynamics can be sufficiently restricted to their advection in a single dimension and the bound vorticity can be adequately restricted to lie on the x-axis.

3. It is assumed that the leading-order unsteadiness of the thin airfoil can be modeled by the motion of a flat plate. To take into account the effects of thickness and camber, the lift and moment are modified in a quasi-steady fashion, that is, steady characteristics versus angle of attack (AOA) are superimposed on the unsteady results for non-ideal airfoil shapes. This allows a general theory that is applicable to the entire class of thin airfoils with very minor modification using tabulated data, for instance, from Abbott and Deonhoff (1959).

These assumptions allow us to solve the drastically simplified problem depicted in Figure 2.2 where the flat-plate airfoil and its subsequent separated vortex elements now effectively lie on the

x-axis. The schematic given in Figure 2.2 is not entirely one-dimensional because the boundary condition is applied on the vertical velocity such that the bound circulation reads

$$\frac{1}{2\pi}\int_{-\frac{c}{2}}^{\frac{c}{2}}\frac{\gamma(s)}{x-s}\mathrm{d}s = v_{\mathrm{b}}(x) + v_{\mathrm{v}}(x), \text{ on } \frac{c}{2} < x < \frac{c}{2} \tag{2.1}$$

where the function v_{b} is the apparent vertical velocity due to the body motion and instantaneous AOA and v_{v} is the velocity induced by any shed vortices. Note that the integral equations for the sheet strength are evaluated in the principal value sense. Furthermore, if there are N discrete vortices in the wake at any time, the bound circulation can be decomposed into

$$\gamma(x) = \sum_{j}^{N}\gamma_j(x) + \gamma_{0,\mathrm{t}}(x) + \gamma_{0,\mathrm{r}}(x) \tag{2.2}$$

so that $\gamma_i(x)$ satisfies the boundary condition for an individual vortex in the wake, $\gamma_{0,\mathrm{t}}(x)$ satisfies the boundary condition due to plunging motion and the free-stream, and $\gamma_{0,\mathrm{r}}(x)$ satisfies the boundary condition solely due to rotation around its mid-chord, $x = 0$. It is also understood that the distributions are all functions of time since the problem is unsteady at heart. We have elected to drop the time dependence from the expressions for the bound circulation strengths understanding that they are indeed a function of time.

2.2.2 Bound vortex circulation

Consider a discrete wake vortex that has separated from the plate with circulation Γ_j located at $x = x_j$. The details of its creation will be addressed later in Section 2.2.4. From assumption 2 in Section 2.2.1, the vortex remains forever on the x-axis and only convects in the x-direction. The influence of this wake vortex on the airfoil will result in the creation of a distribution of circulation around the airfoil, $\gamma_j(x)$, to satisfy the boundary condition that no flow penetrates the plate, i.e.

$$\frac{1}{2\pi}\int_{-\frac{c}{2}}^{\frac{c}{2}}\frac{\gamma_j(s)}{x-s}\mathrm{d}s = \frac{\Gamma_j}{2\pi(x-x_j)}, \text{ on } \frac{c}{2} < x < \frac{c}{2}. \tag{2.3}$$

In addition, to uniquely determine a solution to the boundary value problem, we apply the Kutta condition (see Crighton (1985) and references therein for various manifestations), which in its simplest form states that the flow must leave the trailing edge of the airfoil smoothly. The application of the Kutta condition forces

$$\gamma_j \left(x = \frac{c}{2} \right) = 0 \tag{2.4}$$

and uniquely determines $\gamma_j(x)$.

The formula for the bound circulation density on the surface of the airfoil that satisfies both the boundary condition (2.3) and the Kutta condition (2.4) is found in von Kármán and Sears (1938) and is given as

$$\gamma_j(x) = \frac{\Gamma_j}{\pi(x_j - x)} \sqrt{\left(\frac{\frac{c}{2} - x}{\frac{c}{2} + x} \right) \left(\frac{x_j + \frac{c}{2}}{x_j - \frac{c}{2}} \right)}. \tag{2.5}$$

Equation (2.5) is derived by using conformal mapping and using the fact that the vortex lies on the x-axis. The amount of circulation bound to the airfoil due to this distribution is

$$\int_{-\frac{c}{2}}^{\frac{c}{2}} \gamma_j(x) \, \mathrm{d}x = \Gamma_j \left(\sqrt{\frac{x_j - \frac{c}{2}}{x_j + \frac{c}{2}}} - 1 \right). \tag{2.6}$$

Note that the circulation of both the vortex and its bound circulation gives a net circulation due to the enforcement of the Kutta condition. In comparison to other proposed methods, such as those given in Graham (1983), Cortelezzi (1996), and Michelin and Smith (2009b), the bound circulation presented here changes with position of the wake vortex. In these specific cases, the Milne-Thomson (1968) circle theorem is used to model the separation and this produces an exact opposite bound vortex on the body. When using the circle theorem, the strength of the nascent vortex is most easily determined by the explicit application of the Kutta condition since the conservation of circulation is automatically satisfied. Here we have chosen to model the separation such that each element satisfies the Kutta condition instead, and thus the conservation of circulation is applied to determine the

strength of the nascent vortex. This is just another example of the non-uniqueness in the treatment of potential flow problems. With the application of both the Kutta condition and conservation of circulation (discussed in Section 2.2.4) all approaches should yield identical results under the same assumptions.

2.2.3 Quasi-steady bound circulation

Airfoil translation and rotation lead to an additional term that is deemed the quasi-steady bound circulation about the airfoil. These circulation distributions due to airfoil motion are denoted $\gamma_{0,\text{t}}(x)$ and $\gamma_{0,\text{r}}(x)$ for "translation" and rotation, respectively, and represent associated circulation densities in the absence of wake vortices. For the "translational" term, a non-zero vertical velocity of the airfoil measured from the mid-chord, $\dot{y} - a\dot{\alpha} - U_\infty \sin \alpha$, must be matched by an equal fluid velocity to satisfy the no through-flow condition. Here the term "translational" is used loosely because the terms that have no x-dependence have been lumped together. In this specific boundary condition the free-stream component and additional rotational component are added, so that $\gamma_{0,\text{r}}(x)$ results from a pure rotational motion at the half chord, $x = 0$. Assuming the small angle approximation $\sin \alpha \approx \alpha$, we require $\gamma_{0,\text{t}}(x)$ to satisfy

$$\frac{1}{2\pi} \int_{-\frac{c}{2}}^{\frac{c}{2}} \frac{\gamma_{0,\text{t}}(s)}{x - s} \mathrm{d}s = \dot{y} - a\dot{\alpha} - U_\infty \alpha, \quad \text{on} - \frac{c}{2} < x < \frac{c}{2} \tag{2.7}$$

where the integral is taken using principal-value integration. We find that $\gamma_{0,\text{t}}(x)$, satisfying (2.7) and the Kutta condition, is

$$\gamma_{0,\text{t}}(x) = 2 \left(\dot{y} - a\dot{\alpha} - U_\infty \alpha \right) \sqrt{\frac{\frac{c}{2} - x}{\frac{c}{2} + x}} \tag{2.8}$$

from which we obtain the circulation moments

$$\Gamma_{0,\text{t}} = \int_{-\frac{c}{2}}^{\frac{c}{2}} \gamma_{0,\text{t}}(x) \, \mathrm{d}x = \pi c \left(\dot{y}_\text{b} - a\dot{\alpha} - U_\infty \alpha \right) \tag{2.9a}$$

$$\int_{-\frac{c}{2}}^{\frac{c}{2}} x\gamma_{0,\mathrm{t}}(x)\,\mathrm{d}x = -\frac{c}{4}\Gamma_{0,\mathrm{t}} \tag{2.9b}$$

$$\int_{-\frac{c}{2}}^{\frac{c}{2}} x^2\gamma_{0,\mathrm{t}}(x)\,\mathrm{d}x = \frac{c^2}{8}\Gamma_{0,\mathrm{t}}. \tag{2.9c}$$

Similarly, airfoil rotation about the mid-chord produces an airfoil velocity $-\dot{\alpha}x$ to be matched by a velocity induced by the circulation distribution $\gamma_{0,\mathrm{r}}(x)$. Thus it is required that

$$\frac{1}{2\pi}\int_{-\frac{c}{2}}^{\frac{c}{2}} \frac{\gamma_{0,\mathrm{r}}(s)}{x-s}\,\mathrm{d}s = -\dot{\alpha}x, \quad \text{on } -\frac{c}{2} < x < \frac{c}{2}. \tag{2.10}$$

The solution satisfying (2.10) and the Kutta condition is

$$\gamma_{0,\mathrm{r}}(x) = -2\dot{\alpha}\sqrt{\frac{c^2}{4} - x^2} \tag{2.11}$$

from which we obtain the moments

$$\Gamma_{0,\mathrm{r}} = \int_{-\frac{c}{2}}^{\frac{c}{2}} \gamma_{0,\mathrm{r}}(x)\,\mathrm{d}x = -\frac{\pi c^2 \dot{\alpha}}{4} \tag{2.12a}$$

$$\int_{-\frac{c}{2}}^{\frac{c}{2}} x\gamma_{0,\mathrm{r}}(x)\,\mathrm{d}x = 0 \tag{2.12b}$$

$$\int_{-\frac{c}{2}}^{\frac{c}{2}} x^2\gamma_{0,\mathrm{r}}(x)\,\mathrm{d}x = \frac{c^2}{16}\Gamma_{0,\mathrm{r}}. \tag{2.12c}$$

The total bound quasi-steady circulation can be found by adding (2.9a) and (2.12a) to obtain

$$\Gamma_0 = \Gamma_{0,\mathrm{t}} + \Gamma_{0,\mathrm{r}} = \pi c \left(\dot{y}_\mathrm{b} - \left(a + \frac{c}{4} \right)\dot{\alpha} - U_\infty\alpha \right). \tag{2.13}$$

2.2.4 Wake vortex dynamics

A few physical laws govern the wake vortex dynamics. First, the system must obey the conservation of total circulation (i.e. if the configuration starts with zero circulation at ∞ then it remains with

zero circulation) therefore we have

$$\Gamma_0 + \sum_{j=1}^{N} \Gamma_j \sqrt{\frac{x_j + \frac{c}{2}}{x_j - \frac{c}{2}}} = 0. \tag{2.14}$$

We recall that the total circulation due to a separated vortex and its associated bound circulation is not zero and therefore contributes the second term in 2.14.

Next, in point-vortex dynamics, the convection velocity of each vortex depends on the mutual influence of other vortices in addition to the influence of the body. Since the amplitudes of the motions are assumed to be small and at a low reduced frequency, the convection of a free vortex can be assumed to not be modified by the presence of other vortices. To first order this assumption leads us to model the motion of all but the most recent of the free vortices to move with speed U_∞, i.e.

$$\frac{\mathrm{d}x_j}{\mathrm{d}t} = U_\infty, \quad \text{for} j \geq 2. \tag{2.15}$$

The vortex nearest to the body (always indexed $j = 1$) is being fed circulation and moves with speed

$$\frac{\mathrm{d}x_1}{\mathrm{d}t} = U_\infty - \left(\frac{x_1^2 - \frac{c^2}{4}}{x_1 \Gamma_1} \right) \frac{\mathrm{d}\Gamma_1}{\mathrm{d}t} \tag{2.16}$$

where we have used a conservation of impulse argument to correct its motion due to the change in its circulation. This is much like the corrections that have been used in Brown and Michael (1954), Cheng (1954), Rott (1956), and more recently Cortelezzi (1992) and Michelin (2009), but in this one-dimensional analogue the correction gives an initial lift characteristic that agrees well with Wagner's impulsive start solution.

Naturally, since the flow is at high Reynolds number, the strength of the vortices can be assumed to remain constant except for the nascent vortex where its strength is being modified from the

separating shear layer originating from the trailing edge. For free vortices,

$$\frac{\mathrm{d}\Gamma_j}{\mathrm{d}t} = 0 \quad \text{for} j \geq 2, \tag{2.17}$$

i.e. Γ_j remains constant once it is released from the trailing edge. The strength of the nascent vortex is determined by the conservation of circulation. Therefore, from (2.14)

$$\Gamma_1 = -\sqrt{\frac{x_1 - \frac{c}{2}}{x_1 + \frac{c}{2}}} \left(\Gamma_0 + \sum_{j=2}^{N} \Gamma_j \sqrt{\frac{x_j + \frac{c}{2}}{x_j - \frac{c}{2}}} \right). \tag{2.18}$$

This now begs the question: when does a vortex become a free vortex? Since a vortex cannot "unwind," the magnitude of its circulation strength cannot ever decrease. This means that a vortex only gets stronger or equivalently that $\dot{\Gamma}_1$ does not change sign while the vortex is being fed circulation from the trailing edge. Say the rate $\dot{\Gamma}_1$ changes sign at $t = t_e$, then we model the physics by introducing a new vortex such that the discrete vortices get re-indexed as $\Gamma_{j+1}(t_e^+) = \Gamma_1(t_e^-)$ and $x_{j+1}(t_e^+) = x_1(t_e^-)$ after which the nascent vortex gets reinitialized as $\Gamma_1(t_e^+) = 0$ and $x_1(t_e^+) = \frac{c}{2}$.

2.2.5 Aerodynamic lift and moment

We derive the lift and moment from using the conservation of linear and angular impulse. The total fluid impulse in the y-direction, $\mathcal{I}_y$, is given by

$$\mathcal{I}_y = -\rho_\mathrm{f} \left(\int_{-\frac{c}{2}}^{\frac{c}{2}} x\gamma(x)\,\mathrm{d}x + \sum_{j=1}^{N} \Gamma_j x_j \right) \tag{2.19}$$

where $\gamma(x) = \gamma_j(x) + \gamma_{0,\mathrm{t}}(x) + \gamma_{0,\mathrm{r}}(x)$ is the total distribution of circulation about the airfoil and ρ_f is the fluid density. Using (2.5), (2.19) becomes

$$\mathcal{I}_y = -\rho_\mathrm{f} \left(\int_{-\frac{c}{2}}^{\frac{c}{2}} x\gamma_0(x)\,\mathrm{d}x + \sum_{j=1}^{N} \Gamma_j \sqrt{x_j^2 - \frac{c^2}{4}} \right). \tag{2.20}$$

The lift on the airfoil is defined as

$$L = -\frac{\mathrm{d}\mathcal{I}_y}{\mathrm{d}t}$$

$$= \rho_{\mathrm{f}} \frac{\mathrm{d}}{\mathrm{d}t} \int_{-\frac{c}{2}}^{\frac{c}{2}} x\gamma_0(x)\,\mathrm{d}x - \rho_{\mathrm{f}} U_\infty \Gamma_0 - \frac{\rho_{\mathrm{f}} U_\infty c}{2} \sum_{j=1}^{N} \frac{\Gamma_j}{\sqrt{x_j^2 - \frac{c^2}{4}}} \tag{2.21}$$

where we have used Equations (2.14)-(2.16) to remove time derivatives on Γ_j and x_j. The first term on the right-hand side of (2.21) leads to the so-called added mass terms due to airfoil acceleration, the second term is the quasi-steady lift, and the remaining sum represents the lift due to vortices in the near wake. In the absence of body motion, the lift due to the wake is a weakly decaying function that goes like $\mathcal{O}\left(1/t\right)$ as time increases. Upon substitution of (2.9), (2.12), and (2.13), Equation (2.21) becomes

$$L = \rho_{\mathrm{f}}\pi \left(-\frac{c^2}{4}\ddot{y}_{\mathrm{b}} - U_\infty c\,\dot{y}_{\mathrm{b}} + \frac{ac^2}{4}\ddot{\alpha} + U_\infty c \left(a + \frac{c}{4}\right)\dot{\alpha} + U_\infty^2 c\alpha \right) - \frac{\rho_{\mathrm{f}} U_\infty c}{2} \sum_{j=1}^{N} \frac{\Gamma_j}{\sqrt{x_j^2 - \frac{c^2}{4}}}. \tag{2.22}$$

Similarly, to derive an expression for the moment acting on the airfoil, the conservation of angular impulse is employed. The total angular impulse, $\mathcal{A}(s)$, at a distance s upstream of the mid-chord of the airfoil is given by

$$\mathcal{A}(s) = -\frac{\rho_{\mathrm{f}}}{2} \left(\int_{-\frac{c}{2}}^{\frac{c}{2}} (x+s)^2 \gamma(x)\,\mathrm{d}x + \sum_{j=1}^{N} \Gamma_j (s+x_j)^2 \right). \tag{2.23}$$

The counter-clockwise moment on the airfoil, $M(a)$, about the pivot point distance a upstream of the mid-chord is given by $\mathrm{d}\mathcal{A}(s)/\mathrm{d}t$ evaluated at $s = a$, where one must take into account that $\mathrm{d}s/\mathrm{d}t = -U_\infty$. Thus we find that

$$M(a) = \frac{\rho_{\mathrm{f}}}{2} \frac{\mathrm{d}}{\mathrm{d}t} \left(\int_{-\frac{c}{2}}^{\frac{c}{2}} x^2 \gamma(x)\,\mathrm{d}x + \sum_{j=1}^{N} \Gamma_j x_j^2 \right) + U_\infty \mathcal{I}_y + aL. \tag{2.24}$$

After substitution of and considerable algebraic manipulations using (2.9), (2.12), and (2.13), Equa-

tion (2.24) can be expressed as

$$M(a) = aL + \frac{\rho_f}{2} \frac{d}{dt} \int_{-\frac{c}{2}}^{\frac{c}{2}} \left(x^2 - \frac{c^2}{8} \right) \gamma_0(x) \, dx - \rho_f U_\infty \int_{-\frac{c}{2}}^{\frac{c}{2}} x \gamma_0(x) \, dx$$

$$+ \frac{\rho_f U_\infty c^2}{8} \sum_{j=1}^{N} \frac{\Gamma_j}{\sqrt{x_j^2 - \frac{c^2}{4}}} - \frac{\rho_f}{2} \left(\frac{\left(x_1^2 - \frac{c^2}{4} \right)^{\frac{3}{2}}}{x_1} \frac{d\Gamma_1}{dt} \right). \tag{2.25}$$

It is recommended to neglect the last term of this expression above to agree with the classical result that the lift force due to wake vorticity acts at the quarter-chord point of the airfoil with no additional moment. Recall that the conservation of impulse is used to derive the velocity of the nascent vortex. There are simply not enough variables to satisfy the conservation of y component of linear impulse, conservation of angular impulse, and the Kutta condition with the adjustment of a single vortex (three governing equations and two variables, Γ_1, x_1). Since we do not conserve the angular impulse we choose to ignore this last term to correct this oversight. Further applying Equations (2.9) and (2.12) to (2.25) yields

$$M(a) = aL + \rho_f \pi \left(\frac{U_\infty c^2}{4} \dot{y}_b + \frac{c^4}{128} \ddot{\alpha} - \frac{U_\infty a c^2}{4} \dot{\alpha} - \frac{U_\infty^2 c^2}{4} \alpha \right) + \frac{\rho_f U_\infty c^2}{8} \sum_{j=1}^{N} \frac{\Gamma_j}{\sqrt{x_j^2 - \frac{c^2}{4}}}. \tag{2.26}$$

Upon non-dimensionalizing Equations (2.22) and (2.26) the lift coefficient $C_L = 2L/(\rho_f U_\infty^2 c)$ is

$$C_L = \pi \left(-\frac{c}{2U_\infty^2} \ddot{y}_b - \frac{2}{U_\infty} \dot{y}_b + \frac{ac}{2U_\infty^2} \ddot{\alpha} + \frac{2a+c}{U_\infty} \dot{\alpha} + 2\alpha \right) - \frac{1}{U_\infty} \sum_{j=1}^{N} \frac{\Gamma_j}{\sqrt{x_j^2 - \frac{c^2}{4}}} \tag{2.27}$$

and the standard moment coefficient (with pitch up being positive) $C_M = -2M(a)/(\rho_f U_\infty^2 c^2)$ is

$$C_M(a) = -\frac{a}{c} C_L + \pi \left(-\frac{1}{2U_\infty} \dot{y}_b - \frac{c^2}{64U_\infty^2} \ddot{\alpha} + \frac{a}{2U_\infty} \dot{\alpha} + \frac{1}{2} \alpha \right) - \frac{1}{4U_\infty} \sum_{j=1}^{N} \frac{\Gamma_j}{\sqrt{x_j^2 - \frac{c^2}{4}}}. \tag{2.28}$$

Note well that when all time derivatives are negligible, we recover two classical results for steady aerodynamic theory. From the Equation (2.27) the steady state lift reduces to $C_{L,\infty} = 2\pi\alpha$. Furthermore, if the moment is measured about the quarter-chord, i.e. $a = \frac{c}{4}$, then the steady state

moment reduces to $C_{M,\infty}\left(a = \frac{c}{4}\right) = 0$.

2.2.6 Integration in time

One may notice that the integration of (2.16) and (2.18) is not straightforward due to the inherent singularity at $t = t_e$, the time at which a new nascent vortex is formed. To circumvent this problem, we outline a new strategy to determine x_j and Γ_j with no approximations. From the conservation of total circulation (2.14) we define a new variable

$$G(t) \equiv \Gamma_1 \sqrt{\frac{x_1 + \frac{c}{2}}{x_1 - \frac{c}{2}}} = -\Gamma_0 - \sum_{j=2}^{N} \Gamma_j \sqrt{\frac{x_j + \frac{c}{2}}{x_j - \frac{c}{2}}} \tag{2.29}$$

that can be considered known up to time t. In addition, (2.16) can be rearranged as

$$\frac{\mathrm{d}}{\mathrm{d}t}\left(\Gamma_1 \sqrt{x_1^2 - \frac{c^2}{4}}\right) = \frac{x_1 \Gamma_1 U_\infty}{\sqrt{x_1^2 - \frac{c^2}{4}}}$$

$$= \frac{x_1 G U_\infty}{x_1 + \frac{c}{2}}. \tag{2.30}$$

Defining

$$H(t) = \Gamma_1 \sqrt{x_1^2 - \frac{c^2}{4}} \tag{2.31}$$

Equation (2.30) can be written as

$$\frac{\mathrm{d}H}{\mathrm{d}t} = \frac{2H + cG}{2(H + cG)} G U_\infty \tag{2.32}$$

where (2.29) and (2.31) are used to rewrite

$$x_1 = \frac{2H + cG}{2G} \tag{2.33}$$

and

$$\Gamma_1 = G\sqrt{\frac{H}{H + cG}}. \tag{2.34}$$

Integrating (2.32) in place of (2.16) numerically is now straightforward. At every time step we check to see whether $\dot{\Gamma}_1$ changes sign, and if a creation event occurs, the integration returns to the previous time $t = t_e^-$ and creates a new vortex as described in Section 2.2.4.

2.2.7 Quasi-steady camber and thickness corrections

For non-idealized airfoils, Equations (2.27) and (2.28) must be adjusted to take into account the effects of a finite thickness and/or camber. These corrections can be modeled to be quasi-steady in the sense that the main source of unsteadiness originates from the fluid dynamics for a flat plate-like airfoil. For instance, in numerical experiments performed with a more sophisticated discrete vortex model the wake structure is nearly independent of the shape of the airfoil as long as the separation occurs at the trailing edge.

From experimental evidence, the steady state lift for a thin cambered airfoil is nearly $C_L \approx 2\pi\alpha$ in the attached flow regime (for several examples see the database in Abbott and Deonhoff (1959), pg. 449-670). As a result, the coefficient of lift is simply adjusted by its $\alpha = 0$ lift, $C_{L,0}$ to read

$$C_L' = C_{L,0} + C_L.$$

As for the moment, since the aerodynamic center is near the quarter-chord for thin airfoils, it can be assumed that the moment coefficient has no direct dependence on the AOA and therefore the coefficient of moment can simply be adjusted by its quarter-chord value to read

$$C_{M,\frac{c}{4}}' = C_{M,0} + C_{M,\frac{c}{4}}$$

where $C_{M,\frac{c}{4}} = C_M(a = \frac{c}{4})$.
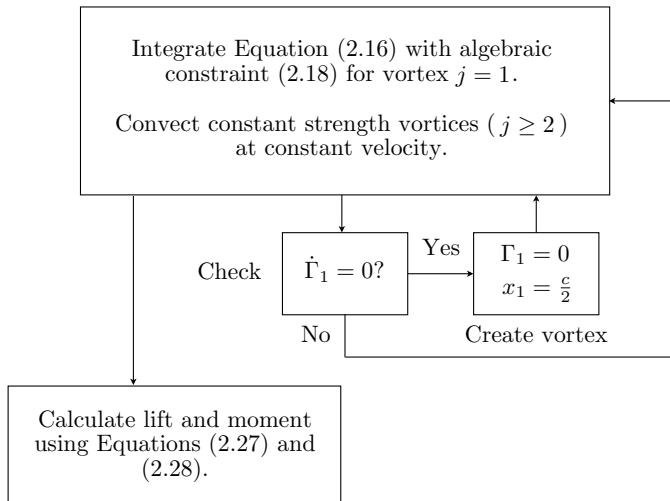
Figure 2.3: A block diagram summarizing the low-order model.

In what follows, the prime notation is dropped with understanding that we are dealing with the corrected values of lift and moment as presented above.

2.2.8   Summary of the low-order model

A block diagram summarizing the model is given in figure 2.3. To numerically simulate the model, only one ordinary differential equation for the nascent vortex velocity, (2.16), must be integrated with the constraint given by the conservation of circulation, (2.18). Equation (2.16) is replaced by (2.32) to circumvent the singularity resulting from the introduction of a new vortex at the trailing edge of the flat plate airfoil. All free vortices convect with constant strength and at the freestream velocity therefore the locations of these vortices are determined analytically. At every time step, one must check whether a new vortex is created based on the shedding criteria $\dot{\Gamma}_1 = 0$. If $\dot{\Gamma}_1$ changes sign, then a new vortex is formed, the simulation is reinitialized to account for the formation of a new vortex, and the simulation resumes. At any instant in time, the force and moment can be determined from Equations (2.27) and (2.28). If necessary, the lift and moment are modified to account for thickness and camber effects as discussed in Section 2.2.7.

(a)   (b)
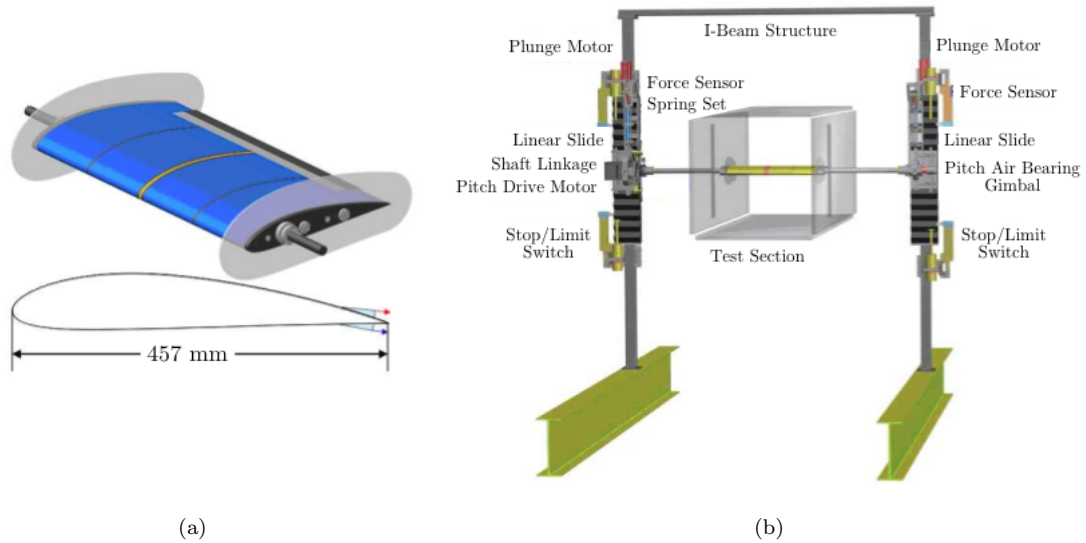
Figure 2.4: Depicted in (a) is the experimental model of the airfoil with modular synthetic jets attached and (b) is the experimental setup to allow for plunge and pitch control in an open-return wind tunnel facility at GTRI. Image is adapted from Muse et al. (2009).

2.3   Validation of the low-order model

The low-order model is compared to experimental results and numerical results of a NACA 4415 airfoil undergoing impulsive and sinusoidal pitch and plunge. This airfoil has been chosen primarily due to its use at Georgia Technical Research Institute (GTRI) in Atlanta as the test bed for current and future flow control experiments. The nominal values used here are $C_{L,0} = 0.4$ and $C_{M,0} = -0.1$.

2.3.1   Comparison with experiments

The experiments are conducted in an open-return low-speed wind tunnel having a square test section measuring 1 m on each side using a modular airfoil fitted with endplates to limit its three-dimensional effects. The airfoil model is depicted in Figure 2.4(a) and has a chord length of $c = 0.457$ m. The wind tunnel model executes commanded flight maneuvers in two-degrees of freedom (pitch about the quarter chord, $a = 0.25c$, and plunge) that can either be controlled by the combination of a torque motor and linear vertical slides as schematically drawn in Figure 2.4(b) or by synthetic jet actuators (as discussed in Section 2.5). Furthermore, the setup and control algorithms effectively remove the parasitic mass that comes from the necessary instrumentation. More information on the

experimental setup and its control strategy can be found in Muse et al. (2008b) and Muse et al. (2009).

For steady state measurements, the moment and lift are given by the torque motor and linear slide load cells. When steady, measurements of the moment and lift are accurate with less than 1% error. An extension to the unsteady case is made for accurate estimation of the instantaneous aerodynamic pitching moment and lift force during dynamic maneuvering. The moment is estimated by using the dynamics equation

$$M = I\ddot{\alpha} - \mathcal{T}_{e} \tag{2.35}$$

where I is the measured moment of inertia and $\mathcal{T}_{e} = K_{m}u_{m}$ is the commanded motor torque with K_{m} and u_{m} being the motor torque gain and command input to the controller, respectively. The moment of inertia is identified experimentally with less than 10% error. Angular acceleration $\ddot{\alpha}$ is measured with an angular accelerometer and its accuracy degrades with increasing pitching frequency and therefore limiting the pitching frequency to $f_{pitch} < 1$ Hz. Estimation of the aerodynamic lift can be done in a similar fashion but due to the several factors in the experimental design, the lift force is much less accurately measured and, like the moment, its accuracy degrades with increasing plunge frequency, f_{plunge}. Because of this, the plunge mechanism is locked to remove the effects of inertia and the lift force is measured directly from the load cell.

For the experimental test, the airfoil is pitched near quarter-chord at a free-stream Reynolds number, $Re = 9 \times 10^{5}$, with a prescribed trajectory,

$$\alpha = \alpha_{max} \sin\left(\frac{k_{pitch}U_{\infty}}{c}t\right) \tag{2.36}$$

where the amplitude, α_{max}, and reduced frequency, $k_{pitch} = \frac{2\pi c f_{pitch}}{U_{\infty}}$, are both functions of time. As seen in Figure 2.5(a), a sinusoidal chirp signal is fed into the experiment such that the reduced frequencies spanned range from $0.057 < k_{pitch} < 0.068$ ($0.60\,\mathrm{Hz} < f_{pitch} < 0.71\,\mathrm{Hz}$). The angular speed of the airfoil is kept constant. Given in Figure 2.5(b) is the comparison of lift and moment between the model and experimentally measured quantities. The agreement between the experimen-
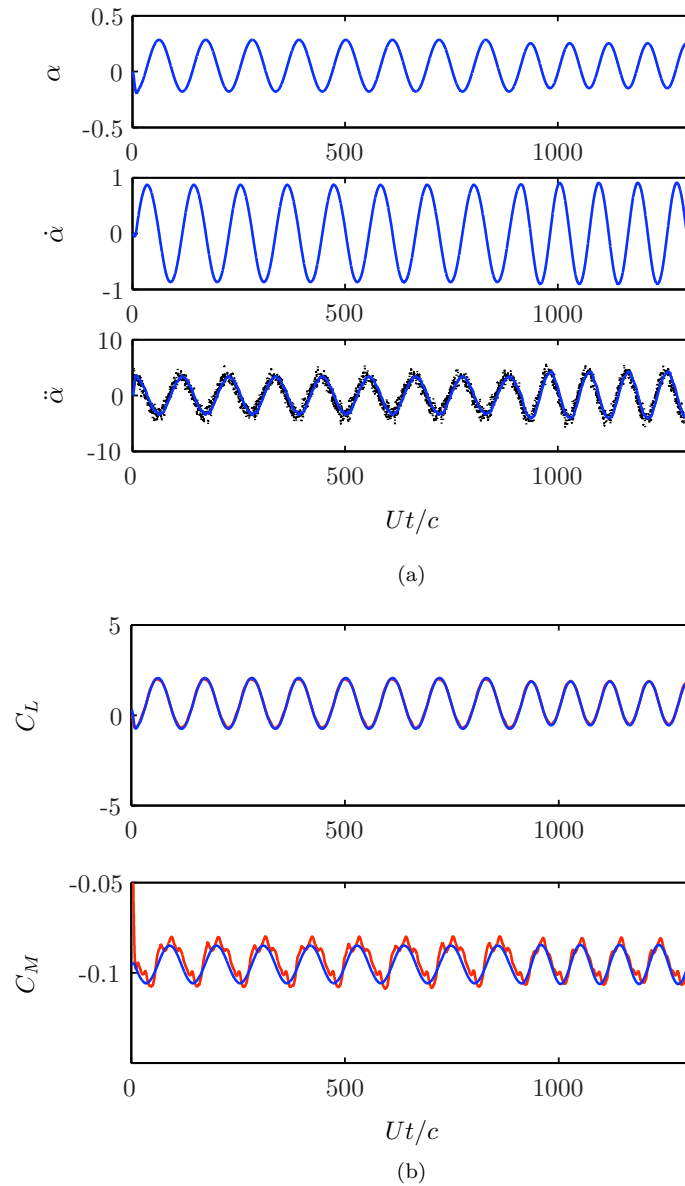
Figure 2.5: Comparison with experimental results for lift and moment for a NACA 4415 airfoil pitching about its quarter chord. (a) Input data (in radians) from experiment (dotted, unfiltered $\ddot{\alpha}$). Frequencies range from $0.057 < k_{\text{pitch}} < 0.068$ ($0.60\,\text{Hz} < f_{\text{pitch}} < 0.71\,\text{Hz}$). (b) Experimental and model response: —— current model; —— experiments. Experimental results for C_M were filtered with a Butterworth filter to remove high frequency noise. Experimental results for C_L are nearly identical to the model results (Tchieu et al., 2008).

Figure 2.6: Comparison with high fidelity numerical simulations for lift and moment for a NACA 4415 airfoil purely pitching about its quarter chord with $k_{\text{pitch}} = 1.256$ and $0° < \alpha < 2°$: ———, current model; ———, DDES.

tal measured lift and the model lift is excellent. The experimentally measured moment (low-pass filtered), shows slight departures from the model although the magnitude, frequency, and phase of the dominant mode of oscillation is very well predicted. The differences between the two might possible originate from the excessive noise in measuring the angular acceleration and using these results in Equation (2.35). The agreement seen here is typical for frequencies $f_{\text{pitch}} < 1Hz$.

2.3.2 Comparison with delayed detached-eddy numerical simulatons

Due to the limitations of the experimental facilities, numerical simulations are used to validate models in situations not realizable by experimentation. In particular, higher pitch and plunge rates are investigated. The numerical simulations presented here are computed at the University of Texas at Austin using delayed detached-eddy simulations (DDES) by Lopez (2009). The DDES scheme is a hybrid non-zonal Reynolds-averaged Navier-Stokes and large-eddy simulation scheme based on the detached-eddy simulation model. For more information on the simulation, see Lopez (2009). Simulations are run at a free-stream Reynolds number, Re $= 9 \times 10^5$, closely matching the conditions of the experiment.

Figure 2.6 shows the comparison between the numerical simulation and the low-order model
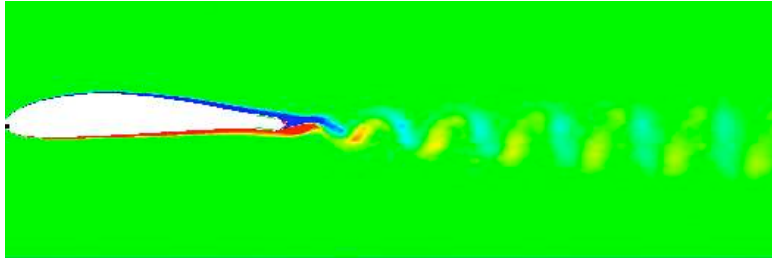
Figure 2.7: Vorticity field from DDES simulation demonstrating small-scale vortices shed off the non-sharp trailing edge (Lopez, 2009).

pitching sinusoidally at a fixed frequency, $k_{\text{pitch}} = 1.256$, which is more than two orders of magnitude higher than the experimental case. The agreement here is acceptable given the simplifications made. We notice that the simple low-order model cannot capture the small-scale oscillations that lie on top of the gross lift and moment signatures. These high frequency oscillations can be explained by vortex shedding off the non-sharp trailing edge in both the numerical simulations and the experiments (although the sensors lack the resolution to resolve this) as seen in Figure 2.7. This causes small amplitude von Kármán street to be shed from the trailing edge for all our operating conditions and typically introduces a small asymmetry in the small-scale waveform due to its turbulent nature. Of course, the low-order model cannot capture such an effect because of the prior assumptions made in Section 2.2.1, but the model does capture the salient features, primarily reproducing the lift and moment amplitudes, phase, and phase shift at the dominant frequency. The small-scale oscillations in this case are considered negligible because under the standard operating conditions, the variations in lift and moment due to the von Kármán street are $|\Delta C_L| < 0.05$ and $|\Delta C_M| < 0.01$ and at a frequency that is to high to garner a response when coupling with the fluid-structure interaction of the rigid structure.

Figure 2.8 similarly shows the comparison for a fixed plunge angular frequency where the airfoil heaves sinusoidally with an amplitude $h = \frac{y_{\text{b,max}}}{c} = 0.2$. Again, the same trend is seen where we have the small scale von Kármán shedding producing a small scale, high frequency signature in the lift and moment. The results are still quite satisfactory in producing the essential characteristics in the lift and moment due to the plunging motion.
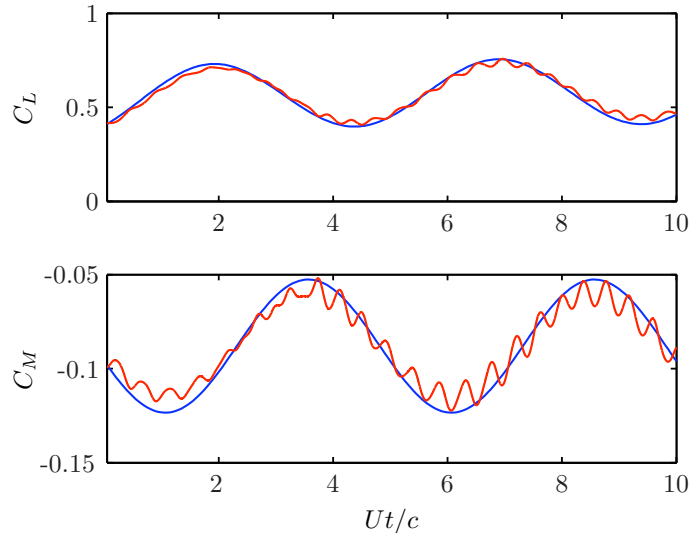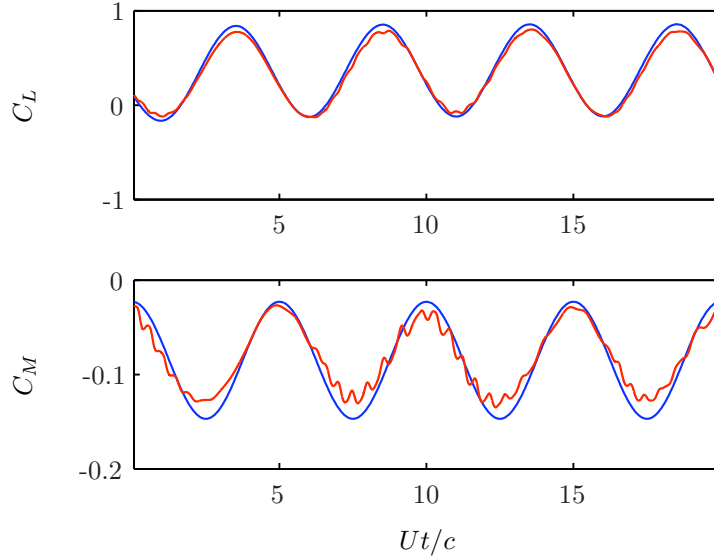
Figure 2.8: Comparison with high fidelity numerical simulations for lift and moment for a NACA 4415 airfoil purely pitching about its quarter chord with $k_{\text{plunge}} = 1.256$ and $h = 0.2$: ——, current model; ——, DDES.

2.4 Vortex-induced flutter of a simple two degree of freedom system

Consider a spring supported flat-plate wing section shown in Figure 2.9 with the a spring and damper acting in the y-direction (k_y, b_y) as well as in the angular direction (k_α, b_α). The model presented above is applied to simulate the onset of vortex-induced flutter in the attached flow regime. The dynamics of the system are modeled as

$$m_{\text{b}}^* \ddot{y}_{\text{b}}^* + S_x^* \ddot{\alpha} + b_y^* \dot{y}_{\text{b}}^* + k_y^* y_{\text{b}}^* = C_L \tag{2.37a}$$

$$I_\alpha^* \ddot{\alpha} + S_x^* \ddot{y}_{\text{b}}^* + b_\alpha^* \dot{\alpha} + k_\alpha^* \alpha = C_M(a) \tag{2.37b}$$

where the equations of motion are non-dimensionalized following Leonard and Roshko (2001) with

$$y_{\text{b}}^* = \frac{y_{\text{b}}}{c}, \ t^* = \frac{tU_\infty}{c}, \ m_{\text{b}}^* = \frac{m_{\text{b}}}{\frac{1}{2}\rho_{\text{f}}c^2}, \ I_\alpha^* = \frac{I_\alpha}{\frac{1}{2}\rho_{\text{f}}c^4}, \ S_x^* = \frac{S_x}{\frac{1}{2}\rho_{\text{f}}c^3},$$

$$b_y^* = \frac{b_y}{\frac{1}{2}\rho_{\text{f}}U_\infty c}, \ k_y^* = \frac{k_y}{\frac{1}{2}\rho_{\text{f}}U_\infty^2}, \ b_\alpha^* = \frac{b_\alpha}{\frac{1}{2}\rho_{\text{f}}U_\infty c^3}, \ k_\alpha^* = \frac{k_\alpha}{\frac{1}{2}\rho_{\text{f}}U_\infty^2 c^2}.$$
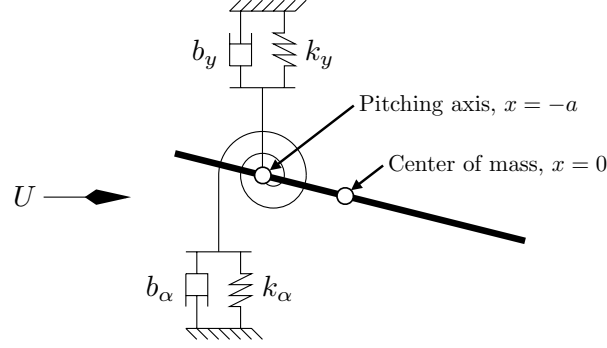
Figure 2.9: Schematic of the vortex-induced flutter of a flat plate airfoil. The point at which the spring-damper is attached is also the pitching axis (refer to Figure 2.2).

The static imbalance, S_x, results from a body not pitching about its center of mass and for a flat-plate wing section this can be reduced to $S_x = m_{\mathrm{b}} a$ assuming that the center of mass is near the mid-chord (Naudascher and Rockwell, 1994). Additionally, for a flat plate, the mass moment of inertia can also be analytically expressed as $I_\alpha = m_{\mathrm{b}} \left(a^2 + \frac{c^2}{12} \right)$. It is noted that non-dimensionalization in this fashion is different from the traditional formulation (for example see Williamson and Govardhan, 2004) but as explained in Klamo (2007) the non-dimensionalization with fluid dynamic parameters are compatible with the traditional formulation. In what follows the $(^*)$ is dropped with the understanding that all values are in their non-dimensional form.

Upon substitution of (2.21) and (2.26) into Equations (2.38) and (2.39), the motion of the airfoil is dictated by two additional ordinary differential equations

$$
\left(m_{\mathrm{b}} + \frac{\pi}{2} \right) \ddot{y}_{\mathrm{b}} + \left(b_y + 2\pi \right) \dot{y}_{\mathrm{b}} + k_y y_{\mathrm{b}} + \left(S_x - \frac{a\pi}{2c} \right) \ddot{\alpha}
$$
$$
+ \left(1 + \frac{2a}{c} \right) \pi \dot{\alpha} + 2\pi \alpha = -\frac{1}{U_\infty} \sum_{j=1}^{N} \frac{\Gamma_j}{\sqrt{x_j^2 - \frac{c^2}{4}}} \tag{2.38}
$$

$$
\left(S_x - \frac{a\pi}{2c} \right) \ddot{y}_{\mathrm{b}} + \left(\frac{c - 4a}{2c} \right) \pi \dot{y}_{\mathrm{b}} + \left(I_\alpha + \pi \left(\frac{1}{64} + \frac{a^2}{2c^2} \right) \right) \ddot{\alpha} + \left(b_\alpha + \frac{a\pi (4a + 3c)}{2c^2} \right) \dot{\alpha}
$$
$$
+ \left(k_\alpha + \frac{\pi (4a + c)}{2c} \right) \alpha = -\frac{1}{4U_\infty} \sum_{j=1}^{N} \frac{\Gamma_j}{\sqrt{x_j^2 - \frac{c^2}{4}}}. \tag{2.39}
$$

Equations (2.38) and (2.39) must be integrated with the model presented in Section 2.2 to give the

CASE	m_{b}	a/c	I_α	k_y	k_α
(a)	10	0.50	3.33	1	1
(b)	10	0.25	1.46	1	1
(c)	10	0.00	0.83	1	1
(d)	10	-0.25	1.46	1	1
(e)	1	0.25	1.46	1	1
(f)	100	0.25	1.46	1	1
(e)	100	0.50	33.33	100	100

Table 2.1: Legend and list of parameters for various cases presented in figures 2.10 and 2.11.

response of the system.

Although many studies revolve around determining the general stability of the system (e.g. the lowest $U_\infty = \tilde{U}_\infty$ such that the airfoil remains flutter free), due to the large parameter space, it is nearly impossible to come to any general conclusion. In particular, Bisplinghoff et al. (1955) could only draw a few generalizations after conducting several parametric studies using a fully periodic response assumption. In addition, the highly non-linear behavior of the wake vortices makes it difficult to determine a closed form solution to the problem such that a definitive stability analysis can be performed. Instead, the focus here is to look at a few key responses to highlight the transient and multi-modal behavior of vortex-induced flutter.

We take a look at undamped structures such that both b_y and b_α are set to zero. Typical aircraft structures have mass ratios $m_{\mathrm{b}} = \mathcal{O}(10 - 100)$ and stiffnesses, $k_\alpha = \mathcal{O}(0.1 - 100)$ and $k_y = \mathcal{O}(0.1 - 100)$.

Figure 2.10 gives several responses due to artificially induced gust in the y-direction with a list of parameters for these cases given in Table 2.1. The gust is modeled in the simulation by setting the initial condition $\dot{y}_{\mathrm{b}} = 0.05$, i.e. 5% of the free-stream velocity.

In cases (a)-(d), the pitching axis is gradually moved from the leading edge towards the trailing edge, thus also changing its mass moment of inertia, I_α. It is observed in 2.10(a) when held at the leading edge, the vibrations in the structure are stable for this set of parameters. As one moves back towards the quarter-chord, Figure 2.10(b), the oscillations are further suppressed. When the pitching axis is moved to the mid-chord and further, Figure 2.10(c) and 2.10(d), the configuration becomes unstable and for short times the model predicts an instability. Generally, if the center of
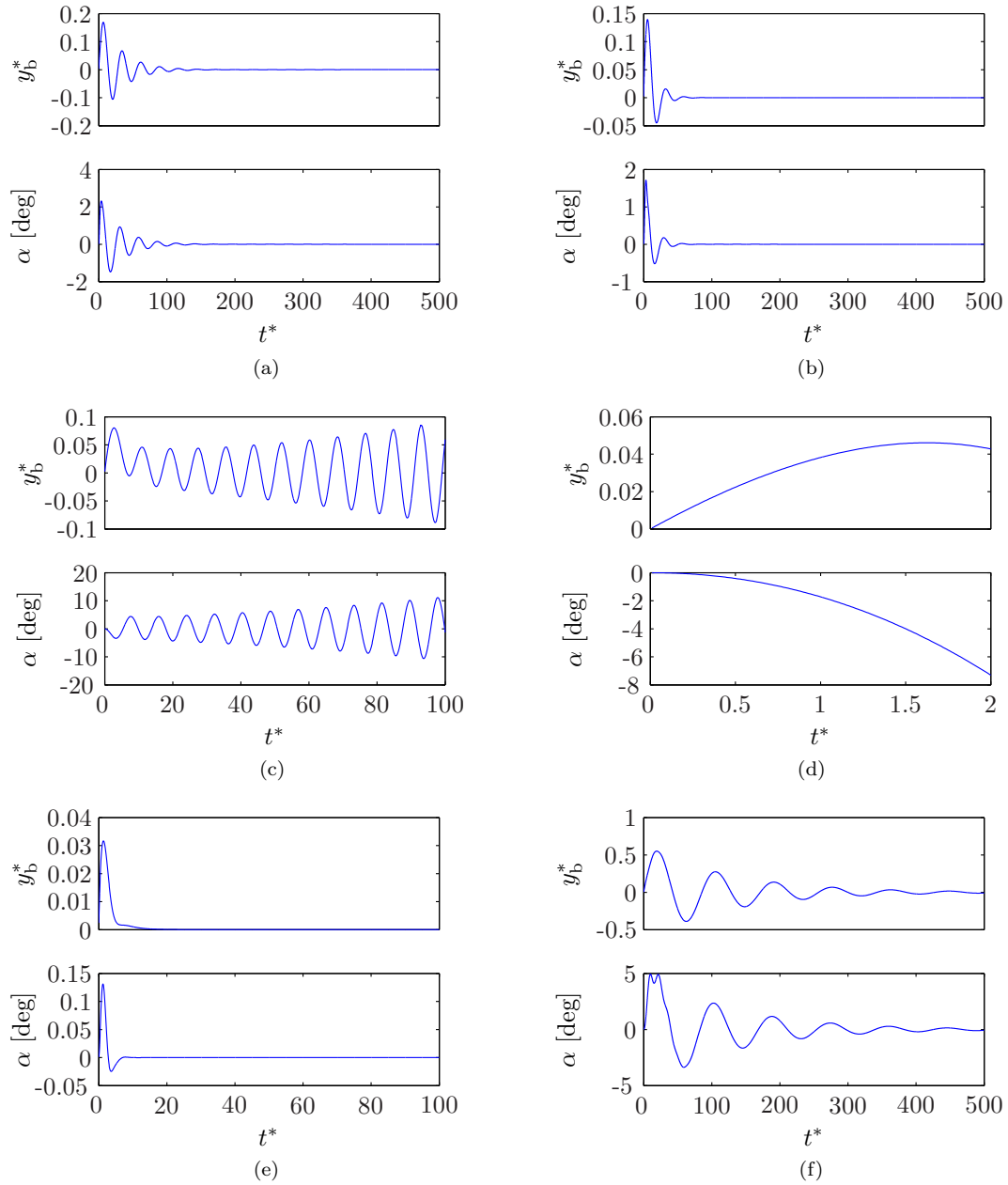
Figure 2.10: Various model simulations of vortex-induced flutter of a flat-plate airfoil. See table 2.1 for legend.
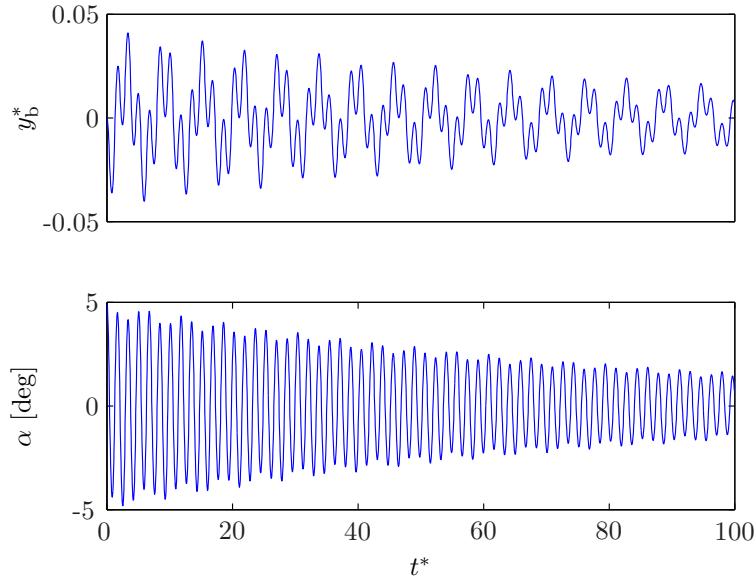
Figure 2.11: Case (e), a multi-modal response of a fluttering flat-plate airfoil with high stiffness. Structural parameters are $m = 100$, $a/c = 0.5$, $I_\alpha = 33.3$, $k_y = 100$, $k_\alpha = 100$.

mass of the airfoil lies behind the pitching axis, the system is stable, more so near the quarter-chord.

As an example, in figures 2.10(e) and 2.10(f), the mass ratios are adjusted. For a $m_b = 1$, the oscillations disappear as the wake dynamics act in such a way that nullifies the motion of the airfoil when compared to Figure 2.10(b). On the other hand, when the mass ratio is increased as in 2.10(f), the oscillations seem to become larger and more persistent possibly because the wake cannot produce large enough forces and moments to counteract the inertia of the system since the both systems are initialized with the same "gust" vertical velocity.

It is interesting to note that in cases (a)-(f), there seems to be only one dominant frequency (dependent on the input parameters) which is typically greater than the natural frequency of the bending mode and below the natural frequency of the torsion mode. Because of this, the use of analyses that assume a single frequency for the combined bending-torsion mode can be used to investigate the stability of fluttering airfoils (Bisplinghoff et al., 1955). For more stiff structures, as seen in Figure 2.11, the response may include two frequencies. As the body becomes increasingly stiff, the body begins to oscillate near the natural frequency of the bending mode ($f^* = 0.17$) as well as the frequency of the torsion mode ($f^* = 0.59$). The existence of two frequencies can be clearly seen by taking a look at the frequency content of y_b in Figure 2.12. This is due to the coupling
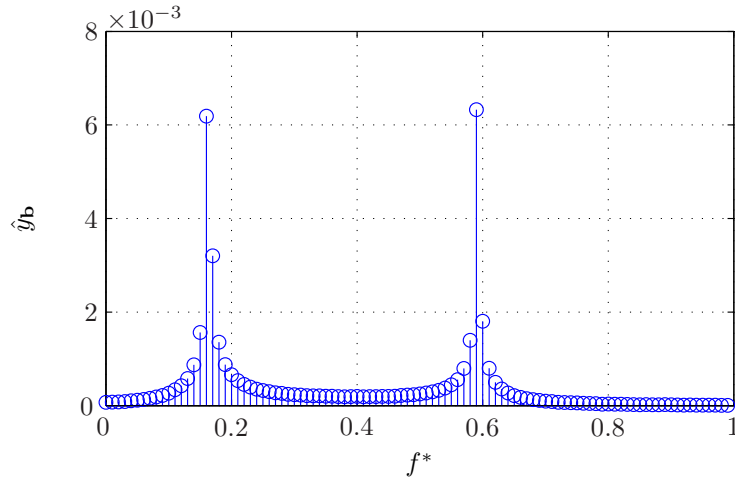
Figure 2.12: FFT of the response in Figure 2.11 plotted versus non-dimensional frequency.

between the two modes. Pitching downward (upward) causes the airfoil to dive (rise) accordingly therefore the pitching mode is apparent in the plunging response (which is not a sub-harmonic of the primary plunge mode).

2.5 Control of a two-dimensional airfoil

Here we make a closer investigation of the setup at GTRI of free-flying NACA 4415 airfoil outfitted with synthetic jet actuators to allow for in flight maneuvering. The current model is extended and applied to control the motions of the airfoil. The experiments are conducted by Muse et al. (2009) with aid from the thesis author in all experiments presented in this chapter.

2.5.1 Setup

The airfoil is controlled unconventionally and solely by synthetic jet actuators that span the entire wing at a specific chord location. A synthetic jet actuator consists of a cavity where one side comprises of a piezo-electric membrane that vibrates at a specific frequency that is proportional to the input voltage to cause a pulsed jet exiting the orifice on the opposite side of the membrane. This produces a zero-mass jet that carries momentum in the direction of its orientation and thus the device does not require a supplying reservoir of fluid (Smith and Glezer, 1998, Glezer and Amitay,

2002). A majority of research associated with synthetic jets revolves around controlling separation over bluff bodies or airfoils at high AOA (Amitay, 2000). It is claimed in Amitay and Glezer (2002) that the use of synthetic jets at frequencies more than an order of magnitude higher than the natural frequency can completely reattach the flow on stalled airfoils at moderate AOA with a relatively small momentum injection, although some propose that this is due to an unintentional tripping of the boundary layer (Greenblatt and Wygnanski, 2000). More recently, synthetic jets are used in the low AOA regime to virtually shape the airfoil to give it better aerodynamic characteristics for control authority (Glezer, 2005). This specific application shows promise in providing a substantial change in lift and moment by trapping small pockets of vorticity near the trailing edge (DeSalvo and Glezer, 2004, 2005). This control technique provides an alternative to using conventional control surfaces such as ailerons and elevators in the attached flow regime. The resulting effect is modeled in this section.

For this specific configuration, actuators are placed both on the suction (SS) and pressure side (PS) of the airfoil. We fix the location of the actuators at $x_{\mathrm{C}}/c = 0.45$ measured from the mid-chord for both the SS and PS actuators. Since the synthetic jet actuators are distributed equally along the airfoil's span, it is assumed that the spanwise effect is such that the synthetic jets can be considered two-dimensional although there are slight departures from this seen in experiments.

2.5.2 Modeling ZMF synthetic jet actuators

Figure 2.13 shows a plot of the normalized vorticity for a synthetic jet acting at a location near the leading edge of a modified circular arc airfoil with an oncoming freestream velocity from a prior experiment (Glezer and Amitay, 2002). The airfoil consists of a circular cylinder with two flat sections forming the trailing edge of the airfoil. The field of view of the particle-image velocimetry window is shown by the inset and is zoomed in near the leading edge of the airfoil. In particular, Figure 2.13(c) shows that the time-averaged field exhibits a noticeable concentration of clockwise vorticity that appears to be "trapped" in the time-averaged-sense (i.e. the time-scale relevant to the flow) immediately following the actuator downstream. This trapped vorticity is modeled as
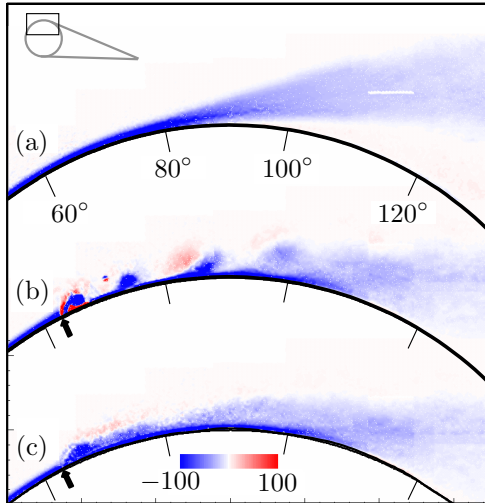
Figure 2.13: Normalized vorticity plots at non-dimensional forcing frequency of $St_{\text{act}} = 4.0$ and non-dimensional momentum coefficient $C_\mu = 5.1 \times 10^{-2}$ over the leading edge of a modified circular arc airfoil for (a) the baseline case, (b) phased-averaged, and (c) time-averaged (Glezer and Amitay, 2002). The arrow indicates the location of the synthetic jet actuator. The window of the field of view is given by the inset image.

a macro vortex element that is held stationary to represent the localized confinement observed in experiments. Thus we place a control vortex located at $x = x_{\text{C}}$ to reproduce the effect of the actuator. When the SS actuator is turned on, a negative (clockwise) vortex is formed. When the PS actuator is turned on, a positive vortex is formed. The circulation of the control vortex depends on the control variable, u_{C}, for example,

$$\frac{d\Gamma_{\text{C}}}{dt} = J(u_{\text{C}}, \Gamma_{\text{C}}).$$

From recent experiments, it seems as though the formation time of the control vortex is much less that the convective time scale, then the control vortex follows the functional form, $\Gamma_{\text{C}} = \Gamma_{\text{C}}(u_{\text{C}})$, with a possible dependence on the AOA as well. The determination of this function will be addressed in Section 2.5.3. In addition to this, the near trailing edge region slightly violates the Kutta condition as seen in both computations and experiments. Given in Figure 2.14(a) is a recent DDES computation from Lopez (2009). Not only is the airfoil pressure affected by the actuator device, but it also experiences shift near the trailing edge that affects the global pressure distribution around the airfoil. Note that the peaks around $2x/c \approx 0.6$ in the computational result are due to the actuator
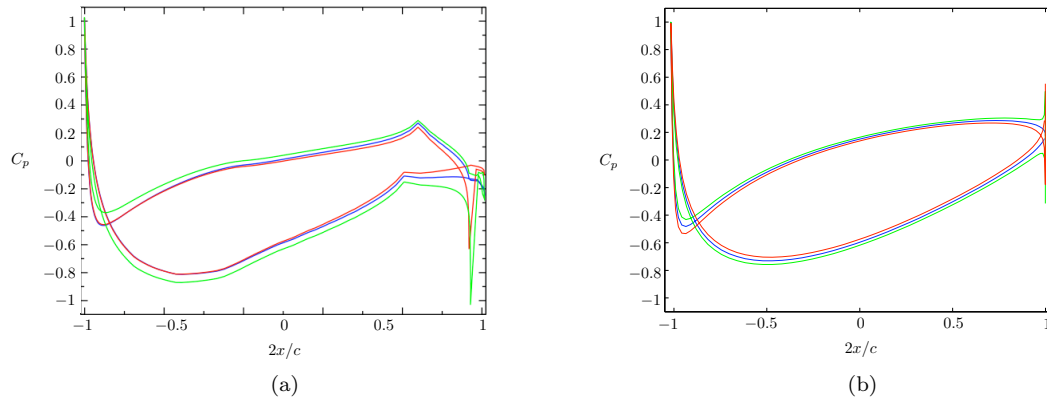
Figure 2.14: Numerical and theoretical evidence for shift in Kutta condition for an airfoil at $\alpha = 8°$. (a) The shift in Kutta condition as seen numerically from Lopez (2009). (b) The theoretical shift in Kutta condition for a Joukowski airfoil. Legend: ——— , baseline case, no actuation; ——— , suction side actuation turned on; ——— , pressure side actuation turned on.

geometry and remained unmodeled since their effect does not change the lift and moment drastically. In Figure 2.14(b) an added bound circulation is added to the Kutta condition to cause a similar effect although it violates the requirement that there should be a stagnation point at the trailing edge. It is found necessary to add an additional bound circulation such that the Kutta condition is shifted slightly to match the computational and experimental results.

The distribution of circulation on the airfoil to satisfy these constraints can be written as

$$\gamma_{\mathrm{C}}(x) = \Gamma_{\mathrm{C}}\delta(x - x_{\mathrm{C}}) + \frac{\epsilon\Gamma_{\mathrm{C}}}{\pi\sqrt{\frac{c^2}{4} - x^2}} \tag{2.40}$$

where ϵ is a fitting parameter. Note that this point distribution of circulation on the airfoil represented by the first term violates the necessary boundary conditions, but its effect is small since the size of the vortex is also small. The effect of the actuation is local and it can be argued that it locally changes the near boundary condition as well. The second term adds a uniform rotation of the flow that slightly shifts the Kutta condition to allow for fluid to wrap around the trailing edge. It is only present for the control vortex and is absent in all subsequently shed vortices.

The circulation created from the actuation is given by

$$\int_{-\frac{c}{2}}^{\frac{c}{2}} \gamma_{\mathrm{C}}(x)\,\mathrm{d}x = (1+\epsilon)\Gamma_{\mathrm{C}}$$

and its moment is

$$\int_{-\frac{c}{2}}^{\frac{c}{2}} x\gamma_{\mathrm{C}}(x)\,\mathrm{d}x = x_{\mathrm{C}}\Gamma_{\mathrm{C}}.$$

We must make the appropriate changes to the conservation of circulation so that it now reads

$$(1+\epsilon)\Gamma_{\mathrm{C}} + \Gamma_0 + \sum_{j=1}^{N}\Gamma_j\sqrt{\frac{x_j+\frac{c}{2}}{x_j-\frac{c}{2}}} = 0. \tag{2.41}$$

The integration scheme in Section 2.2.6 must be modified so that (2.29) now reads

$$G(t) \equiv -(1+\epsilon)\Gamma_{\mathrm{C}} - \Gamma_0 - \sum_{j=2}^{N}\Gamma_j\sqrt{\frac{x_j+\frac{c}{2}}{x_j-\frac{c}{2}}}. \tag{2.42}$$

All other quantities in Section 2.2.6 remain the same and are treated in the same manner.

Due to the addition of the control vortex the lift and moment equations are also slightly modified to include the effect of the actuation so that (2.27) and (2.28) become

$$C_L = \pi\left(-\frac{c}{2U_\infty^2}\ddot{y}_{\mathrm{b}} - \frac{2}{U_\infty}\dot{y}_{\mathrm{b}} + \frac{ac}{2U_\infty^2}\ddot{\alpha} + \frac{2a+c}{U_\infty}\dot{\alpha} + 2\alpha\right) - \frac{1}{U_\infty}\sum_{j=1}^{N}\frac{\Gamma_j}{\sqrt{x_j^2 - \frac{c^2}{4}}} - \frac{2\,(1+\epsilon)\,\Gamma_{\mathrm{C}}}{U_\infty c} \tag{2.43a}$$

$$C_M(a) = -\frac{a}{c}C_L + \pi\left(-\frac{\pi}{2U_\infty}\dot{y}_{\mathrm{b}} - \frac{c^2}{64U_\infty^2}\ddot{\alpha} - \frac{a}{2U_\infty}\dot{\alpha} - \frac{1}{2}\alpha\right) - \frac{1}{4U_\infty}\sum_{j=1}^{N}\frac{\Gamma_j}{\sqrt{x_j^2 - \frac{c^2}{4}}} + \frac{2x_{\mathrm{C}}\Gamma_{\mathrm{C}}}{U_\infty c^2}. \tag{2.43b}$$
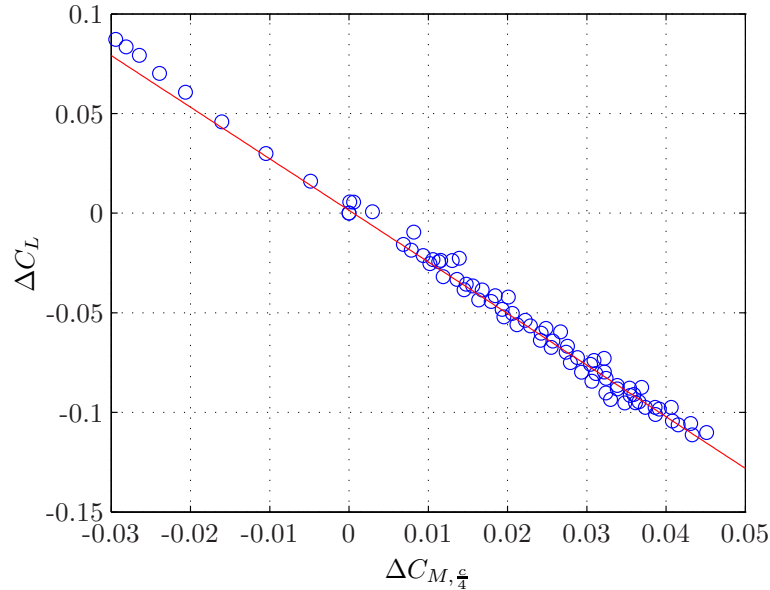
Figure 2.15: Change in lift versus the change in moment due to a control input for various control input strengths $(-1 < u_C < 1)$ and AOA $(-10 < \alpha < 10)$: $\circ$ experiments; —— linear fit, $\Delta C_L / \Delta C_{M,\frac{c}{4}} = -2.5$.

2.5.3 Static fitting for the shift in Kutta condition and trapped vortex strength

Two things must be modeled before proceeding. Static tests are performed to find both the parameter ϵ and the relationship between voltage input, u_C to the trapped circulation strength, Γ_C. First, ϵ is determined by performing experiments (performed by the thesis author and A. Kutay, from GTRI) to measure the change in moment and lift solely to the actuation. In steady state, from Equations (2.43),

$$\frac{\Delta C_L}{\Delta C_{M,\frac{c}{4}}} = \frac{(1 + \epsilon)}{(1 + \epsilon)\frac{a}{c} + \frac{x_C}{c}}$$

represents the ratio of the change due to an input in control vortex strength $\Gamma_C(u_C, \alpha)$ for fixed α. From experimental data given in Figure 2.15, it appears the slope depicted is nearly constant for all conditions when varying the control input from $-1 < u_C < 1$ and AOA $-10 < \alpha < 16$. This is not only true for the current configuration but for several configurations where the actuator locations are changed (Brzozowski, 2009). The slope of the least squares linear fit of the data provided in
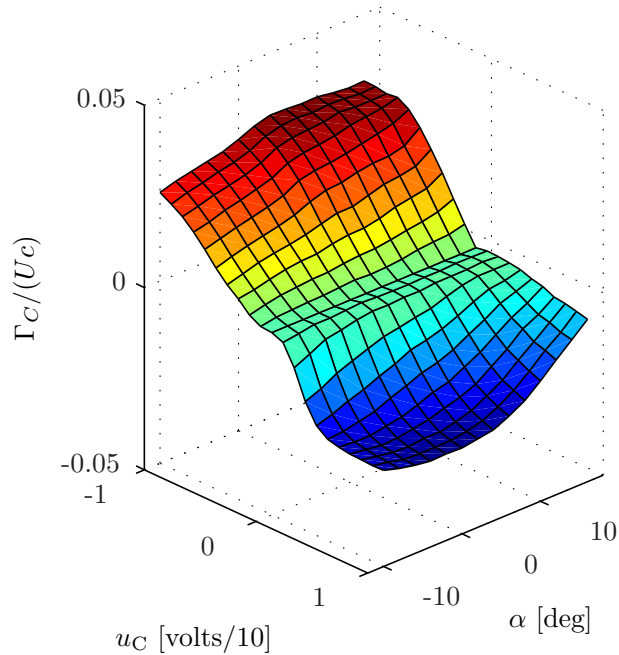
Figure 2.16: Relationship between Γ_C, u_C, and α. A positive voltage turns on the SS actuator (negative turns on the PS actuator). Both actuators cannot be simultaneously on.

firgure 2.15 is $\Delta C_L / \Delta C_{M,\frac{c}{4}} = -2.59$. Solving for ϵ (recall $a/c = 1/4$ and $x_C/c = 0.45$) leads to the value of $\epsilon = 2.31$. This parameter is held constant for all operating conditions as long as the configuration of the airfoil remains the same.

A functional relationship for $\Gamma_C(u_C, \alpha)$ is attained using the same data for generating Figure 2.15. Note, the actuators are not simultaneously turned on because of the specific configuration of the actuators. There are actuators both ont he PS and SS side of the airfoil and turning them both on at the same power level at the same instant produces negligible control authority. Therefore a convention is chosen such that $u_C > 0$ turns on the SS actuator and $u_C < 0$ turns on the PS actuator. From (2.43b) we can determine from steady data the necessary vortex strength to be

$$\frac{\Gamma_C}{U_\infty c} = \frac{\Delta C_{M,\frac{c}{4}}(u, \alpha)}{2\left(\frac{a}{c}(1+\epsilon) + x_C\right)}. \tag{2.44}$$

The functional relationship is plotted in Figure 2.16. The dependence on α is slight compared to the dependence on u_C for moderate AOA, $-10 < \alpha < 10$, nevertheless its dependence is retained to help counteract the unmodeled effects of leading edge separation. We also note that the dependence in
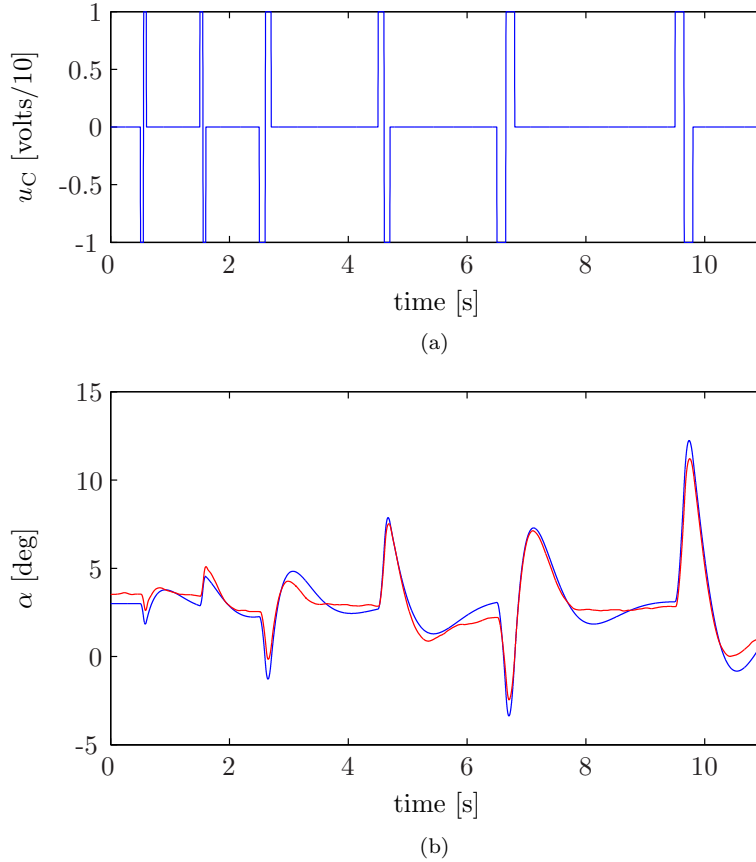
Figure 2.17: Comparison of test bed simulation with experimental results. (a) Input command signal given to both the simulation and the experiment (Tchieu et al., 2008). (b) Airfoil response due to control input: —— current model; —— experiments.

u_C. From this data, a lookup table is used to acquire Γ_C for simulation of the equations of motion.

2.5.4   Comparison between experiments

The model equations with the control vortex effects are compared to the experimental setup. For this case, the airfoil is controlled by the torque motor to hold a specific AOA but with a loosely tuned controller such that a sufficient control input produces an obvious response in the AOA of the airfoil. A simulation of the model is created in MATLAB Simulink to include the airfoil dynamics described by the model presented in Section 2.2 with the additional actuator model described in Section 2.5.2 in addition to the dynamics of the experimental setup depicted in Figure 2.4 undergoing pure pitching airfoil motion. A Simulink schematic and details of the numerical model for the dynamics of the experimental setup can be found in appendix A.

The controller is first set to hold the airfoil at $\alpha = 3°$. Several doublet commands are given to the synthetic jet actuators, each of different duration as seen in Figure 2.17(a), and since the controller is non-aggressive, the airfoil moves substantially. The experimental response (red) and the model response (blue) are given in Figure 2.17(b). The model equations do a very good job of simulating the experimental response. A major difference between the simulation and the experiments is that the airfoil tends to relax to its original position at a much faster rate. This can be attributed to the unmodeled and excessive damping in the experimental apparatus (Muse et al., 2009).

2.5.5   Simple feedback for reduction of vortex induced oscillations

It has been shown in Section 2.4 that under specific conditions an airfoil will undergo non-stalled vortex-induced vibrations in the attached flow regime for a sudden change in AOA which may eventually lead to separation and the onset of stall. In this section, the reduction of such vibrations is investigated using the actuators modeled above. Assuming that α of the airfoil can be exactly measured, a simple control law is proposed such that

$$u_{\mathrm{C}} = -K_{\mathrm{C}}\dot{\alpha}. \tag{2.45}$$

The control can be saturated thus $|u_C| < 1$ at any time. The control strategy is applied to case (f) in table 2.1 in an attempt to stabilize the system. Seen in Figure 2.18 is the response of the system when the gain is set to $K_{\mathrm{C}} = 1$. The control gain is lightly tuned in this case and with feedback, the airfoil is capable of maintaining its stability.

A more sophisticated control strategy is more difficult to design for this case, as the model is still very highly non-linear due many factors, namely the creation of new vortices. Though not the primary interest of this author a further application using adaptive control with a linearized version of the current model applied to the GTRI experiments is found in appendix B.
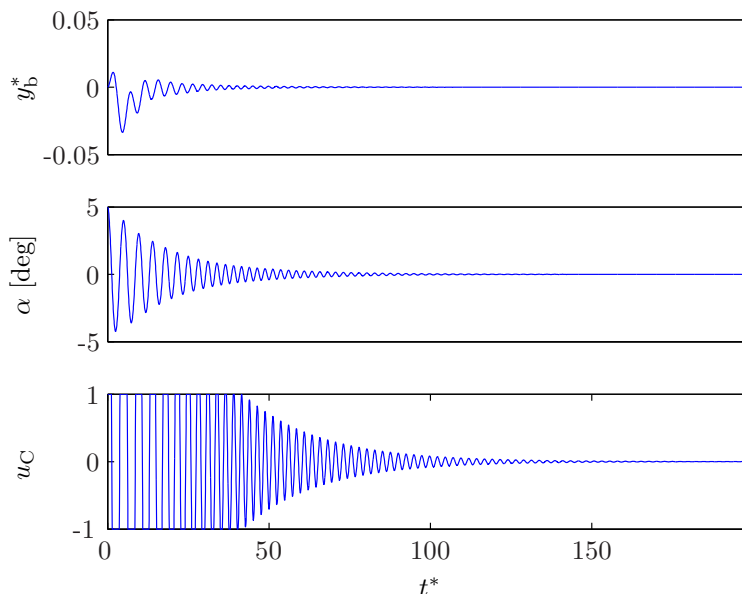
Figure 2.18: Simple feedback is used to reduce the induced vibrations on a airfoil in case (f) in figure 2.1.

2.6   Conclusions

A one-equation aerodynamic model has been created to address the issues related with the fluid-structure interaction of an idealized flat-plate airfoil subject to a free-stream flow. The major assumptions that are in play here are that the airfoil is at very high Reynolds number and that the airfoil does not experience any leading edge separation at any instant thus providing a simplified model for the wake dynamics. The wake dynamics and airfoil circulation distributions are then used to generate expressions for lift and moment. The resulting equations for lift and moment are then adjusted accordingly for application to airfoils with thickness and camber.

The model is compared to experiments performed at GTRI and high-fidelity simulations at University of Texas, Austin of a NACA 4415 wing section at high Reynolds number. The results are quite promising given the number of assumptions used to simplify the model. For low reduced frequencies in pitch and plunge, the model gives a good prediction of the aerodynamic lift and moment. For high reduced frequencies, the agreement is still quite acceptable although the small scale vortex shedding could not be captured from the simplicity of the model.

Given here are just a few of the problems that can be confronted with this model. The flutter

problem is addressed using the model to show, as an example, the use and implementation of the model for fluid-structure interaction. Several examples of stable and unstable flutter phenomena are given. Additionally, a multi-modal response is shown for very stiff structures that may break single bending-torsion mode assumption used for classical flutter analyses.

We note that the model presented here is based on the assumption that no leading edge separation occurs. When large-scale leading edge separation occurs, the model does a marginal job of representing the dominant features in the fluid mechanics and thus does not accurately capture the lift and moment on the airfoil. This may occur when the airfoil performs maneuvers at high angle-of-attack or at very fast pitching and plunge rates. In addition, the model becomes less applicable when the thickness and camber of the airfoil exceed the thin airfoil limit becuase the body may have separation bubbles on the pressure and suction side. This causes a large departure from the thin airfoil theory that is formulated here because these separation bubbles are unsteady in nature.

The aerodynamic model is further extended using the concept of trapped vorticity to model the synthetic jet actuators used in this specific application of airfoil control without conventional control surfaces. The augmented model is then implemented in a simulation of the experimental apparatus at GTRI and its comparison to experimental results give very good agreement. With this validated model, a simple feedback algorithm is used to suppress the vortex-induced vibrations of a thin airfoil. Even when the airfoil undergoes unsteady flutter, the lightly tuned algorithm can stabilize the system. Further application of the model in the context of adaptive control can be found in appendix B.

We note that a more advanced model for the sythetic jets may be formulated for future implementation to help aid with the discrepancies between the model and the experimental results. For a more accurate response, the time dependence of the control vortex must be explicitly treated. In addition, the control vortex may be much more than a function of the control voltage such that it depends on the state of the fluid dynamics and the shape (e.g. camber) of the airfoil. At this point, the only reasonable method, without resorting to modeling each pulse period of the synthetic jet or accounting for specific configurations of the airfoil, is to determine this dependency is through

empirical relations.

Chapter 3

An inviscid low-order model for the vortex-induced vibration of bluff bodies

3.1 Introduction

The ubiquitous nature of vortices in many natural flows have led to various studies of the vortex dynamics in the past with many using low-order models to provide physical understanding of the fluid dynamics in free space and near rigid, stationary boundaries. For high Reynolds number two-dimensional flows, one can expect vortices to behave as compact structures that lose their definition only over large non-dimensional times due to the slight viscosity. Therefore potential point vortices make an excellent simplification to the fluid dynamics problem by reducing the complexity of the governing equations by several orders of magnitude in comparison to direct numerical simulation techniques of the viscous Navier-Stokes equations. Several studies have investigated stationary bluff body flows using point vortices with varied success including studies of vortex shedding behind a square-like section (Clements, 1973), the investigation a flat plate at high angle of attack (Sarpkaya, 1975), and the modeling of separation behind a circular cylinder (Sarpkaya and Schoaff, 1979). In these instances, the evolution vortex sheet-like structure is essentially simulated by introducing individual point vortices at each time step at geometrically convenient and or empirically calculated separation points.

Cortelezzi et al. (1994) and Cortelezzi (1996) further simplified these models by introducing varying strength vortices that followed the so-called Brown-Michael correction (Brown and Michael, 1954, Rott, 1956, Cheng, 1954, Bryson, 1959). Instead of shedding vortices at every time step, a set of ordinary differential equations is derived for the entire system leading to a system with analytical solutions for starting flow and a system that can be numerically integrated using standard methods when more vortices are present. This further reduced the complexity and ad-hoc corrections that were introduced in previous methods.

Until recently the treatment of coupled fluid-structure intereaction (FSI) between point vortices and a single rigid body have not been rigorously treated. Jones et al. (2005) and Shukla and Eldredge (2007) use a vortex sheet representation with the corresponding Birkhoff-Rott integro-differential equation and derived a model to determine the FSI between falling cards and the deformation of a heaving flexible plate, respectively. Moreover, the equations of a body interacting with one or more pre-existing point vortices in an ideal, two-dimensional fluid are derived in Borisov et al. (2007a) as an extension of Ramodanov (2002) and Borisov et al. (2005) following a dynamical systems approach, in addition to the concurrent work performed by Shashikanth (2005). Roenby and Aref (2010) used a similar approach and investigated the integrability of such equations in the context of transition to chaotic motion. Furthermore, Michelin and Smith (2009b) studied the FSI generated by a general sharp-edged body with the Brown-Michael correction in order to study the broadside fall of a thin plate among other studies of FSI (Michelin et al., 2008, Michelin and Smith, 2009a).

In this chapter, we develop a general method to treat the FSI of a bluff body in the presence of a freestream flow and/or multiple vortices. It is chosen to also concentrate on the canonical two degree-of-freedom spring-damper system model of vortex-induced vibration since it is one of the simplest FSI to consider and has various implications in the study of FSI. Previous models of vortex-induced vibration relied heavily on empirical data (Gabbai and Benaroya, 2005, Benaroya and Gabbai, 2008). In many cases, such as wake-oscillator models, the fluid dynamics are nearly non-existent in the description of the model itself. The present model will provide better insight into the interactions of vortices with the canonical mass-spring-damper system for vortex-induced
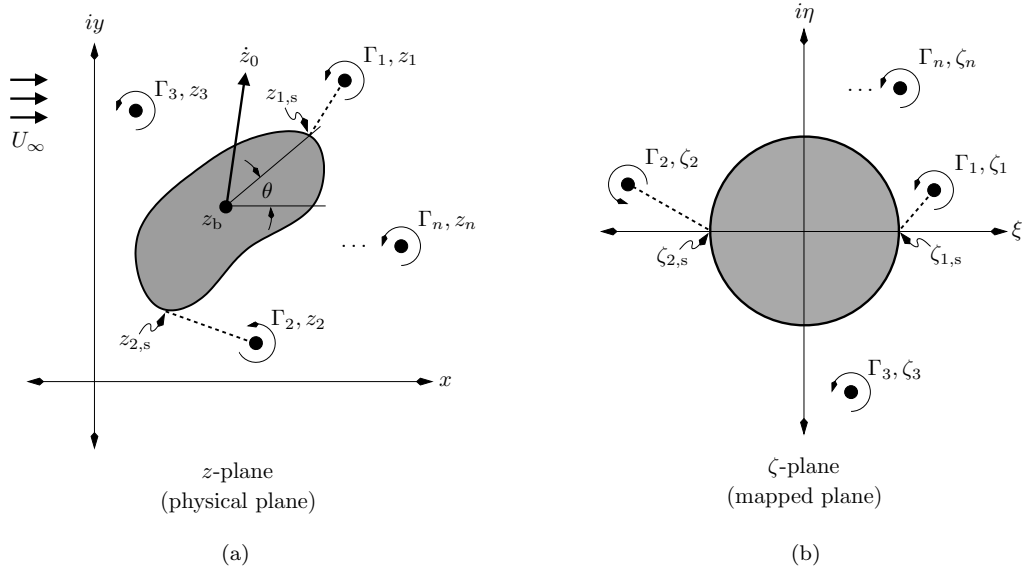
Figure 3.1: Schematic of a body interacting with N point vortices in the physical-plane and the mapped-plane. As an example, two variable strength vortices are illustrated with an attached dotted line to indicate vortex shedding and growth of the vortex. (a) z-plane. (b) ζ-plane.

vibration.

Two specific geometries are more closely investigated. First we consider the case where a circular cylinder interacts with pre-existing vortices in the flow with and without a freestream flow. The introduction of vortices is not addressed in this situation because the inviscid shedding off smooth bodies is an ongoing research topic that is difficult to model. In the case where the freestream is present, we specifically investigate how the vortices excite the modes of oscillation and what kind of responses can be expected.

In the second case, the FSI of a flat plate with vortices is given as an example. The application of a new vortex shedding model is used for this flow. As a test, we first apply the shedding model to a stationary plate and see the resultant vortex motion and shedding cycle to gain confidence in the fluid dynamics. Following this, we apply the model to a vortex-induced vibration case to see a sample response of the system due to the modeled vortex shedding.

3.2 General formulation

Consider the problem as depicted in Figure 3.1(a) in the z-plane where N point vortices of strength Γ_n and location z_n interact with a rigid two-dimesnional solid with centroid location z_0 and orientation defined by θ. Of the N vortices, P vortices are considered to have varying strengths to represent circulation shed from the body (in Figure 3.1(a) these vortices are shown with the attached dotted lines). The body is allowed to translate at velocity $\dot{z}_0$ and rotate at an angular rate $\Omega = \dot{\theta}$ based on the interactions with the vortices and the freestream flow. We seek an incompressible, inviscid potential flow solution for the fluid in an unbounded domain such that the boundary conditions on the body's surface, ∂D_0, are satisfied. To accomplish this, conformal mapping is used to transfer the problem at hand from the physical plane to a more manageable configuration in the mapped-plane (ζ-plane) as depicted in Figure 3.1(b).

3.2.1 Conformal map

The conformal map that takes the circle, $|\zeta| = a$, in the mapped-plane to the the physical boundary in the z-plane with centroid located at z_0 and orientation θ can be written as

$$z = z_0 + \mathrm{e}^{i\theta}g(\zeta). \tag{3.1}$$

For now, we restrict $g(\zeta) \sim \zeta$ as $z \to \infty$. More specific examples of the function will be given in sections 3.3 and 3.4.

3.2.2 Boundary conditions and associated potentials

The solution for the complex potential is a linear combination of the individual contributions due to the flow generated by the translation of the body, W_t, the rotation of the body, W_r, the free stream, W_f, and each vortex, $W_{n,\mathrm{v}}$. For the translational potential, the required boundary condition is such that the normal velocity is exactly balanced by the normal velocity of the body. In complex

notation, this reduces to

$$\text{Re}\left[-i\frac{\mathrm{d}W}{\mathrm{d}s}\right] = \text{Re}\left[-i\dot{\bar{z}}_0\frac{\mathrm{d}z}{\mathrm{d}s}\right] \tag{3.2}$$

where s is taken along the body. After integrating (3.2) with respect to s and noting that $\text{Re}\left[-iW_{\mathrm{t}}\right] = \text{Im}\left[W_{\mathrm{t}}\right]$ it is found that the streamfunction satisfies

$$\text{Im}\left[W_{\mathrm{t}}\right] = \text{Im}\left[\dot{\bar{z}}_0 z\right], \quad \text{on } \partial D_0. \tag{3.3}$$

This is another manifestation of the common *Schwarz problem* and when transfered to the mapped-plane on $|\zeta| = a$, it can be solved by using the Poisson integral formula (or with subtle geometric formulas). The solution to (3.3) given in terms of ζ is

$$W_{\mathrm{t}} = U\left(\zeta - g(\zeta)\right) + \frac{a^2\overline{U}}{\zeta} \tag{3.4}$$

where $U = -\dot{\bar{z}}_0 \mathrm{e}^{i\theta}$.

Similarly for the rotational potential, it is required that

$$\text{Re}\left[-i\frac{\mathrm{d}W_{\mathrm{r}}}{\mathrm{d}s}\right] = \text{Re}\left[i\Omega\left(\bar{z} - \overline{z_0}\right)\frac{\mathrm{d}z}{\mathrm{d}s}\right]$$

and upon integration, the potential satisfies

$$\text{Im}\left[W_{\mathrm{r}}\right] = \text{Im}\left[-i\Omega\left(\frac{1}{2}z\bar{z} - z\bar{z}_k\right)\right], \quad \text{on } \partial D_0. \tag{3.5}$$

The solution for W_{r} in terms of ζ is not obvious and must be found on a case to case basis depending on the mapping function $g(\zeta)$ in (3.1). For now, the solution satisfying (3.5) is denoted

$$W_{\mathrm{r}} = w_{\mathrm{r}}(\zeta). \tag{3.6}$$

Several examples of such potentials can be found in appendix C.

For the freestream and vortex potentials, it is required that the streamfunction satisfies the no flow-through condition

$$\mathrm{Im}\left[W_{\mathrm{f}}\right] = \mathrm{Im}\left[W_{n,\mathrm{v}}\right] = \text{constant, on } \partial D_0. \tag{3.7}$$

The solution for the freestream potential can be found using geometric relationships and is

$$W_{\mathrm{f}} = U_\infty \left(\zeta e^{i\theta} + \frac{a^2 e^{-i\theta}}{\zeta} \right). \tag{3.8}$$

The potential for a single vortex can be found using the circle theorem (Milne-Thomson, 1968) and is simply

$$W_{n,\mathrm{v}} = \frac{\Gamma_n}{2\pi i} \log \left(\frac{\zeta - \zeta_n}{\zeta - \frac{a^2}{\overline{\zeta}_n}} \right). \tag{3.9}$$

Adding Equations (3.4), (3.6), (3.8), and N instances of (3.9) gives the solution to the potential problem

$$W = U\left(\zeta - g(\zeta)\right) + \frac{a^2\overline{U}}{\zeta} + w_{\mathrm{r}}(\zeta) + U_\infty \left(\zeta e^{i\theta} + \frac{a^2 e^{-i\theta}}{\zeta} \right) + \sum_{n=1}^{N} \frac{\Gamma_n}{2\pi i} \log \left(\frac{\zeta - \zeta_n}{\zeta - \frac{a^2}{\overline{\zeta}_n}} \right). \tag{3.10}$$

Note that there are an infinite number of solutions to the boundary value problem. A vortex can always be added at $\zeta = 0$ and still satisfy the zero normal velocity boundary condition. This is commonly referred to as the "bound vortex." It is our interest to study cases where the circulation is zero for all time in the entire domain, therefore this bound vortex is removed.

3.2.3   Definition of the velocity

The velocities in the physical plane are defined as

$$u - iv = \frac{\mathrm{d}W}{\mathrm{d}z} \tag{3.11}$$

$$= \frac{\mathrm{d}W}{\mathrm{d}\zeta} \bigg/ \frac{\mathrm{d}z}{\mathrm{d}\zeta} \tag{3.12}$$

recalling the relation that $W = \tilde{W}(z) = w(\zeta(z))$. The definitions given in (3.4), (3.8), and (3.9) are differentiated and substituted into (3.12) to give

$$\frac{\mathrm{d}W}{\mathrm{d}z} = \frac{\mathrm{e}^{-i\theta}}{g'(\zeta)}\left(U_\infty\left(\frac{\zeta^2\mathrm{e}^{i\theta} - a^2\mathrm{e}^{-i\theta}}{\zeta^2}\right) + U\left(1 - g'(\zeta)\right) - \frac{a^2\overline{U}}{\zeta^2}\right.$$
$$\left. + w'_r(\zeta) + \sum_{n=1}^{N}\frac{\Gamma_n}{2\pi i}\left(\frac{1}{\zeta - \zeta_n} - \frac{\overline{\zeta}_n}{\zeta\overline{\zeta}_n - a^2}\right)\right) \tag{3.13}$$

where the prime denotes differentiation with respect to ζ.

3.2.4   Equation of motion for vortices

We use a more generalized form of the standard Kirchoff laws of vortex motion. Unlike previous studies involving point vortex models this equation accounts change in motion due to the growth of a vortex provided that the location at which circulation is being fed is given (Cortelezzi and Leonard, 1993). This provides a means for circulation to be shed into the wake and it degenerates into the standard Kirchoff law when the vortex remains at constant strength.

Vortices convect with the Brown-Michael law, which mandates that a growing vortex and its associated branch cut must convect force free. With this constraint, the equation of motion for n^{th} vortex in the physical plane, whether being fed or not, is governed by

$$\dot{z}_n + (z_n - z_{n,\mathrm{s}})\frac{\dot{\Gamma}_n}{\Gamma_n} = \overline{\left(\frac{\mathrm{d}W_n}{\mathrm{d}z}\right)} \tag{3.14}$$

where $z_{n,\mathrm{s}}$ is the generating corner for the vortex (see Figure 3.1(a)) and the $(\dot{\ })$ represents the time derivative, $\frac{\mathrm{d}}{\mathrm{d}t}$. The function on the right hand side of (3.14) is defined as the desingularized velocity field such that

$$\frac{\mathrm{d}W_n}{\mathrm{d}z} = \frac{\mathrm{e}^{-i\theta}}{g'(\zeta_n)}\left(\frac{\mathrm{d}W_n}{\mathrm{d}\zeta} - \frac{\Gamma_n}{4\pi i}\left(\frac{g''(\zeta_n)}{g'(\zeta_n)}\right)\right) \tag{3.15}$$

where

$$W_n = W - \frac{\Gamma_n}{2\pi i} \log{(\zeta - \zeta_n)} \tag{3.16}$$

is the desingularized complex potential. The extra term on the right hand side of (3.15) is the so-called Routh correction and it stems from rewriting (3.14) in terms of mapped-coordinates (Clements, 1973). In the case where a vortex has reached a constant strength, i.e., is no longer being fed circulation, then the vortex velocity follows the standard Kirchoff evolution equation

$$\dot{z}_n = \overline{\left(\frac{\mathrm{d}W_n}{\mathrm{d}z}\right)}. \tag{3.17}$$

The equations of motion are most comfortably solved in the ζ-plane, therefore (3.14) is rewritten as

$$\begin{aligned}
\mathrm{e}^{i\theta} g'(\zeta_n)\dot{\zeta}_n + \dot{z}_0 + i\Omega \mathrm{e}^{i\theta} g(\zeta_n) &+ \mathrm{e}^{i\theta}\left(g(\zeta_n) - g(\zeta_{n,\mathrm{s}})\right)\frac{\dot{\Gamma}_n}{\Gamma_n} = \\
\frac{\mathrm{e}^{i\theta}}{\overline{g'(\zeta_n)}} &\left[U_\infty \left(\frac{\overline{\zeta}_n^{-2}\mathrm{e}^{-i\theta} - a^2\mathrm{e}^{i\theta}}{\overline{\zeta}_n^2} \right) + \overline{U}\left(1 - \overline{g'(\zeta_n)}\right) - \frac{a^2 U}{\overline{\zeta}_n^2} + \overline{w'_{\mathrm{r}}(\zeta_n)} \right. \\
&\left. - \sum_{j\neq n}^{N} \frac{\Gamma_j}{2\pi i}\left(\frac{1}{\overline{\zeta}_n - \overline{\zeta}_j} - \frac{\zeta_j}{\overline{\zeta}_n\zeta_j - a^2} \right) + \frac{\Gamma_n}{2\pi i}\left(\frac{\zeta_n}{\zeta_n\overline{\zeta}_n - a^2} + \overline{\frac{g''(\zeta_n)}{2g'(\zeta_n)}} \right) \right].
\end{aligned} \tag{3.18}$$

3.2.5 Force

An expression for the force, $\mathcal{F}$, is given in Sedov (1965) as

$$\frac{\mathcal{F}}{\rho_{\mathrm{f}}} = i\sum_{n=1}^{N} z_{n,\mathrm{s}}\dot{\Gamma}_n + \frac{i}{2}\oint_{\partial D_0}\left(\frac{\mathrm{d}W}{\mathrm{d}z}\right)^2\mathrm{d}z + i\frac{\mathrm{d}}{\mathrm{d}t}\oint_{\partial D_0} z\frac{\mathrm{d}W}{\mathrm{d}z}\mathrm{d}z + A\ddot{z}_0 \tag{3.19}$$

where A denotes the area of the solid body. Equation (3.19) is a variation of the more standard unsteady Blasius integral equation for force that is most commonly used in various references (Milne-Thomson, 1968, Graham, 1980, Cortelezzi, 1996). In essence, all forms of the force integrals are derived by integrating the pressure force on the surface, but there are several key simplifications
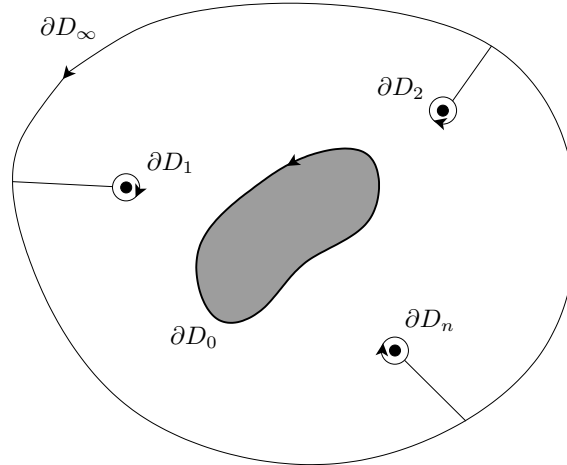
Figure 3.2: Schematic of the application of Cauchy's theorem to deform ∂D_0 to form the contours ∂D_∞, ∂D_n, and the associated contours connecting the two. The infinitessimally thin contours connecting ∂D_n to ∂D_∞ contribute nothing to the integrals in (3.19) because the integrands are analytic in the fluid domain.

made to obtain (3.19) so that the integration is more manageable. In particular, the time derivative given in the third term on the right hand side of (3.19) is taken out of the integrand whereas in the standard unsteady Blasius equation, it remains within.

We can further simplify the expression given in (3.19) by following Michelin and Smith (2009b) and applying Cauchy's theorem. This allows us to extend the contour ∂D_0 to the contour given in Figure 3.2 which consists of a contour at infinity, ∂D_∞, and several infinitesimally small contours around each vortex, ∂D_n, in the opposite sense. Therefore the integrals in (3.19) can be written as $\oint_{\partial D_0} = \oint_{\partial D_\infty} - \sum_{n=1}^{N} \oint_{\partial D_n}$. To make further progress, we expand the potential at $z \to \infty$ to read

$$W = a_1 z + a_0 + \frac{a_{-1}}{z} + \frac{a_{-2}}{z^2} + \mathcal{O}\left(\frac{1}{z^3}\right), \text{ as } z \to \infty \tag{3.20}$$

and subsequently after term by term differentiation

$$\frac{\mathrm{d}W}{\mathrm{d}z} = a_1 - \frac{a_{-1}}{z^2} - \frac{2a_{-2}}{z^3} + \mathcal{O}\left(\frac{1}{z^4}\right), \text{ as } z \to \infty \tag{3.21}$$

where the coefficients a_j are time dependent. In addition, near each vortex, the complex velocity

can be expanded as

$$\frac{\mathrm{d}W}{\mathrm{d}z} = \frac{\Gamma_n}{2\pi i}\left(\frac{1}{z-z_n}\right) + \frac{\mathrm{d}W_n}{\mathrm{d}z} + \mathcal{O}(z-z_n), \text{ as } z \to z_n. \tag{3.22}$$

Upon substitution of (3.20), (3.21), and (3.22) into (3.19), the force reduces to

$$\frac{\mathcal{F}}{\rho_{\mathrm{f}}} = -i\left[\sum_{n=1}^{N}\left(\Gamma_n\dot{z}_n + \dot{\Gamma}_n\left(z_n - z_{n,\mathrm{s}}\right) - \Gamma_n\overline{w}_n\right) + 2\pi i\dot{a}_{-1}\right] + A\ddot{z}_0. \tag{3.23}$$

If the Brown-Michael model (3.14) for growing vortices is used then (3.23) simplifies to

$$\frac{\mathcal{F}}{\rho_{\mathrm{f}}} = 2\pi\dot{a}_{-1} + A\ddot{z}_0. \tag{3.24}$$

The details of the determination of a_{-1} is addressed in specific examples given in sections 3.3 and 3.4 because it depends on the choice of the mapping function, $g(\zeta)$.

3.2.6 Torque

Sedov (1965) also provided an equation for torque, $\mathcal{T}$, which is extended in Michelin and Smith (2009b) to the case where the center of mass of the body moves with location $z_0(t)$. This latter expression is given as

$$\frac{\mathcal{T}}{\rho_{\mathrm{f}}} = \frac{1}{2}\sum_{n=1}^{N}|z_{n,\mathrm{s}} - z_0|^2\dot{\Gamma}_n + \frac{1}{2}\mathrm{Re}\left[2\dot{\bar{z}}_0\oint_{\partial D_0}(z-z_0)\frac{\mathrm{d}W}{\mathrm{d}z}\mathrm{d}z\right.$$
$$\left. - \oint_{\partial D_0}(z-z_0)\left(\frac{\mathrm{d}W}{\mathrm{d}z}\right)^2\mathrm{d}z + \frac{\mathrm{d}}{\mathrm{d}t}\oint_{\partial D_0}|z-z_0|^2\frac{\mathrm{d}W}{\mathrm{d}z}\mathrm{d}z\right]. \tag{3.25}$$

The same technique that is applied in Section 3.2.5 can be used to deform the contour ∂D_0 to simplify (3.25) to read

$$\frac{\mathcal{T}}{\rho_{\mathrm{f}}} = \frac{1}{2}\sum_{n=1}^{N}|z_{n,\mathrm{s}} - z_0|^2\dot{\Gamma}_n + \mathrm{Re}\left[\sum_{n=1}^{N}\left(\frac{\mathrm{d}W_n}{\mathrm{d}z} - \dot{\bar{z}}_0\right)(z_n - z_0)\,\Gamma_n - 2\pi i\dot{\bar{z}}_0 a_{-1} + 2\pi i a_1 a_{-1}\right] + \frac{\dot{\mathcal{B}}}{2}$$

$$\tag{3.26}$$

where

$$\mathcal{B} = \text{Re}\left[\oint_{\partial D_0} |z - z_0|^2 \frac{\mathrm{d}W}{\mathrm{d}z} \mathrm{d}z\right]. \tag{3.27}$$

Although it seems (3.27) is not analytic, given the mapping $g(\zeta)$, it can be integrated by noting that $\overline{z(\zeta)}$ remains analytic on the boundary. Since the function is analytic on the boundary, it can be analytically continued into the domain and integrated using standard complex methods.

3.2.7 Coupled equations of motion

Assuming that there is an external force $\mathcal{F}_e$ and torque $\mathcal{T}_e$, the coupled equations of motion for the bodies are simply

$$(m - \rho_f A)\ddot{z}_0 = 2\pi \rho_f \dot{a}_{-1} + \mathcal{F}_e \tag{3.28}$$

and

$$I\ddot{\theta} = \frac{\rho_f}{2} \sum_{n=1}^{N} |z_{n,s} - z_0|^2 \dot{\Gamma}_n + \rho_f \,\text{Re}\left[\sum_{n=1}^{N} \left(\frac{\mathrm{d}W_n}{\mathrm{d}z} - \dot{\bar{z}}_0\right)(z_n - z_0)\,\Gamma_n \right.$$
$$\left. - 2\pi i \dot{\bar{z}}_0 a_{-1} + 2\pi i a_1 a_{-1}\right] + \frac{\rho_f \dot{\mathcal{B}}}{2} + \mathcal{T}_e \tag{3.29}$$

where m and I are the mass and mass moment of inertia of the body about the centroid, respectively. The Equations (3.18), (3.28), and (3.29) constitute $2N + 3$ equations. If the strength of all vortices are held fixed ($\dot{\Gamma}_n = 0$) then we have $2N + 3$ unknowns ($2N$ vortex positions, two body positions, and one angular orientation) and the problem can be integrated given sufficient initial conditions.

3.3 Vortex-induced vibrations of a circular cylinder

Here we model the induced vibrations of a circular cylinder and a spring-damper system that is depicted in Figure 3.3 with an additional N constant strength vortices. We are not concerned with
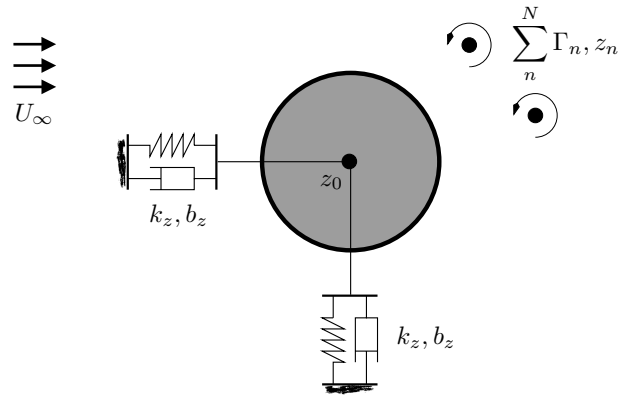
Figure 3.3: Schematic of the vortex-induced vibration for a circular cylinder in cross flow. There are two degrees of freedom for the solid structure, x and y.

vortex growth since it is difficult to model separation off smooth bodies using inviscid methods (Sarpkaya and Schoaff, 1979). The presence of the spring-damper system is modeled by setting the external force to

$$\mathcal{F}_{\mathrm{e}} = -k_z(z_0 - z_{\mathrm{E}}) - b_z \dot{z}_0 \tag{3.30}$$

where k_z and b_z are both scalars and represent the stiffness and damping constant, respectively. The location z_{E} represents the equilibrium position such that the cylinder feels no force from the stiffness.

3.3.1 Equations of motion

In this specific case, due to the geometry of the problem, the orientation θ is not used and thus removed from the equations of motion. In addition, it is not necessary to calculate torques about the centroid (it will be zero by definition). Although we can treat the system without a specific map, one is chosen to stay within the framework presented in Section 3.2, therefore the conformal map for this case is

$$z = z_0 + \zeta \tag{3.31}$$

which just offsets the cylinder at a location z_0. Given the map, the potential can be determined by (3.10) and is

$$W = \frac{a^2 \dot{z}_0}{\zeta} + U_\infty \left(\zeta + \frac{a^2}{\zeta} \right) + \sum_{n=1}^{N} \frac{\Gamma_n}{2\pi i} \log \left(\frac{\zeta - \zeta_n}{\zeta - \frac{a^2}{\bar{\zeta}_n}} \right). \tag{3.32}$$

Performing a series expansion at $z \to \infty$ gives

$$a_{-1} = a^2 (\dot{z}_0 + U_\infty) + \sum_{n=1}^{N} \frac{\Gamma_n}{2\pi i} \left(\frac{a^2}{\bar{\zeta}_n} - \zeta_n \right). \tag{3.33}$$

The equation of motion for the body is found by substituting (3.30) and (3.33) into the equation of motion for the body, (3.28), and explicitly expanding the time derivative to give

$$(\rho_{\mathrm{b}} + \rho_{\mathrm{f}}) \pi a^2 \ddot{z}_0 + b_z \dot{z}_0 + k_z (z_0 - z_{\mathrm{E}}) = i \rho_{\mathrm{f}} \sum_{n=1}^{N} \Gamma_n \left(\dot{\zeta}_n + \left(\frac{a^2}{\bar{\zeta}_n^2} \right) \dot{\bar{\zeta}}_n \right) \tag{3.34}$$

where ρ_{b} is the uniform density of the body. Note that the $\dot{\Gamma}_n = 0$ for all n since the vortex strengths are restricted to be constant and pre-existing.

Upon substitution of (3.32) into Equation (3.18), the motion of the vortices for this specific case is governed by

$$\dot{\zeta}_n = -\dot{z}_0 + \left(\frac{a^2}{\bar{\zeta}_n} \right) \dot{\bar{z}}_0 + U_\infty \left(1 + \frac{a^2}{\bar{\zeta}_n} \right) - \sum_{j \neq n}^{N} \frac{\Gamma_j}{2\pi i} \left(\frac{1}{\bar{\zeta}_n - \bar{\zeta}_j} - \frac{\zeta_j}{\zeta_j \bar{\zeta}_n - a^2} \right) + \frac{\Gamma_n}{2\pi i} \left(\frac{\zeta_n}{\zeta_n \bar{\zeta}_n - a^2} \right) \tag{3.35}$$

The combination of (3.34) and (3.35) together gives $2N + 2$ equations for the $2N + 2$ unknowns ($2N$ vortex positions, ζ_n, and two from the position, z_0) therefore we can solve the system readily using a standard numerical integrator.

3.3.2 Results

Elastically mounted cylinder

Klamo (2007) presented various cases for which a single degree-of-freedom cylinder undergoes large amplitude vortex-induced vibration under the presence of a freestream velocity. Although, in actuality, the induced vibration is created by the unsteady bluff-body shedding, here we choose to examine a specific case of the vortex-induced vibration of in the presence of pre-existing vortices. In the stationary flow case, this may be thought of as ocean eddies interacting with off-shore risers. The spring stiffness and damping are prescribed as $k_z = 1$ and $b_z = 0$ such that the structural natural frequency in vacuum is $\omega_s = \sqrt{1/\pi}$ ($\rho_f = 1$, $a = 1$). In addition we enforce that the fluid is neutrally buoyant such that the density of the cylinder is simply $\rho_b = \rho_f$. These are found to be typical values for which we can expect a large amplitude response in the canonical one-degree of freedom case (Klamo, 2007).

The response of an elastically mounted cylinder is studied in the presence of pre-existing vortices. There is no freestream flow in the cases considered ($U_\infty = 0$) . First, the effect of a single vortex on the structure is explored. Γ_1 is selected so that $\Gamma_1 / (\omega_s D^2) = 1$. The simulation is initialized with a vortex located at $z_1(t = 0) = x_1 > D/2$ and the structure is allowed to interact with it. Plotted in Figure 3.4 is a typical response for this case. As seen in Figure 3.4(a) the motion of the vortex and the cylinder does not follow any particular periodic structure. It is seen in Figure 3.4(b) that the amplitudes oscillations are substantial.

We can attempt to find a maximum amplitude of oscillation, $A^* = \max(|z_0|)/D$, given a starting vortex location, $z_1(t = 0)$. The simulations are run until $t\omega_s = 1000$ at which point the maximum displacement over all time is used to determine the maximum non-dimensional amplitude. This is plotted in Figure 3.5. We can see that there is not a simple relationship. Unexpectedly, when the vortex is very close to the cylinder, its effect is very small. The vortex tends to encircle the cylinder at a very quick rate while avoiding changing its inertia. As the distance is increased, the cylinder begins to oscillate until it reaches a maximum amplitude over time with an initial vortex location

(a)

(b)
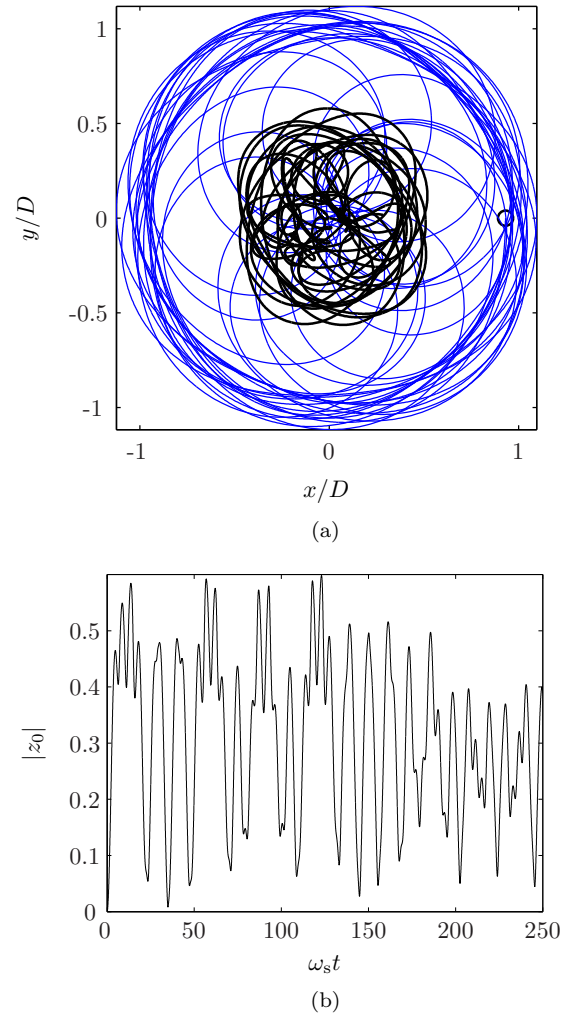
Figure 3.4: Response of the system for $z_1(t = 0)/D = 0.930$ with $k_z = 1$ and $b_z = 0$ at $t = 500$. (a) Cylinder path (black) and vortex path (blue), $\circ$ represents the initial locations of the vortices. (b) Time history of the amplitude of the cylinder response, $|z_0|$.
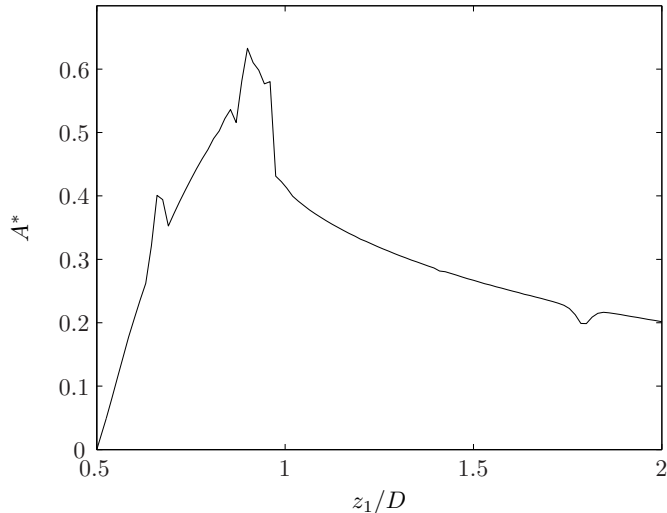
Figure 3.5: Maximum amplitude versus vortex separation distance, z_1/D. $k_z = 1$, $b_z = 0$ $\Gamma_1 = \omega_s D^2 = 2.2568$.

at $z_1(t=0)/D = 0.93$.

As more vortices are added, the system appears to become chaotic. This is partly due to the fact that when there is more than one vortex interacting with a circular cylinder, chaotic motion ensues because of the system is no longer integrable (Roenby and Aref, 2010). We can see this behavior in an example given in Figure 3.6. For a relatively short time, the motion of the cylinder seems erratic. With a slight change in initial conditions, the response becomes drastically different. An effort has been made to find the maximum amplitudes for this case and although the response is always bounded, there was no trend due to the chaotic nature of the flow.

Elastically mounted cylinder with cross-flow

Here vortices are released upstream of the circular cylinder and allowed to convect downstream and interact with the circular cylinder. The system is initialized with a vortex street ahead of the cylinder as depicted in Figure 3.7. The parameters δx and δy define the spacing for the incoming street. The first vortex of the street is located 10 convective time units upstream. We choose $\delta y/D = 0.5$ so that the street impinges on the cylinder initially with the width equal to the cylinder diameter. A Strouhal number is defined such that $\text{St} = f_v D/U$ where f_v is the frequency of the oncoming vortices. In this case, $f_v = U/(\delta x)$ therefore $\text{St} = D/(\delta x)$. We restrict our attention to the case

(a)

(b)
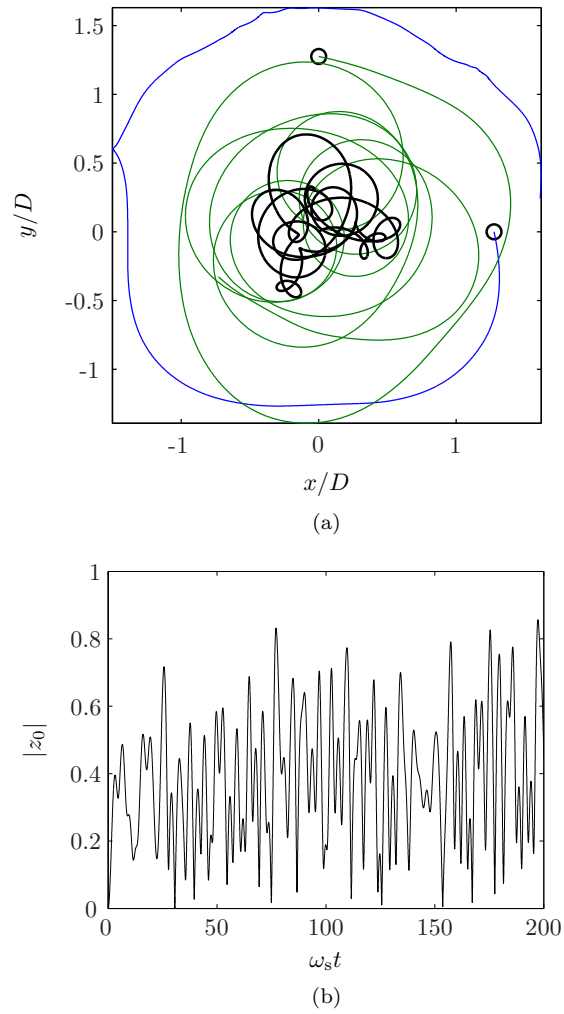
Figure 3.6: Response of the system for $z_1(t=0)/D = 1.275$ and $z_2(t=0)/D = 1.275i$ with $k_z = 1$ and $b_z = 0$ at $t = 100$. (a) Cylinder path (black) and vortex path (blue, green), ○ represents the initial locations of the vortices. (b) Time history of the amplitude of the cylinder response, $|z_0|$.
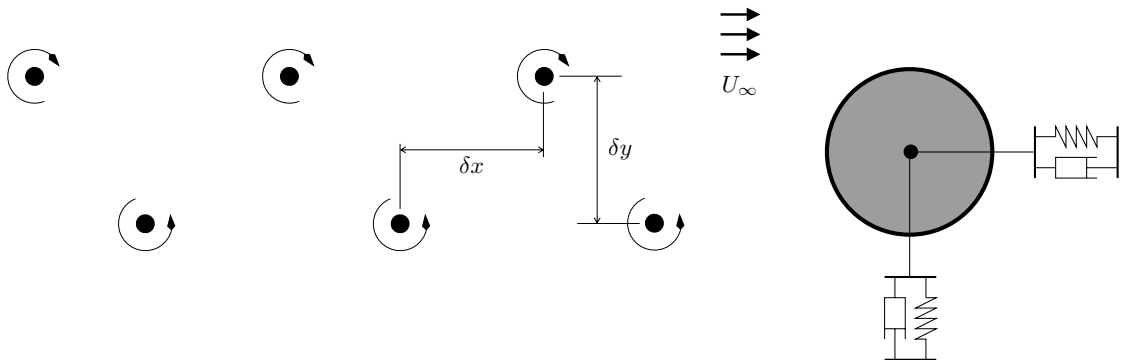
Figure 3.7: Schematic defining the parameters in the vortex street.
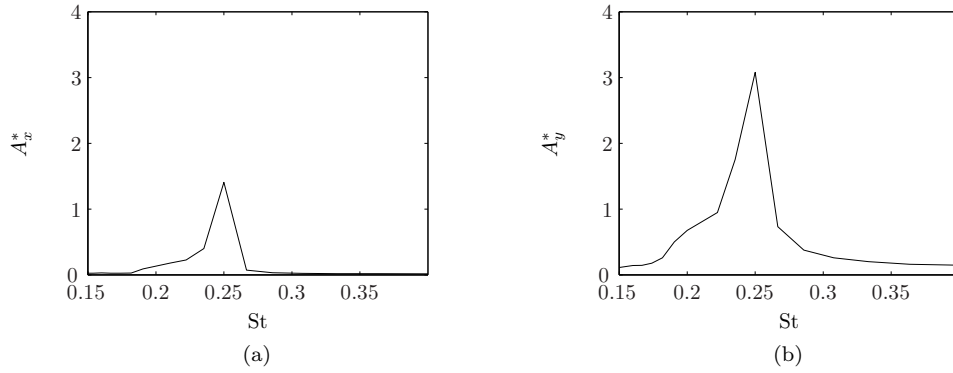
Figure 3.8: Max displacement versus Strouhal frequency of incoming vortex street. (a) x-direction. (b) y-direction.
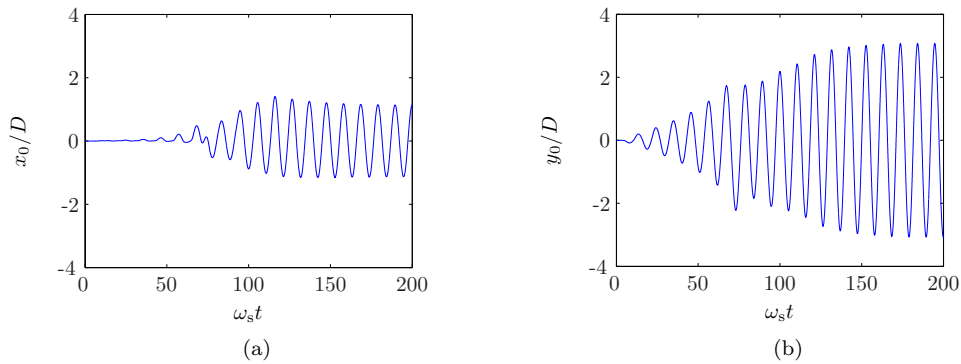
Figure 3.9: Displacement versus time for St $= 0.25$. (a) x-direction. (b) y-direction.

where $k_z = 1$ and $b_z = 0.1$.

Given in Figure 3.8 are the max amplitudes in the x and y-direction for a given Strouhal number for the chosen parameters. As the body starts to vibrate at higher transverse amplitudes, the incoming vortices begin to have a larger influence because they almost hit the structure near head-on (recall $\delta y/D$ is set to one half). This causes a larger force on the cylinder and more feedback until the system saturates as seen in Figure 3.9(b). This type of large amplitude behavior happens near ω_s.
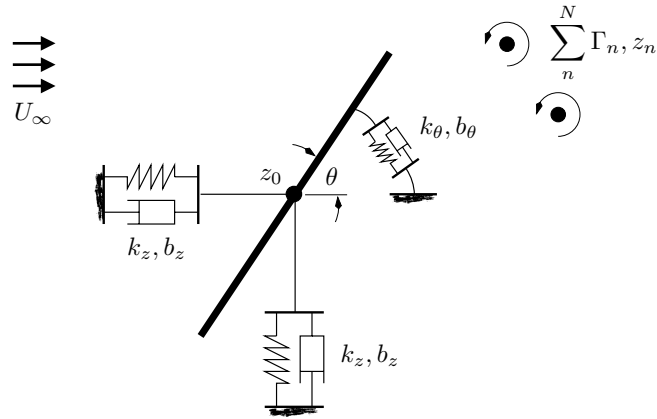
Figure 3.10: Schematic of the vortex-induced vibration for a flat plate in cross flow. There are three degrees of freedom for the solid structure; x, y, and θ.

3.4 Vortex-induced vibration of a flat plate at high angles of attack

We model the induced vibrations of a plate and spring-damper system that are depicted in Figure 3.10. For the body itself, there are three degrees of freedom, x_0, y_0, and θ. In this example, the vortex strengths are not restricted to be constant. In fact, a separation model is also presented to allow circulation to enter the fluid from the two sharp edges of the plate.

Again, the spring-damper system in the x and iy directions is modeled by (3.30). In addition, there is an additional spring-damper system added such that

$$\mathcal{T}_{\mathrm{e}} = -k_\theta(\theta - \theta_{\mathrm{E}}) - b_\theta \Omega \tag{3.36}$$

where k_θ and b_θ represent the stiffness and damping constant in the θ direction, respectively. The equilibrium angle is chosen to be $\theta_{\mathrm{E}} = \frac{\pi}{2}$ so that the freestream flow impinges on the plate in a bluff fashion.

3.4.1 Equations of motion

The mapping taking the circle to a flat plate of length, $l = 4a$ is given by

$$g(\zeta) = \zeta + \frac{a^2}{\zeta}. \tag{3.37}$$

For the mapping (3.37), the potential satisfying the associated boundary conditions in the ζ-plane is given by

$$W = U_\infty \left(\zeta e^{i\theta} + \frac{a^2}{\zeta} e^{-i\theta} \right) - \frac{2ia^2 \mathrm{Im}\,[U]}{\zeta} - \frac{i\Omega a^4}{\zeta^2} - \sum_{n=1}^{N} \frac{i\Gamma_n}{2\pi} \log \left(\frac{\zeta - \zeta_n}{\zeta - \frac{a^2}{\overline{\zeta}_n}} \right) \tag{3.38}$$

where details of deriving the rotational potential, $w_r(\zeta) = -i\Omega a^4/\zeta^2$, are given in appendix C. Upon substitution of (3.38) into (3.18) the equation of motion for the nth vortex is

$$
\left(\frac{\zeta_n^2 - a^2}{\zeta_n^2} \right) \dot{\zeta}_n + \left(\frac{(\zeta_n - \zeta_{n,\mathrm{s}})^2}{\zeta_n \Gamma_n} \right) \dot{\Gamma}_n = \overline{U} - i\Omega \left(1 + \frac{a^2}{\zeta_n} \right)
$$
$$
+ \frac{\overline{\zeta}_n^2}{\overline{\zeta}_n^2 - a^2} \left[U_\infty \left(e^{-i\theta} - \frac{a^2}{\overline{\zeta}_n^2} e^{i\theta} \right) - \frac{2ia^2 \mathrm{Im}\,[U]}{\overline{\zeta}_n^2} - \frac{2i\Omega a^4}{\overline{\zeta}_n^3} \right.
$$
$$
\left. - \sum_{\substack{j \neq n}}^{N} \frac{\Gamma_j}{2\pi i} \left(\frac{1}{\overline{\zeta}_n - \overline{\zeta}_j} - \frac{\zeta_j}{\overline{\zeta}_n \zeta_j - a^2} \right) + \frac{\Gamma_n}{2\pi i} \left(\frac{\zeta_n}{\zeta_n \overline{\zeta}_n - a^2} + \frac{a^2}{\overline{\zeta}_n (\overline{\zeta}_n^2 - a^2)} \right) \right]. \tag{3.39}
$$

To determine the equations of motion for the body, we perform a series expansion on (3.38) to give $a_1 = U_\infty$ and

$$a_{-1} = e^{i\theta} \left(-2ia^2 \left(U_\infty \sin\theta + \mathrm{Im}\,[U] \right) + \sum_{n=1}^{N} \frac{\Gamma_n}{2\pi i} \left(\frac{a^2}{\overline{\zeta}_n} - \zeta_n \right) \right). \tag{3.40}$$

Substituting (3.38) and (3.40) into the coupled linear momentum equation, (3.28) becomes

$$
\frac{m}{\rho_\mathrm{f}} e^{-i\theta} \ddot{z}_0 - 4\pi i a^2 \mathrm{Im}\,\left[\ddot{\overline{z}}_0 e^{i\theta} \right] + \frac{b_z \dot{z}_0 + k_z (z_0 - z_\mathrm{E})}{\rho_\mathrm{f}} e^{-i\theta} = -4\pi i a^2 \left(\Omega U_\infty \cos\theta + \mathrm{Im}\,[i\Omega U] \right)
$$
$$
+ \Omega \left[4\pi a^2 \left(U_\infty \sin\theta + \mathrm{Im}\,[U] \right) - \sum_{n=1}^{N} \Gamma_n \left(\zeta_n - \frac{a^2}{\overline{\zeta}_n} \right) \right] + i \frac{\mathrm{d}}{\mathrm{d}t} \sum_{n=1}^{N} \Gamma_n \left(\zeta_n - \frac{a^2}{\overline{\zeta}_n} \right). \tag{3.41}
$$

Additionally, from (3.29) the angular degree of freedom is dictated by

$$\frac{I\dot{\Omega}}{\rho_{\mathrm{f}}} - \frac{\dot{\mathcal{B}}}{2} - \frac{1}{2}\sum_{n=1}^{2}\left|\left(\zeta_{n,\mathrm{s}} + \frac{a^2}{\zeta_{n,\mathrm{s}}}\right)\right|^2 \dot{\Gamma}_n + \frac{b_\theta \Omega + k_\theta(\theta - \theta_{\mathrm{E}})}{\rho_{\mathrm{f}}} =$$
$$\mathrm{Re}\left[\sum_{n=1}^{N}\Gamma_n\left(\frac{\mathrm{d}W_n}{\mathrm{d}z} - \dot{\bar{z}}_0\right)\left(\zeta_n + \frac{a^2}{\zeta_n}\right)\mathrm{e}^{i\theta} - 2\pi i a_{-1}\left(\dot{\bar{z}}_0 - U_\infty\right)\right] \qquad (3.42)$$

where a_{-1} is defined in (3.40), the derivative of $\mathcal{B}$ is given as

$$\dot{\mathcal{B}} = -4\pi a^4 \dot{\Omega} - 2a^2 \sum_{n=1}^{N}\left(-2\Gamma_n a^2 \mathrm{Re}\left[\frac{\dot{\zeta}_n}{\zeta_n^3}\right] + \dot{\Gamma}_n\left(a^2 \mathrm{Re}\left[\frac{1}{\zeta_n^2}\right] + 1\right)\right), \qquad (3.43)$$

and the vortex velocity is defined as

$$\frac{\mathrm{d}W_n}{\mathrm{d}z} = \frac{\zeta_n^2 \mathrm{e}^{-i\theta}}{\zeta_n^2 - a^2}\left[U_\infty\left(\mathrm{e}^{i\theta} - \frac{a^2}{\zeta_n^2}\mathrm{e}^{-i\theta}\right) + \frac{2ia^2\mathrm{Im}\left[U\right]}{\zeta_n^2} + \frac{2i\Omega a^4}{\zeta_n^3}\right.$$
$$\left. + \sum_{j\neq n}^{N}\frac{\Gamma_j}{2\pi i}\left(\frac{1}{\zeta_n - \zeta_j} - \frac{\bar{\zeta}_j}{\zeta_n\bar{\zeta}_j - a^2}\right) - \frac{\Gamma_n}{2\pi i}\left(\frac{\bar{\zeta}_n}{\zeta_n\bar{\zeta}_n - a^2} + \frac{a^2}{\zeta_n(\zeta_n^2 - a^2)}\right)\right]. \qquad (3.44)$$

If all vortices in the flow are constant strength (i.e. pre-existing) all terms involving $\dot{\Gamma}_n = 0$. This leads to $2N+3$ unknowns ($2N$ vortex locations, ζ_n, two from z_0, and one from the orientation, θ). The combination (3.39), (3.41), and (3.42) give $2N+3$ real valued equations (two per complex equation). Again, a standard scheme is used to integrate the system.

3.4.2 Separation model and the Kutta condition

A shedding model can be conveniently derived for the current problem because of the existence of the two sharp edges on the plate. The complex velocity given by (3.13) is

$$u - iv = \frac{\zeta^2 \mathrm{e}^{-i\theta}}{\zeta^2 - a^2}\left[U_\infty\left(\mathrm{e}^{i\theta} - \frac{a^2}{\zeta^2}\mathrm{e}^{-i\theta}\right) + \frac{2ia^2\mathrm{Im}\left[U\right]}{\zeta^2} + \frac{2i\Omega a^4}{\zeta^3} + \sum_{n=1}^{N}\frac{\Gamma_n}{2\pi i}\left(\frac{1}{\zeta - \zeta_n} - \frac{\bar{\zeta}_n}{\zeta\bar{\zeta}_n - a^2}\right)\right].$$
$$(3.45)$$

Upon closer inspection, (3.45) indicates that at the sharp edges $\zeta = \pm a$ there exists an inherent singularity due to the mapping function. It is reasonable, but not entirely necessary to remove

the singularity at the sharp edges as the system of equations can still be integrated (albeit the velocities near the sharp edges remains unphysical). However, the removal of the singularity can conveniently model the effect of inviscid shedding as well. To do so, one can introduce two vortices, $\Gamma_1(t)$ and $\Gamma_2(t)$, near the tips to remove the singularity. The strength of these vortices is continually adjusted such that the velocity in the frame of the plate is zero at the tip. This is known as applying the unsteady Kutta condition (Cortelezzi and Leonard, 1993). Defining the pseudo-velocity as the interior of the bracketed term in (3.45), $\frac{\mathrm{d}W}{\mathrm{d}\zeta}$, the Kutta condition can be written as

$$\left.\frac{\mathrm{d}W}{\mathrm{d}\zeta}\right|_{\zeta=\pm a} = 0. \tag{3.46}$$

or, when simplified,

$$\mathrm{Im}\left[U_\infty e^{i\theta} + U\right] \pm \Omega a \pm \sum \frac{\Gamma_n}{4\pi a}\left(2\mathrm{Re}\left[\frac{\zeta_n}{\zeta_n \mp a}\right] - 1\right) = 0. \tag{3.47}$$

This condition gives two additional algebraic constraints to the equations of motion by effectively adjusting the strength of the shedding vortices, Γ_1 and Γ_2. This naturally allows a method to introduce circulation into the fluid domain and can be thought of as a model of the separation of a shear layer feeding the two growing vortices.

Vortex shedding criteria

Subsequent vortices can be shed as well. When a vortex grows, one can expect it to become a free vortex at some point and allow an incipient vortex to take its place near the generating tip. The inception of a new vortex can be chosen such that when the rate of change of the strength of the nascent vortex changes sign (e.g. $\dot{\Gamma}_1 = 0$), a new vortex is formed at the sharp tip, as proposed in Section 2.2.4. There is a problem with this specific shedding model for the current geometry that is also inherent in other bluff body flows using an inviscid point vortex model. Consider the plate at a large angle of attack as depicted in Figure 3.10. It is expected that at $\zeta = a$, the corner only feeds negative circulation to the nascent vortex. If the model previously proposed is used in this instance,
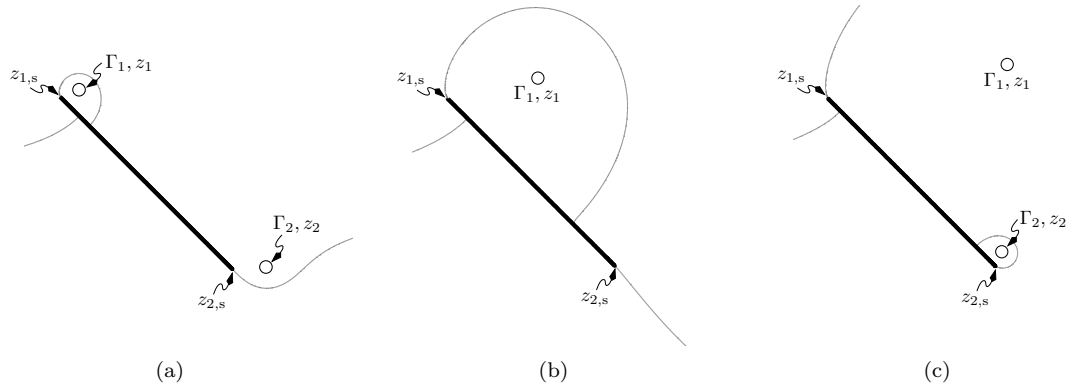
Figure 3.11: Schematic showing the instantaneous stagnation streamline at various instants of time. (a) At the inception of both vortices after impulsive start. (b) At an instant prior to pinch off of Γ_2. (c) The inception of a new vortex where the new vortex is reindexed to Γ_2.

the vortex continues to grow and never pinches off since $\dot{\Gamma}_1$ is always negative. This is contrary to the observation that a von Kàrmàn vortex street is nearly always seen in the wake of a bluff body.

Although the increasing complexity of using vortex sheets as opposed to point vortices can overcome this problem (Jones, 2003), the following scheme is chosen to combat the issue. Shortly after two vortices are initiated, if the plate is not exactly perpendicular to the flow, the leading edge vortex usually recirculates flow such that there is a relative stagnation point on the backside of the plate (i.e., where the velocity relative to the body is zero). This situation is depicted in Figure 3.11(a). At a later time (Figure 3.11(b)) the relative stagnation point moves towards Γ_2. It is proposed that in addition to the previously described shedding criteria, when the stagnation point reaches the opposite sharp tip (in this case $z_{2,\mathrm{s}}$), the vortex being fed from that point (Γ_2) is released and an incipient vortex is introduced at the at the tip. A time shortly after this criteria is illustrated in Figure 3.11(c). Numerically, this is executed by tracking the velocity at a position $z_{p,0}$ on the backside of plate near $z_{p,\mathrm{s}}$ ($p = 1, 2$) and determining whether there is a switch in the the sign of the tangential velocity. The direction of the switch indicates the direction in which the stagnation point passes through $z_{p,0}$. At this point, if the direction is consistent with moving away from the generating edge, then a new vortex is created and the vortices are re-indexed such that the newly created vortex becomes indexed $p = 1$ or 2.

Incipient behavior of vortices

The flow around the sharp corners can lead to the introduction of a vortex near the edge. As indicated in Cortelezzi and Leonard (1993) and more recently in Michelin and Smith (2009b), the introduction of a vortex at the sharp edges creates a singularity since the vortex and its image lie at the same location and the equation of motion for the nascent vortex cannot be readily integrated. Thus, due to the singularity, the initiation of the nascent vortex must be treated separately. A small-time expansion can be used to further unveil the behavior of newly formed vortices from these edges. Here we summarize the main results of the small time expansions presented in Michelin and Smith (2009b) and give a procedure for dealing with the situation where the flow is impulsively started and the case where a vortex is created at the tip with pre-existing vortices in the flow.

In what follows we only consider the vortex that initiates at $\zeta_{1,s} = a$. The vortex that initiates from $\zeta_{2,s} = -a$ can be treated in a similar manner to give essentially the same result. At time $t = 0^+$ the freestream is impulsively started with the plate at high angle of attack. We define $\zeta_1 = a(1 + \tilde{\zeta}_1)$ such that $|\tilde{\zeta}_1| \ll 1$. Closely following Michelin and Smith (2009b), a small time expansion is performed on the equations of motion and it is found that the leading order behavior for the vortex position follows

$$\tilde{\zeta}_1 = C_1 e^{\frac{i\pi}{4}} t^{\frac{1}{3}} \tag{3.48}$$

where C_1 is a constant. Since $z_1 - a = a e^{i\theta} \tilde{\zeta}_1^2$, the dominant flow around the corner forces the vortex to move perpendicularly away from the plate at a power law of $t^{\frac{2}{3}}$ without regard for the orientation of the plate. Consequently, when the Kutta condition is applied, the strength of the vortex grows like $\Gamma_1 \sim -t^{\frac{1}{3}}$.

For subsequent vortices, the situation is more difficult to handle. When a vortex is shed from $\zeta = a$ at $t = t_s$, a new vortex is started in its place and the remaining vortices are re-indexed so the nascent vortex replaces the shed vortex. This new vortex is qualitatively different from the starting flow vortex because the background flow is essentially canceled due to the satisfaction of the Kutta condition. It is seen in Michelin and Smith (2009b) that the small-time expansion in this

instance leads to the vortex shedding with linear growth in the direction tangent to the sharp edge, i.e. $z_1 - a = C_2 e^{i\theta}(t - t_s)$ where C_2 is a constant. This imposes two situations. Depending on the sign of C_2 the vortex can either shed away from the tip into the flow or along the plate. The prior situation is amenable and the latter is very problematic because the inviscid model cannot handle this situation because the vortex and its image will be one and the same. The problematic case often occurs at low angles of attack and can also arise when free vortices move in close proximity to either sharp corner. This is a major drawback of this method. This difficulty is also observed in inviscid vortex sheet models such as Jones (2003) as well. To the author's knowledge, this condition cannot be easily circumvented if encountered. Therefore, we halt the simulation when this condition occurs. The proximity of free vortices to the sharp edges is not an issue in this case because they will be sufficiently swept away downstream by the oncoming flow in the cases we consider.

As for the details of numerical implementation, for the impulsive start, a vortex is initiated perpendicular to each tip at a small distance $\delta \sim \mathcal{O}(\Delta t^{\frac{2}{3}})$ where $\Delta t \sim \mathcal{O}(10^{-5})$. To determine the Γ_p, the Kutta condition is applied. Subsequently, a standard time integrator is used until the criteria to shed a new vortex is met at $t = t_s$. At this time a new vortex is started, but this time it is initiated at $t = t_s + \Delta t$ tangentially at a distance $\delta \sim \mathcal{O}(t - t_s)$. The integration resumes until the criteria for shedding is met again, then a new vortex is shed, and so on.

3.4.3   Results

Stationary plate with cross-flow and shed vortices

The vortex shedding criteria is first verified to provide reasonable results. We incline a plate at $45°$ angle of attack with an impulsively-started oncoming freestream. The radius of the circle in the ζ-plane is chosen to be $a = 1/2$, thus the chord length is $c = 2$. The streamlines for various instants in time are plotted in Figure 3.12. Figure 3.12(a) demonstrates the starting flow around the plate forming two vortices, one of which stays attached to the leading edge for some time and another that moves downstream after initially forming. The stagnation point resulting primarily from the leading edge vortex moves down the plate in Figure 3.12(b) and eventually pinches off the trailing edge

(a) $t = 0.4$

(b) $t = 4.6$

(c) $t = 8.0$

(d) $t = 16.0$
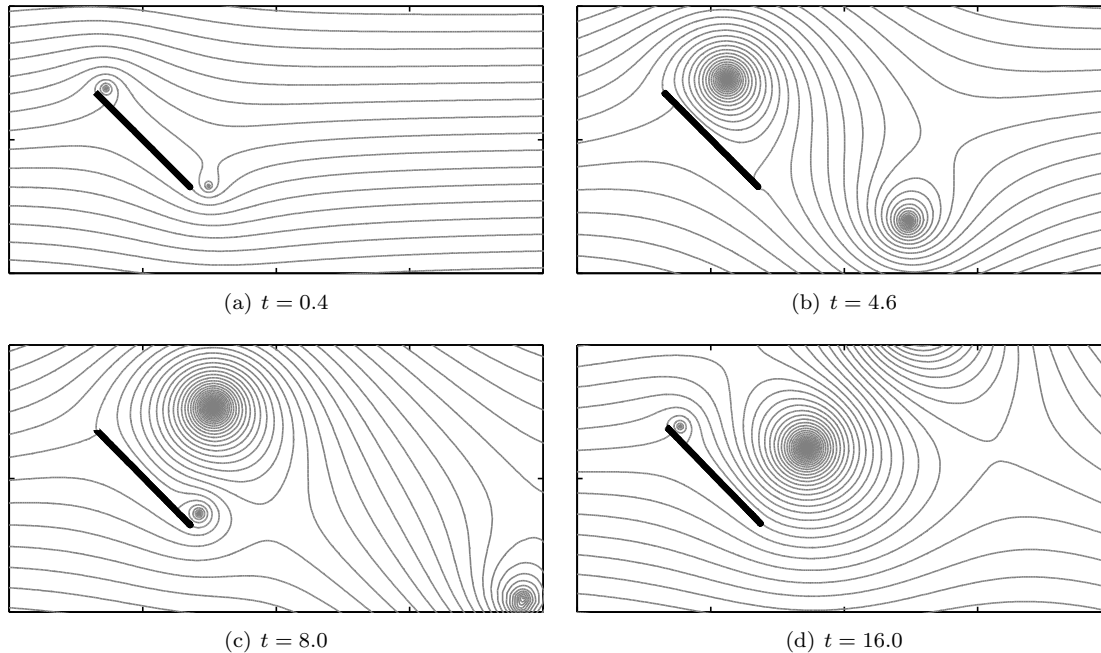
Figure 3.12: Streamlines at various instants in time for separated flow off of a plate at angle of attack of 45°.

vortex causing a new vortex to be formed in Figure 3.12(c). One key difference seen in comparison to the results of some more detailed computations is that in the present method subsequent shed vortices have a much more substantial upwash (Sarpkaya, 1975, Kiya and Arie, 1977). This may be due to an excess amount of circulation that each vortex gathers before meeting the criteria of being shed into the wake. Although a slightly high for a bluff body flow, the long time separation Strouhal number is still reasonable at St ≈ 0.20.

Example of plate vibration due to shed vortices

In this example the plate is only allowed to rotate about its center of mass, that is, z_0 is held fixed. The simulation is initialized with $\theta_0 = \pi/2$. Two vortices are artifically placed far downstream of the plate to break the flow symmetry thus inducing the von Kármán instability in the wake. Other parameters chosen for this simulation are $I = 1$, $k_\theta = 1$, and $b_\theta = 0$. The instability then induces a rotational oscillation in the system shown in Figure 3.13. The simulation is run until the model is no longer valid, i.e. when the velocity at the tip of the plate overcomes the oncoming flow such that a positive (negative) vortex is shed from the top (bottom) separation point. The oscillation of
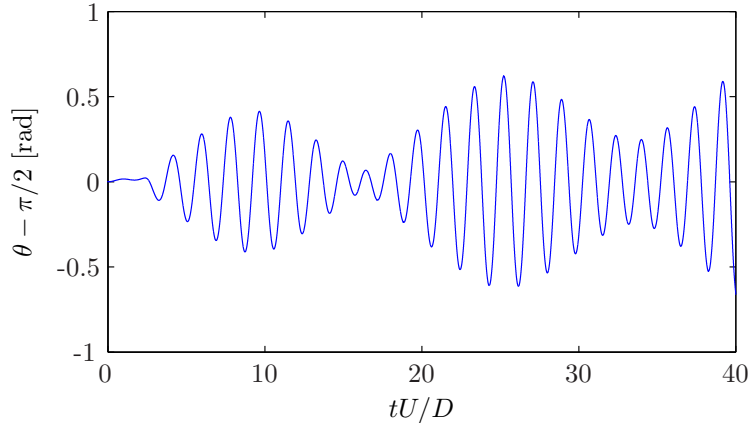
Figure 3.13: Evolution of θ in vortex-induced vibration of a plate.

the plate is modulated by a lower frequency wave. Unlike the circular cylinder case, the system here seems to become unstable due to the feedback between the shed vortices and the oscillation of the plate. When the plate begins to oscillate the shed vortices become stronger, thus inducing stronger oscillations, and so on. The response of the plate begins to deomonstrate some aspects of instability, although system could saturate in the regime where the model is can no longer be simulated.

3.5   Conclusion

A low-order technique has been outlined here to give the response of an elasatically-mounted general shaped body in the presence of point vortices and a freestream velocity. It is formulated using standard potential flow techniques in conjunction to coupling the problem to rigid body dynamics through Sedov's force and moment equations. This allows us to specifically apply an external force to model the structural properties of the fluid-structure interaction. In addition, this model is also amenable to shedding vortices off sharp edges since the general equations of motion allow for variable strength vortices.

Specifically, two examples are presented here. First we considered vortex-induced vibrations of a circular cylinder in the presence of pre-existing vortices. The results show, that even for one vortex, the motion appears to be bounded. We calculate the maximum amplitude for the case of a circular cylinder interacting with one vortex versus the vortex's initial position. It is found that

if a vortex initially lies near a body, it does not affect it much, but as it is moved away from the body, the vortex has more influence until it reaches a local maximum near $z_1/D \approx 1$. For more than one vortex interacting with a circular cylinder, it is difficult to draw any conclusions since the response is chaotic. We then allow a freestream flow to convect the vortices downstream towards a circular cylinder. A vortex street configuration is chosen to impinge on the cylinder. When changing the Strouhal frequency of the impinging vortices, it is seen that the maximum amplitude Strouhal number is around St $= 0.25$ for the configuration considered. At this frequency the vortices couple closely with the natural frequency of the system to produce a large amplitude response. At lower and higher frequencies, the vortices have a minimal effect on exciting the system to oscillate at large transverse magnitudes.

As a further example, the flat plate geometry is also considered. The equations of motion for the system are derived and simulated with a point vortex separation model. This model is simulated for the case of a stationary flat plate and gives reasonable results for the natural shedding frequency of the system. An example of the vortex-induced vibration due to vortex shedding is simulated and discussed.

Only a couple examples of the methodology are given here. More analysis is necessary to draw any definite conclusions about the fluid-structure interaction of these structures. However, the low-order model developed can be used to rapidly simulate problems without relying on higher-order computational techniques. These models run within a matter of seconds and can provide fast, useful information for design, prevention, and control of vortex-induced vibrations. At high Reynolds number, the model of the flat plate geometry is very applicable to vortex-induced vibration for viscous fluid over a flat plate in the sense that it models the separation from the bluff body very well. Vortices shed from the sharp edges retain their compactness for relevant time scales therefore the diffusion due to viscosity is negligible in these cases. An additional model must be developed to combat the difficulties of representing the vortex shedding off smooth bodies before any progress on the prediction of the response of the canonical cylinder-spring-damper system can be made.

Chapter 4

Fluid-structure interactions of two bodies in an inviscid fluid

4.1 Introduction

This chapter addresses the problem of solving for the hydrodynamic interactions between two arbitrarily moving rigid bodies in a two-dimensional inviscid fluid. Not only is it of theoretical interest, but this work also is important for the application to a myriad of doubly connected problems. As an example of such a doubly connected domain problem, the Weis-Fogh mechanism has been previously studied by using complex potential theory for the spreading phase until the two wings separate into an inherently two-body problem (Lighthill, 1973). The analysis within this study does not carry on into the phase where the wings are separated due to a lack of a generalized potential theory for doubly connected domains. Similarly, if we examine the cross-section of a dragonfly wing, we see two wings that constitute another naturally occurring two-body problem where the interactions between each wing cannot be simply neglected (Wang and Russell, 2007). To the author's knowledge, the hydrodynamics of such phenomena have not been previously investigated and the framework provided in this paper will allow its subsequent analysis. Moreover, another relevant example in aerodynamics concerns the flow around two airfoils, or the so-called "biplane problem," where it has been seldom studied from an analytic standpoint. In particular, Sedov's work on this subject is a rare resource and he devotes a short chapter to determining the steady flow around several biplane sections in his book (Sedov, 1965). Many other examples of situations with fundamentally doubly

connected domains exist and the reader is urged to examine Furber and Ffowcswilliams (1979) and Nair and Kanso (2007) for applications to turbomachinery and coordinated motion applied to fish schooling, respectively.

Until recently, the multiply connected domain problem in potential theory has been avoided except for a number of simplified cases. Perhaps as the most simple case, Lagally (1929) was the first to consider the analytical solution of the potential flow problem for two stationary cylinders in a uniform stream. He obtained a rather complicated expression for the velocity potential in terms of Weierstrass functions. This work was later extended to the case of two hydrodynamically coupled cylinders by Landweber and Shahshahan (1991) to study the hydrodynamic forces on two bodies nearing inline impact. Furthermore, Wang (2004) contributed to this specific problem by determining the forces on the cylinders with the extension of allowing the cylinders to contract and expand as well as determining the large distance influence of the cylinders on one another. More recently Borisov et al. (2007b) provided the first dynamically coupled interaction between two circular cylinders in a perfect fluid and restricted his examples to the motion of his cylinders being along the line connecting their centers. We also take notice of the long-lasting interest in the two cylinder problem, as Alassar and El-Gebeily (2009) have recently revisited the fundamental question proposed by Lagally and determined an alternative solution to the potential flow problem using bipolar coordinates and an infinite series expansion. The methods referenced above are very restrictive in the sense that they are only applicable to the case where the bodies are two circular cylinders.

For more complicated shapes, the use of boundary integral formulations, such as panel methods (e.g. Kanso et al., 2005), have supplanted closed-form solutions for the potential due to the lack of a theory. However, Crowdy (2010) has developed a new calculus to address issues with providing solutions to flows in multiply connected domains and has applied it to the Weis-Fogh mechanism discussed above (Crowdy, 2009). Although the doubly connected problem can be solved in Crowdy's framework, here we provide an efficient and specific solution of the flow generated by the motion of two arbitrarily shaped bodies without the need of special functions. This stems from the fact that

the doubly connected case has special properties not available in the general multiply connected case which are exploited in order to avoid using the integral representation in Crowdy (2010). In addition, formulas for the force and moment are provided and a method to study the fluid-structure interaction (FSI) of the system is proposed.

As a specific example, the interaction of two circular cylinders is more closely investigated using the proposed method. First, the method is validated by determining the hydrodynamic forces for the prescribed motions of the two cylinders and comparing the results to previously derived formulations in Wang (2004), Bampalas and Graham (2008), and Landweber and Shahshahan (1991). Next, numerical analyses are performed to address the benefits of hydrodynamic drafting in a "forced-free" interaction by prescribing the motion of one cylinder and allowing the second cylinder to follow freely. Lastly, analysis of "free-free" interaction of two cylinders is carried out. Here the idea of "free-free" interactions refers to objects that are given initial conditions and allowed to interact with the flow field freely, which in part has been studied in Borisov et al. (2007b) for specific inline motions of the cylinders. Here, we choose to concentrate on studying the oblique collision and near-collision events of two hydrodynamically coupled cylinders and demonstrate that the system conserves total energy and momentum.

An additional example of two flapping plates, similar to the configuration discussed in Wang and Russell (2007), is provided to highlight the use of the method in a more complicated doubly connected domain. An idealized flapping motion is examined and resulting forces and torque on both individual plates are determined for the specified motion.

4.2   Potential flow formulation

4.2.1   Formulation of the boundary value problem

We seek an incompressible, inviscid, and irrotational flow in an unbounded two-dimensional fluid domain D that is exterior to two solid objects, D_1 and D_2. Let us denote each body by a subscript $k = 1, 2$ so that each body moves with velocity $\mathbf{U}_k = (u_k, v_k)$ and rotates with the angular rate

Ω_k. Kelvin's theorem guarantees that a flow that originates in an irrotational flow must remain irrotational everywhere thus for all time there exists a velocity potential Φ such that $\mathbf{u} = \nabla\Phi$. Incompressibility requires that the velocity potential must satisfy Laplace's equation, $\nabla^2\Phi = 0$, in the domain D. Since Φ is harmonic, the solution can additionally be recast as finding its harmonic conjugate, the streamfunction Ψ. Additionally, it is assumed that the flow decays at infinity and that the circulation around each object is zero. The solution must satisfy the boundary conditions

$$\mathbf{u} \cdot \hat{\mathbf{n}} = (\mathbf{U}_k + \Omega_k \hat{\mathbf{e}}_z \times (\mathbf{x} - \mathbf{x}_k)) \cdot \hat{\mathbf{n}}, \text{ on } \partial D_k \tag{4.1}$$

for $k = 1, 2$ where $\hat{\mathbf{n}}$ denotes the unit outward facing normal. In what follows, it is understood that the boundary conditions are for each body, $k = 1, 2$. We introduce s to denote the length along a specific contour ∂D_k such that the tangent vector and outward normal can be written as

$$\hat{\mathbf{s}} = \left(\frac{\mathrm{d}x}{\mathrm{d}s}, \frac{\mathrm{d}y}{\mathrm{d}s}\right) \tag{4.2}$$

and

$$\hat{\mathbf{n}} = \left(\frac{\mathrm{d}y}{\mathrm{d}s}, -\frac{\mathrm{d}x}{\mathrm{d}s}\right). \tag{4.3}$$

By the Cauchy-Riemann equations it is recognized that the normal velocity on the surface $\mathbf{u} \cdot \hat{\mathbf{n}} = \nabla\Phi \cdot \hat{\mathbf{n}} = \nabla\Psi \cdot \hat{\mathbf{s}}$. Therefore Equation (4.1), by using definitions (4.2) and (4.3), can be rewritten in terms of the streamfunction as

$$\frac{\partial\Psi}{\partial x}\frac{\mathrm{d}x}{\mathrm{d}s} + \frac{\partial\Psi}{\partial y}\frac{\mathrm{d}y}{\mathrm{d}s} = -\left(v_k + \Omega_k(x - x_k)\right)\frac{\mathrm{d}x}{\mathrm{d}s} + \left(u_k - \Omega_k(y - y_k)\right)\frac{\mathrm{d}y}{\mathrm{d}s} \tag{4.4}$$

on ∂D_k. For an arbitrary surface, (4.4) is satisfied only if

$$\frac{\partial\Psi}{\partial x} = -v_k - \Omega_k(x - x_k), \text{ on } \partial D_k, \tag{4.5a}$$

$$\frac{\partial\Psi}{\partial y} = u_k - \Omega_k(y - y_k), \text{ on } \partial D_k. \tag{4.5b}$$
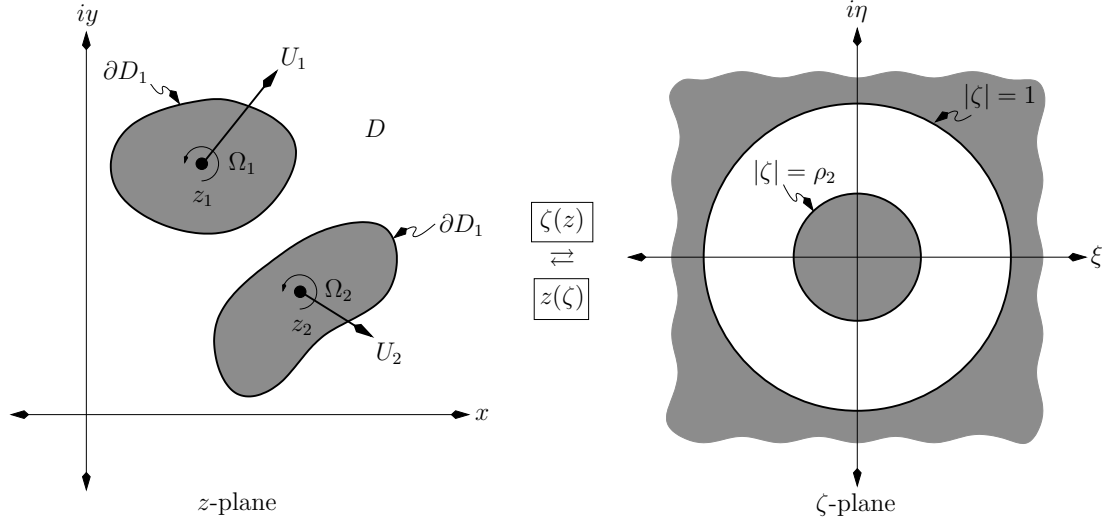
Figure 4.1: Two arbitrarily shaped objects in the z-plane mapped to the annulus in the ζ-plane. Object k translates with complex velocity U_k and rotates with angular velocity Ω_k around its center of inertia z_k. The annulus is centered at $\zeta = 0$ with a conformal modulus of ρ_2.

Upon integration of (4.5), Ψ on the boundary is

$$\Psi = u_k y - v_k x - \Omega_k \left(\frac{x^2 + y^2}{2} - x_k x - y_k y \right) + d_k, \text{ on } \partial D_k \tag{4.6}$$

where d_k are constants of integration.

Now consider the complex variable $z = x + iy$ such that there exists a complex potential function $W(z) = \Phi + i\Psi$ that is analytic in the domain D. In addition, we denote the object velocity in complex form as $U_k = u_k + iv_k$. The problem is now presented in the complex z-plane in Figure 4.1. Equation (4.6) can now be rewritten in complex form to read

$$\text{Im}\left[W(z) \right] = \text{Im}\left[\overline{U}_k z - i\Omega_k \left(\frac{1}{2} z\overline{z} - z\overline{z}_k \right) \right] + d_k, \text{ on } \partial D_k. \tag{4.7}$$

Here "Im" denotes the imaginary part ("Re" the real part) and the overbar denotes explicit complex conjugation. The set of equations for each k in (4.7) is equivalent to the standard mathematical problem in potential theory known as the *modified Schwarz problem* (Muskhelishvili, 1953). Simply stated, if one knows either the real or imaginary value of the complex function on the boundaries, then an analytic solution for $W(z)$ can be found in the domain D. Without loss of generality, the

constant d_1 can be set to zero since it can be arbitrarily specified due to the nature of the modified Schwarz problem. The constant d_2 on the other hand must be determined by a compatibility condition that forces $W(z)$ to be single valued as discussed later in Section 4.2.2.

To make further progress, an extension of the Riemann mapping theorem is employed to doubly connected domains. The theorem states that *any* doubly connected domain can be mapped, by some conformal map $z(\zeta)$, from the annulus given by $\rho_2 < |\zeta| < 1$ in the ζ-plane, where ρ_2 is defined by the choice of domain D and its appropriate mapping (see Figure 4.1 and Goluzin, 1969). Defining

$$w(\zeta) = W(z(\zeta)) \tag{4.8}$$

Equation (4.7) can be recast as a boundary value problem for $w(\zeta)$ on the annulus in the ζ-plane, i.e.

$$\text{Im}\left[w(\zeta)\right] = \text{Im}\left[\overline{U}_k z(\zeta) - i\Omega_k \left(\frac{1}{2} z(\zeta)\overline{z(\zeta)} - z(\zeta)\overline{z}_k\right)\right] + d_k, \text{ on } |\zeta| = \rho_k \tag{4.9}$$

where $\rho_1 = 1$. It is important to observe that due to the geometric relationship $\overline{\zeta} = \rho_k^2/\zeta$ on the boundary, the function between the square brackets in (4.9) can be written as an analytic function of ζ on the boundaries. Additionally, as $z \to \infty$ the potential must decay to a constant, at most. Therefore, this sets a requirement on the mapped potential such that $w(\zeta_\infty)$ must be bounded, where the pre-image of infinity is defined as the $\lim_{\zeta \to \zeta_\infty} z(\zeta) = \infty$.

We note in passing that (4.9) is essentially equivalent to the formulation given by Crowdy (see equation (3) in Crowdy et al., 2007)) since $\text{Im}\left[W(z)\right] = \text{Re}\left[-iW(z)\right]$. In contrast to Crowdy et al. (2007) the rotations Ω_k are introduced as additional degrees of freedom in the current formulation.

4.2.2 Analytic solution to the boundary value problem

Although the solution for $w(\zeta)$ can be obtained by using the *Villat formula* (see Crowdy et al., 2007, Crowdy, 2008, Akhiezer, 1990), we prefer here to use a representation of the complex potential in terms of a Laurent series because it is a natural representation of the solution in the annulus domain. By using the Laurent series expansion, the determination of the Laurent coefficients will

stem directly from application of the boundary conditions. One reason for using this method is that, as shown below, the values of the coefficients can be efficiently calculated by using fast Fourier transforms. Thus, consider the Laurent series expansion of the potential

$$w(\zeta) = \sum_{j=-\infty}^{\infty} a_j \zeta^j. \tag{4.10}$$

The representation given in (4.10) satisfies the condition at infinity as long as the series is convergent. To determine the coefficients a_j, the required boundary data in (4.9) are expanded and rewritten as an analytic function, i.e.

$$\begin{aligned} \mathrm{Im}\,[w(\zeta)] &= \frac{1}{2i} \left(w(\zeta) - \overline{w}(\rho_k^2 \zeta^{-1}) \right), \quad \text{on } |\zeta| = \rho_k \\ &= \frac{1}{2i} \sum_{j=-\infty}^{\infty} \left(a_j - \overline{a}_{-j} \rho_k^{-2j} \right) \zeta^j, \quad \text{on } |\zeta| = \rho_k \end{aligned} \tag{4.11}$$

where the overbar on w denotes the Schwarz conjugate of the function,

$$\overline{w}(\zeta) = \overline{w(\overline{\zeta})}. \tag{4.12}$$

Subsequently, the known boundary data are also expanded as

$$\mathrm{Im}\left[\overline{U}_k z(\zeta) - i\Omega_k \left(\frac{1}{2} z(\zeta)\overline{z}(\rho_k^2/\zeta) - z(\zeta)\overline{z}_k \right) \right] = \sum_{j=-\infty}^{\infty} b_{k,j} \zeta^j, \quad \text{on } |\zeta| = \rho_k \tag{4.13}$$

where (see Saff and Snider (2003), pg. 269)

$$b_{k,j} = \frac{1}{2\pi i} \oint_{|\zeta|=\rho_k} \frac{\mathrm{Im}\left[\overline{U}_k z(\zeta) - i\Omega_k \left(\frac{1}{2} z(\zeta)\overline{z}(\rho_k^2/\zeta) - z(\zeta)\overline{z}_k \right) \right]}{\zeta^{j+1}} \, d\zeta. \tag{4.14}$$

The coefficients (4.14) can be solved explicitly because the integrand can be written as an analytic function on the boundary. To do so, one can use residue theory for every j^{th} term. Practically, due to the duality of the Laurent series and the Fourier transform, the coefficients (4.14) can be calculated numerically in an efficient manner by using the fast Fourier transform. The Laurent coefficients can

be found from the Fourier series representation of the boundary data by relating $b'_{k,j} = b_{k,j} \rho_k^j$ where

$b'_{k,j}$ are the Fourier coefficients. It is also useful to recognize that due to the fact that real data is

provided on the boundary for the determination of these coefficients, the negative coefficients are

given by the alternative relationship $b_{k,-j} = \rho_k^{2j} \bar{b}_{k,j}$ for $j \geq 0$.

Equating coefficients in (4.11) and (4.13) leads to

$$a_j = \frac{2i}{1 - \rho_2^{2j}} \begin{cases} b_{1,j} - b_{2,j} \rho_2^{2j}, & j > 0 \\ \\ b_{2,j} - b_{1,j} \rho_2^{2j}, & j < 0 \end{cases} . \tag{4.15}$$

The zero term must be explicitly treated as a compatibility constraint. Equating the constant terms

uniquely defines $d_2 = b_{1,0} - b_{2,0}$ in addition to requiring $\text{Im}[a_0] = b_{1,0}$. It is observed that the

solution for $w(\zeta)$ can only be solved for up to an additive constant whose value is inconsequential

in obtaining the solution for the flow. Furthermore, it can be confirmed by simple algebra that the

coefficients a_j decay exponentially as $j \to \pm\infty$, since the coefficients $b'_{k,j}$ of the periodic boundary

data decay exponentially as well. Thus given the motions U_k and Ω_k and the appropriate conformal

mapping function $z(\zeta)$ one can explicitly form all the components to construct a solution of the form

(4.10).

Some care must be taken when numerically truncating the series (4.10). When bodies are rather

close in proximity, more terms of the series must be retained to provide an adequate representation

of the potential since the conformal radius ρ_2 approaches 1. In the examples provided here, the

series is truncated to N terms such that

$$\frac{|a_N|^2}{\sum_{j=1}^{N-1} |a_j|^2.} < 0.01$$

thus retaining 99 percent of the energy associated in the expansion. This typically leads to expan-

sions with $N < 50$ terms for separation distances $\epsilon/L \approx \mathcal{O}(10^{-2})$, where L is a pertinent length

scale. Alternatively, a more elaborate truncation correction method can be used to combat the

errors associated with representing the infinite series with a finite number of terms. Landweber

and Shahshahan (1991) discuss a method where the "trapezoidal" remainder left from truncation is used to correct the truncated series. Without the correction it is necessary to retain an additional $N/N_{\text{corrected}} = 2.5$ terms to attain the same level of accuracy for gap distances of $\epsilon/L = 0.01$ for the case of the impact of two circular cylinders, thus it is chosen to ignore the correction for simplicity, although at a higher computational expense.

4.3 Hydrodynamic coupling

In this section, a method for determining the forces and moments and hence the coupled interactions of the two bodies is determined by employing the conservation of momentum and angular momentum.

4.3.1 Hydrodynamic forces and moment

The force on the body can be obtained via complex contour integrals around the objects by extension of the well known unsteady Blasius formula (Milne-Thomson, 1968). Sedov (1965) gives an expression for the complex force, $F_k = f_{k,x} + i f_{k,y}$, and, in the absence of point singularities, it reduces to (with fluid density ρ_{f})

$$\mathcal{F}_k = \overline{\frac{i\rho_{\text{f}}}{2} \oint_{\partial D_k} \left(\frac{\mathrm{d}W}{\mathrm{d}z}\right)^2 \mathrm{d}z} + \ i\rho_{\text{f}} \frac{\mathrm{d}}{\mathrm{d}t} \left[\oint_{\partial D_k} z\frac{\mathrm{d}W}{\mathrm{d}z}\,\mathrm{d}z\right] + \rho_{\text{f}} A_k \ddot{z}_k \qquad (4.16)$$

where A_k and z_k are the area and centroid position of the kth object respectively. It is seen that a "negative-mass" like term is introduced by the last term on the right hand side of Equation (4.16). This may be deceptive since it is counter-intuitive to the notion of added-mass, but the time derivative of the second term of Equation (4.16) produces an additional "mass" term. In later examples this term is found to counteract the "negative-mass" term and produce an overall positive added-mass for the system bodies.

Similarly, from Michelin and Smith (2009b), the torque applied by the fluid onto the body about

its moving centroid in the laboratory frame is found to be

$$
\begin{aligned}
\mathcal{T}_k = \quad & \frac{\rho_{\mathrm{f}}}{2} \mathrm{Re} \left[2\dot{\bar{z}}_k \oint_{\partial D_k} (z - z_k) \frac{\mathrm{d}W}{\mathrm{d}z} \, \mathrm{d}z \right. \\
& - \oint_{\partial D_k} (z - z_k) \left(\frac{\mathrm{d}W}{\mathrm{d}z} \right)^2 \mathrm{d}z \\
& \left. + \frac{\mathrm{d}}{\mathrm{d}t} \oint_{\partial D_k} |z - z_k|^2 \frac{\mathrm{d}W}{\mathrm{d}z} \, \mathrm{d}z \right].
\end{aligned}
\tag{4.17}
$$

There are no further simplifications that can be made without prior knowledge of the form of the mapping function $z(\zeta)$. One can transform (4.16) and (4.17) from integrals in the z-plane to integrals in the ζ-plane. Thus, (4.16) and (4.17) can be replaced respectively by

$$
\mathcal{F}_k = \overline{\frac{i\rho_{\mathrm{f}}}{2} \oint_{|\zeta|=\rho_k} \left(\frac{\mathrm{d}w}{\mathrm{d}\zeta} \right)^2 \left(\frac{\mathrm{d}z}{\mathrm{d}\zeta} \right)^{-1} \mathrm{d}\zeta} + i\rho_{\mathrm{f}} \frac{\mathrm{d}}{\mathrm{d}t} \left[\oint_{|\zeta|=\rho_k} z(\zeta) \frac{\mathrm{d}w}{\mathrm{d}\zeta} \, \mathrm{d}\zeta \right] + \rho_{\mathrm{f}} A_k \ddot{z}_k
\tag{4.18}
$$

and

$$
\begin{aligned}
\mathcal{T}_k = \quad & \frac{\rho_{\mathrm{f}}}{2} \mathrm{Re} \left[2\dot{\bar{z}}_k \oint_{|\zeta|=\rho_k} (z(\zeta) - z_k) \frac{\mathrm{d}w}{\mathrm{d}\zeta} \, \mathrm{d}\zeta \right. \\
& - \oint_{|\zeta|=\rho_k} (z(\zeta) - z_k) \left(\frac{\mathrm{d}w}{\mathrm{d}\zeta} \right)^2 \left(\frac{\mathrm{d}z}{\mathrm{d}\zeta} \right)^{-1} \mathrm{d}\zeta \\
& \left. + \frac{\mathrm{d}}{\mathrm{d}t} \oint_{|\zeta|=\rho_k} |z(\zeta) - z_k|^2 \frac{\mathrm{d}w}{\mathrm{d}\zeta} \, \mathrm{d}\zeta \right]
\end{aligned}
\tag{4.19}
$$

where all integrals are now evaluated in the ζ-plane. The integrals can be evaluated using residue theory as in Bampalas and Graham (2008) but due to the series form of $w(\zeta)$ and the geometry of the doubly connected domain, formulas (4.18) and (4.19) are best integrated numerically by parameterizing the curves $|\zeta| = \rho_k$ as $\zeta = \rho_k \exp(i\sigma)$ and integrating from 0 to 2π. This gives a numerical integration of a periodic function on a periodic domain and thus the integration can be carried out with spectral accuracy by employing a trapezoidal-rule quadrature.

It is also worthy to note that the Equations (4.18) and (4.19) are extremely useful in the presence of discrete vortices as they removes the contour integration around the logarithmic singularities that are present in the standard formulation of the unsteady Blasius formula (Michelin and Smith, 2009b).

Crowdy (2010) has developed a novel method to add vortices to multiply connected domains and it can be readily applied to the current problem.

4.3.2 Coupled fluid-structure interactions

The equations dictating the coupled fluid-structure motion are

$$(\rho_{\mathrm{b},k} - \rho_{\mathrm{f}})A_k\ddot{z}_k = \overline{\frac{i\rho_{\mathrm{f}}}{2} \oint_{|\zeta|=\rho_k} \left(\frac{\mathrm{d}w}{\mathrm{d}\zeta}\right)^2 \left(\frac{\mathrm{d}z}{\mathrm{d}\zeta}\right)^{-1} \mathrm{d}\zeta} + i\rho_{\mathrm{f}}\frac{\mathrm{d}}{\mathrm{d}t}\left[\oint_{|\zeta|=\rho_k} z(\zeta)\frac{\mathrm{d}w}{\mathrm{d}\zeta}\,\mathrm{d}\zeta\right] \tag{4.20}$$

and

$$\begin{aligned}
I_k\ddot{\theta} = \frac{\rho_{\mathrm{f}}}{2}\mathrm{Re}\Bigg[&2\dot{\bar{z}}_k \oint_{|\zeta|=\rho_k} (z(\zeta) - z_k)\frac{\mathrm{d}w}{\mathrm{d}\zeta}\,\mathrm{d}\zeta \\
&- \oint_{|\zeta|=\rho_k} (z(\zeta) - z_k)\left(\frac{\mathrm{d}w}{\mathrm{d}\zeta}\right)^2\left(\frac{\mathrm{d}z}{\mathrm{d}\zeta}\right)^{-1}\mathrm{d}\zeta \\
&+ \frac{\mathrm{d}}{\mathrm{d}t}\oint_{|\zeta|=\rho_k} |z(\zeta) - z_k|^2\frac{\mathrm{d}w}{\mathrm{d}\zeta}\,\mathrm{d}\zeta\Bigg]
\end{aligned} \tag{4.21}$$

with $\rho_{\mathrm{b},k}$ being the density, I_k the moment of inertia of the kth object, and θ_k being the orientation of body k such that $\dot{\theta}_k = \omega$. One must also take care if numerically integrating the system. Since a time derivative given on the right hand side of Equations (4.20) and (4.21) gives rise to an added-mass type term, at each time step an iterative scheme must be implemented to ensure that the accelerations are consistent. Details of the are given in Appendix D.

4.4 Two interacting circular cylinders

Here, an example of two interacting circular cylinders is more closely investigated using the prescribed method. Due to the symmetry of the problem there is no need to introduce rotations and torques on the bodies.

4.4.1 Conformal map

Two discs lie at $z_1(t)$ and $z_2(t)$ with radii $r_1 = 1$ and r_2 in the z-plane. The Möbius transformation that takes the annulus in the ζ-plane ($\rho_2 < |\zeta| < 1$) to the appropriate configuration in the z-plane is

$$z = z_1 + \exp(i\alpha)\frac{\zeta - \lambda}{\lambda\zeta - 1} \tag{4.22}$$

with

$$\lambda = \frac{1 + \left(\hat{x}_2^2 - r_2^2\right) + \sqrt{(l_1^2 - 1)(l_2^2 - 1)}}{2\hat{x}_2},$$

$\alpha = \arg(z_2 - z_1)$, $\hat{x}_2 = |z_2 - z_1|$, $l_1 = \hat{x}_2 - r_2$, and $l_2 = \hat{x}_2 + r_2$ (see Saff and Snider (2003)). The inner radius of the annulus, i.e. the conformal modulus, is found to be

$$\rho_2 = \frac{\left(\hat{x}_2^2 - r_2^2\right) - 1 - \sqrt{(l_1^2 - 1)(l_2^2 - 1)}}{2r_2}.$$

The conformal map (4.22) can be easily inverted to give the inverse relationship that takes the physical plane to the mapped plane. We also note that in the special case where $r_1 = r_2$ it can be shown that $\lambda^2 \rho_2 = 1$.

4.4.2 Complex potential solution

Analytical expressions for the coefficients (4.14) can be obtained by expanding the boundary data via analytic continuation and integrating around the contour $|\zeta| = \rho_k$. Defining $B_k = \overline{U}_k(\lambda^2 - 1)\exp(i\alpha)$ and $C_k = \overline{U}_k(z_1 + \lambda^{-1}\exp(i\alpha)) - U_k(\overline{z}_1 + \lambda\exp(-i\alpha))$ the boundary data can be expressed as

$$\text{Im}\left[\overline{U}_1 z(\zeta)\right] = \frac{i\overline{B}_1}{2(\zeta - \lambda)} + \frac{iB_1}{2\lambda(\lambda\zeta - 1)} + \frac{iC_1}{2}, \quad \text{on } |\zeta| = 1 \tag{4.23a}$$

$$\text{Im}\left[\overline{U}_2 z(\zeta)\right] = \frac{iB_2}{2\lambda(\lambda\zeta - 1)} + \frac{i\rho_2^2 \overline{B}_2}{2(\zeta - \lambda\rho_2^2)} - \frac{iC_2}{2}, \quad \text{on } |\zeta| = \rho_2. \tag{4.23b}$$

Residue theory is used to integrate (4.14). Inserting Equation (4.23a) and (4.23b) into (4.14) gives residues at $\zeta = 0, 1/\lambda$ and $\zeta = 0, \lambda\rho_2^2$ which lie in their respective contours. Applying the residue theorem gives

$$b_{1,j} = -\frac{i\overline{B}_1}{2\lambda^{j+1}}, \tag{4.24a}$$

$$b_{2,j} = -\frac{iB_2}{2\lambda^{1-j}}, \tag{4.24b}$$

for $j \neq 0$ with the zero terms $b_{1,0} = -\text{Im}[U_1(\overline{z}_1 + \lambda^{-1}\exp(-i\alpha))]$ and $b_{2,0} = -\text{Im}[U_2(\overline{z}_1 + \lambda\exp(-i\alpha))]$. Thus the coefficients in the Laurent expansion (4.15) are

$$a_j = \frac{1}{\lambda^{j+1}(1-\rho_2^{2j})}\begin{cases} \overline{B}_1 - B_2(\rho_2\lambda)^{2j}, & j > 0 \\ \\ \overline{B}_2 - B_1\lambda^{2j}, & j < 0 \end{cases}. \tag{4.25}$$

The necessary compatibility condition sets the constant

$$d_2 = \text{Im}[(U_2 - U_1)\overline{z}_1 + (U_2\lambda - U_1\lambda^{-1})\exp(-i\alpha)].$$

4.4.3 Forces induced from inline impact of two circular cylinders

To validate the method the inline impact of two cylinders is investigated and the results are compared to Wang (2004), Bampalas and Graham (2008), and Landweber and Shahshahan (1991). For simplicity the cylinder radii are taken to be $r_1 = r_2 = 1$ ($D = 2$). The integrals for the force given by (4.16) are integrated numerically using a trapezoidal-rule quadrature. Since motions are prescribed, a simple first order finite difference scheme is used to approximate the time derivative to $\mathcal{O}(10^{-8})$.

First we investigate the inline motion of a cylinder ($k = 2$) towards a stationary cylinder ($k = 1$). Cylinder 2 moves at a constant velocity U_2. Streamlines for such a motion are shown in Figure 4.2. In Figure 4.3, the force coefficient in the x-direction $C_x = 2f_x/(\rho_f U_2^2 D)$ for both the moving and stationary cylinder are plotted versus non-dimensional time $t^* = U_2(t - t_0)/D$. The two cylinders impact at $t^* = 0$. In addition to results from the current formulation, data from the papers of
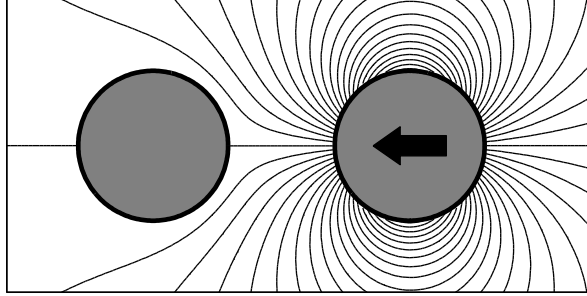
Figure 4.2: Instantaneous streamlines due to a cylinder approaching a fixed cylinder from the right at constant velocity.

Bampalas and Graham (2008), Landweber and Shahshahan (1991), and Wang (2004) are also plotted for comparison. It is useful to note that, unlike the current method, Bampalas and Graham (2008) and Wang (2004) use a form of the Blasius equation much like the formulas given in Milne-Thomson (1968) but with assumptions that allowed the order of the spatial integration and time derivative of Φ to be interchanged. On the other hand Landweber and Shahshahan (1991) used a Lagrangian mechanics perspective to derive the force on the cylinders as outlined in Lamb (1945). Using the current method the agreement to Bampalas and Graham (2008) and Landweber and Shahshahan (1991) is excellent for both the moving and stationary cylinder. As the cylinders approach each other, the forces become unbounded as expected. The results from Wang (2004) for the stationary cylinder agree well, but the results for the moving cylinder are offset due to the incorrect treatment of the Blasius force equation. This difference is accounted for by the omission of a convective term $U_2 \, \partial\Phi/\partial x$ in the standard Blasius equation as discussed in Bampalas and Graham (2008). The Sedov formula presented in (4.16) accounts for such a term in its derivation.

Additionally a case where two cylinders move towards each other at a constant velocity $U_1 = U_2 = U$ is compared. Streamlines for such a case are given in Figure 4.4. The magnitude of the force coefficient in the x-direction is plotted with the same non-dimensional variables as given above. Figure 4.5 shows the results for this configuration in comparison to data from Bampalas and Graham (2008) and Wang (2004). Again, the agreement between Bampalas and Graham (2008) is nearly exact while the results from Wang (2004) are slightly offset due to the mistaken omission of the convective term.
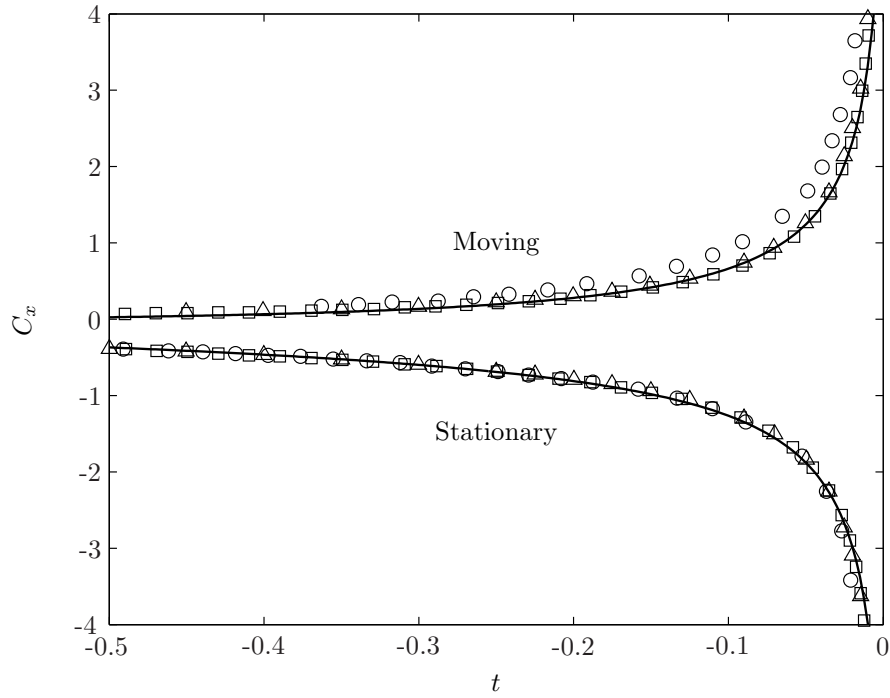
Figure 4.3: Force coefficient C_x when a cylinder moves toward a stationary cylinder as depicted in Figure 4.2. The two cylinders impact at $t^* = 0$. The forces on the moving and stationary body are denoted on the figure. ——— , present method; □ , Bampalas and Graham (2008); ○ , Wang (2004); △ , Landweber and Shahshahan (1991)

.

Figure 4.4: Instantaneous streamlines due to two cylinders approaching each other inline at constant velocity.
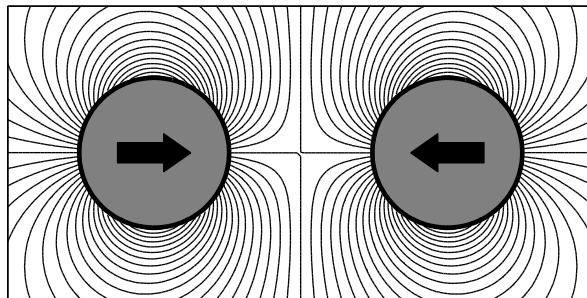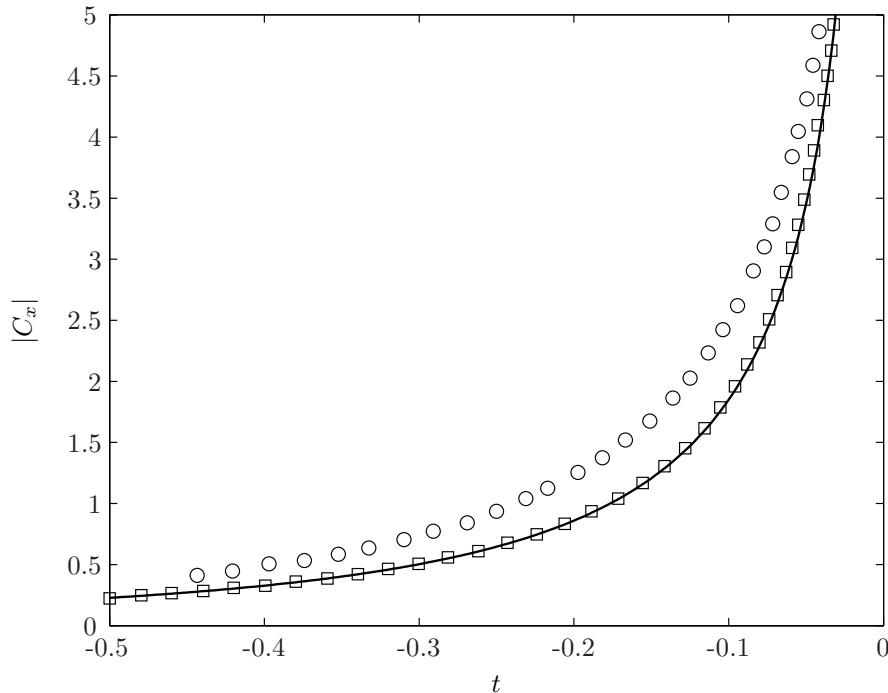
Figure 4.5: Magnitude of the force coefficient $|C_x|$ when two cylinders moves toward each other at constant velocity as depicted in Figure 4.4. The two cylinders impact at $t^* = 0$. ——— , present method; □ , Bampalas and Graham (2008); ○ , Wang (2004).

As previously discussed, when the bodies become closer in proximity more terms in the expansion (4.25) are retained for an accurate representation in the truncated series. Given in Figure 4.6 is the convergence of the coefficients a_j when the cylinders are separated by a distance $\epsilon/D = 0.01$ to highlight the spectral convergence of the Laurent coefficients in this case. The square of the magnitude of the jth term is machine precision small at $j \approx 150$. For the investigations hereafter, a minimum separation distance of $\epsilon/D = 0.01$ is maintained.

4.4.4 Coupled dynamics of two circular cylinders

For coupled cylinder interactions we use Equation (4.20). The equations are integrated using a variable-time step explicit Runge-Kutta solver in MATLAB (i.e. the `ode45` package) with strict relative and absolute tolerances on the error in the solution (10^{-6} and 10^{-8} respectively). Here we study two different types of cases. First, we investigate the influence that a cylinder with prescribed motion has on a cylinder that is allowed to freely interact with the flow (forced-free interaction).
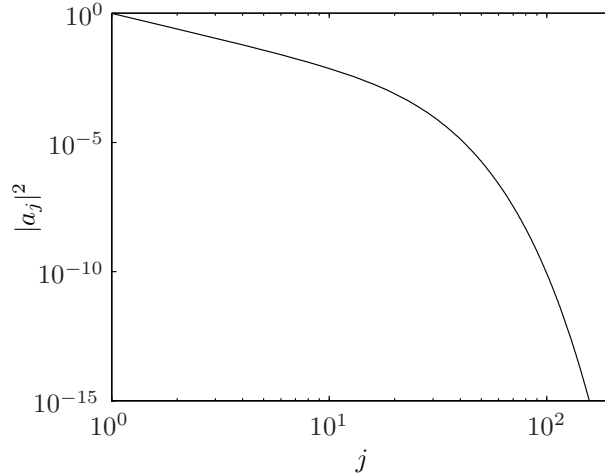
Figure 4.6: Convergence of $|a_j|^2$ versus j. For the negative terms, the scaled coefficients, $a_{-j}\rho_2^{-j}$, reveal the same trend.

Second, we study the case where both cylinders are given an initial condition and allowed to interact freely with one another (free-free interaction). In what follows it is assumed that each body is of equal radius, $r_1 = r_2$, and neutrally buoyant, $\rho_{\mathrm{b},k} = \rho_{\mathrm{f}}$.

Forced-free interaction applied to hydrodynamic drafting

In this section we prescribe the motion of first body and allow the second body to move freely in the flow. One particular area of application is to characterize how bodies forward of another body affect the hydrodynamic performance of the aft body. Here we look to investigate the benefits that the aft body receives in "riding" behind the forward cylinder that has a prescribed motion, primarily to determine good drafting regions. We first initialize both cylinders to have unit velocity in the x-direction, i.e. $U_k = 1$. It is assumed that the forward body travels at a uniform speed $U_1 = 1$ (which means there must be an external force on it). No external force is applied to the second body so it moves in response to the resultant fluid forces. A few examples are given in Figure 4.7. If the aft cylinder sits in a narrow band directly behind the forward cylinder, its velocity is decreased. On the other hand, the aft cylinder is capable of maintaining or overtaking the forward cylinder with no added force if it sits more towards the forward cylinder's side. In one case it is seen that the aft cylinder is ejected in the y-direction due to the large side force generated from the motion of the forward cylinder.
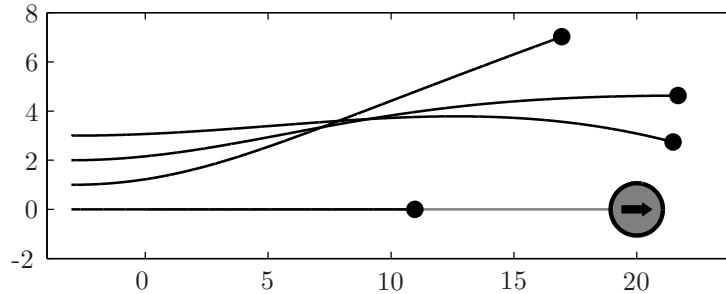
Figure 4.7: Several example paths of an aft cylinder following the forced motion of a forward cylinder. Both cylinders are initially moving to the right with unit speed. Black lines denote the paths of the passive cylinder, ● denotes the centroid location at $t = 20$, and the gray line denotes the path of the forward cylinder. The forward cylinder is forced at a constant velocity starting from $z_1(0) = 0$. The initial locations for the aft cylinder are $z_2(0) = -3, -3 + i, -3 + 2i$, and $-3 + 3i$.

To further elucidate the effect of drafting for the aft body we look at the forces that the aft body experiences due to the presence of the forward body. In a perfect fluid a single cylinder in an unbounded flow travels with no drag and thus does not require any energy input to maintain its velocity. Thus we look for the regions in a force contour map where the aft cylinder receives an additional thrust due to the motion of the forward body. This extra force assists the aft body to overcome the drag it is to experience if in a viscous fluid. Plotted in Figures 4.8(a) and 4.8(b) are the thrust force and side force experienced by the aft body, respectively. Although it may seem beneficial to draft directly behind the lead cylinder since fluid rushes to fill the forward mass, doing so actually hinders the following body substantially. The aft body receives an induced hydrodynamic drag due to the high-pressure region created between the bodies. Thus as seen in a particular path in Figure 4.7 where the aft body is initialized directly behind the forward cylinder, the separation between the two increases as they move toward the right. Alternatively, if the aft cylinder sits in an area slightly behind the forward cylinder's midline but above the 30 degree angle line (see Figure 4.8(a)) the forward cylinder experiences a thrust force allowing the aft cylinder to be propelled beyond the forced cylinder as seen in a few of the example pathlines given in Figure 4.7. This force increases as the distance between the cylinders is reduced and reaches a finite value in the limit that the separation is the sum of their radii. In addition to the thrust force, the aft body can experience a significant side force as seen in 4.8(b). In many applications, such as the drafting of neonate dolphins behind their mothers, the side force can be a substantial limiting factor on the effectiveness
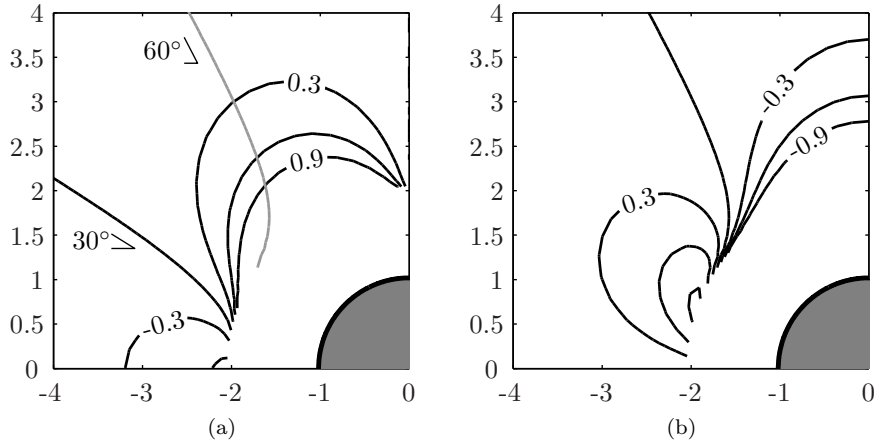
Figure 4.8: Contour plots for the force on an aft cylinder drafting behind another cylinder of equal radius. Both the lead cylinder and trailing cylinder move to the right with $U_1 = 1$. (a) Thrust force acquired by the aft cylinder based on the location of its center. The gray curve indicates the location where the side force on the aft body is exactly zero. (b) Side force on the aft cylinder. Contours on all plots are separated by an increment of 0.3.

of drafting. In Figure 4.8(a) the line of zero side force is shown in gray to give a sense of the location where the aft cylinder feels zero side force thus allowing the aft cylinder to stay near the body without being pushed away or colliding with the forward cylinder. This line indicates that the preferred location for drafting and is roughly inclined at an angle of 60 degrees from the trailing edge of the forward cylinder.

Free-free interaction applied to the collision of two cylinders

We now investigate the dynamics of two circular bodies that are allowed to interact with one another given a specific set of initial conditions. As a specific example, the collision of two circular cylinders is studied to illustrate the effect of the fluid on the resultant motion of the cylinders before and after impact.

Consider the assumed collision of two cylinders. When two circular cylinders collide, momentum along the line of contact is transferred between the two bodies. For a perfectly elastic collision, this transfer of momentum between the two bodies must satisfy both conservation of total momentum and the conservation of energy. We seek to enforce this when the two bodies collide and to do so, expressions for the total momentum and energy are derived and used to determine the resultant

velocities after impact. The momentum of both the bodies and the fluid is written as an integral over the entire plane, D,

$$\mathbf{P} = \int_D \rho_f \mathbf{u} \, dA = m(\mathbf{U}_1 + \mathbf{U}_2) + \rho_f \int_{D_f} \nabla \Phi \, dA \qquad (4.26)$$

where explicit integration over the two bodies leaves us with the standard expression for momentum of two rigid bodies, each with mass m, and an expression for the fluid momentum as an integral over the region occupied by the fluid, D_f. By applying the divergence theorem to the area integral over the fluid region, Equation (4.26) can be rewritten

$$\mathbf{P} = m(\mathbf{U}_1 + \mathbf{U}_2) - \oint_{\partial D_1 + \partial D_2} \Phi \, \hat{\mathbf{n}} \, ds. \qquad (4.27)$$

Now, we take the vector Equation (4.27) and transform it to complex notation, $\mathbf{P} \mapsto P = P_x + iP_y$, by noting that the complex version of the normal can be represented with $\hat{\mathbf{n}} \mapsto -i(dz/ds)$ and recalling that $\Phi = \text{Re}[W]$. Thus

$$P = m(U_1 + U_2) + \rho_f \oint_{\partial D_1 + \partial D_2} \text{Re}[W] \, dz. \qquad (4.28)$$

Similarly, the expression for kinetic energy is written as

$$\begin{aligned} E &= \frac{1}{2} \int_D \rho_f \left(\mathbf{u} \cdot \mathbf{u} \right) \, dA \\ &= \frac{m}{2} (|\mathbf{U}_1|^2 + |\mathbf{U}_2|^2) + \frac{\rho_f}{2} \int_{D_f} (\nabla \Phi \cdot \nabla \Phi) \, dA \end{aligned} \qquad (4.29)$$

where the last integral is the kinetic energy of the fluid alone. The area integral for the kinetic energy of the fluid in (4.29) can be transformed to a contour integral by applying Green's theorem and noting that $\nabla^2 \Phi = 0$. Thus

$$\int_{D_f} (\nabla \Phi \cdot \nabla \Phi) \, dA = -\int_{\partial D_1 + \partial D_2} \Phi \frac{\partial \Phi}{\partial n} \, ds + \int_{\partial D_\infty} \Phi \frac{\partial \Phi}{\partial n} \, ds \qquad (4.30)$$

where ∂D_∞ is a contour that extends to infinity. The last integral in (4.30) is exactly zero due to the continuity equation and the requirement that Φ must be a constant at infinity, thus, when placing in complex form, (4.29) reads

$$E = \frac{m}{2}\left(|U_1|^2 + |U_2|^2\right) - \frac{\rho_f}{2}\oint_{\partial D_1}\text{Re}[W]\,\text{Re}\left[-i\overline{U}_1\,dz\right] - \frac{\rho_f}{2}\oint_{\partial D_2}\text{Re}[W]\,\text{Re}\left[-i\overline{U}_2\,dz\right]. \qquad (4.31)$$

Equations (4.28) and (4.31) must be conserved following a collision event.

To model a collision a threshold value ϵ is chosen such that when separation between the cylinders is below this value a collision takes place. This threshold value is selected to be $\epsilon = 0.01D$ for all the cases presented here. If a collision event occurs at $t = t_c$ while the equation of motion (4.20) is integrated, the pre-impact velocities are decomposed into two components, a component that is along the line of collision, $U_{k,n}(t_c^-)$, and a component that is tangent to the line of collision, $U_{k,t}(t_c^-)$. The change in resultant velocity after a collision must only take place in the direction along the line of collision while conserving both the total momentum and energy of the system. For example, in the absence of the fluid, closed-form expressions for the post-impact normal velocities of the two equal mass cylinders are easily found to be $U_{1,n}(t_c^+) = U_{2,n}(t_c^-)$ and $U_{2,n}(t_c^+) = U_{1,n}(t_c^-)$ while the tangential component remains the same. With the presence of the fluid, we resort to numerically determining the post-impact normal velocities $U_{k,n}(t_c^+)$ by ensuring that the total normal momentum is conserved, $P_n(t_c^+) = P_n(t_c^-)$, and that the total energy is conserved, $E(t_c^+) = E(t_c^-)$.

As an example, an oblique collision event is plotted in Figure 4.9. Here, a cylinder starting from the left is initialized with $U_1(0) = 1$ and $z_1(0) = -6 + i$ and allowed to interact with the second cylinder initially at rest with $U_2(0) = 0$ and position $z_2(0) = 0$. In the presence of the fluid the cylinders collide at $t = 4.45$. The paths for such a situation are given in Figure 4.9 as black lines. For comparison, the paths for the case where the fluid is absent are also plotted as dashed lines. One can see a distinct difference between the two paths due to the presence of the fluid.

To validate this type of behavior the evolution of momentum and energy for the fluid, each body, and the entire system are plotted in Figure 4.10. It is easily seen that the total momentum and
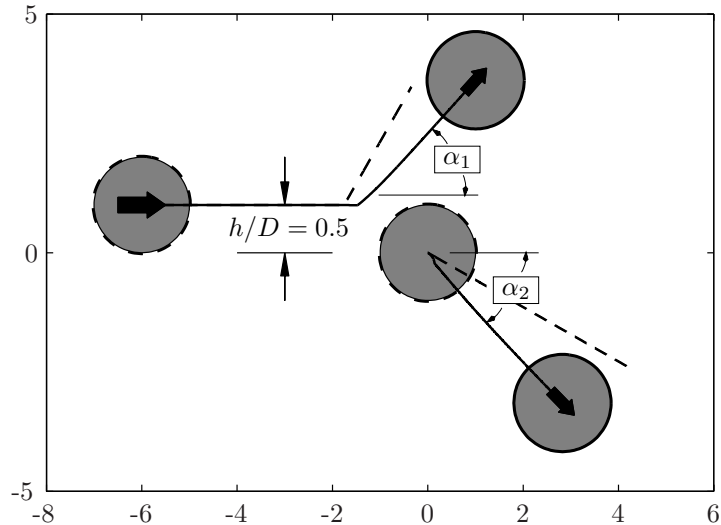
Figure 4.9: Paths of two cylinders in a collision event. The dashed filled cylinders indicate the initial locations and velocities ($U_1(0) = 1$, $U_2(0) = 0$, $z_1(0) = -6 + i$, and $z_2(0) = 0$) while the solid filled cylinders indicate the resultant locations and velocities at $t = 10$. In addition to the paths taken by the cylinders in an inviscid fluid (solid) the paths of a perfect collision in the absence of the fluid are also plotted (dashed) for comparison. Arrows scale with the magnitude of velocity. h/D is measured from the origin (i.e. the initial location of the stationary cylinder).

energy of the system is conserved in addition to providing more justification for the use of (4.20) for modeling FSI in potential flow. In all instances presented here, the normalized variations in total momentum and kinetic energy are maintained at $\mathcal{O}(10^{-3})$ or less. It is interesting to observe that the fluid momentum and energy is continuous at the instant of collision (although non-smooth). The lack of the jump in the fluid momentum actually indicates that at the time of impact, the transfer of momentum between the two bodies is conserved, that is even though we enforce the requirement that the *total* momentum of the entire fluid-body system be conserved, the collision itself degenerates into satisfying only the momentum transfer between the two bodies. In essence, at the time of collision, the fluid can be neglected, although the fluid plays an important role in deflecting and buffering the two bodies prior to collision, thus drastically affecting the resulting trajectories of both the impinging cylinder and the target cylinder by changing the line of impact.

Futhermore, it is also important to distinguish the difference between the fully coupled FSI and the prescribed motion case. As observed in Section 4.4.3, the prescribed collision of two cylinders creates an unbounded force approaching impact. Intuitively, one thinks this suggests that a collision
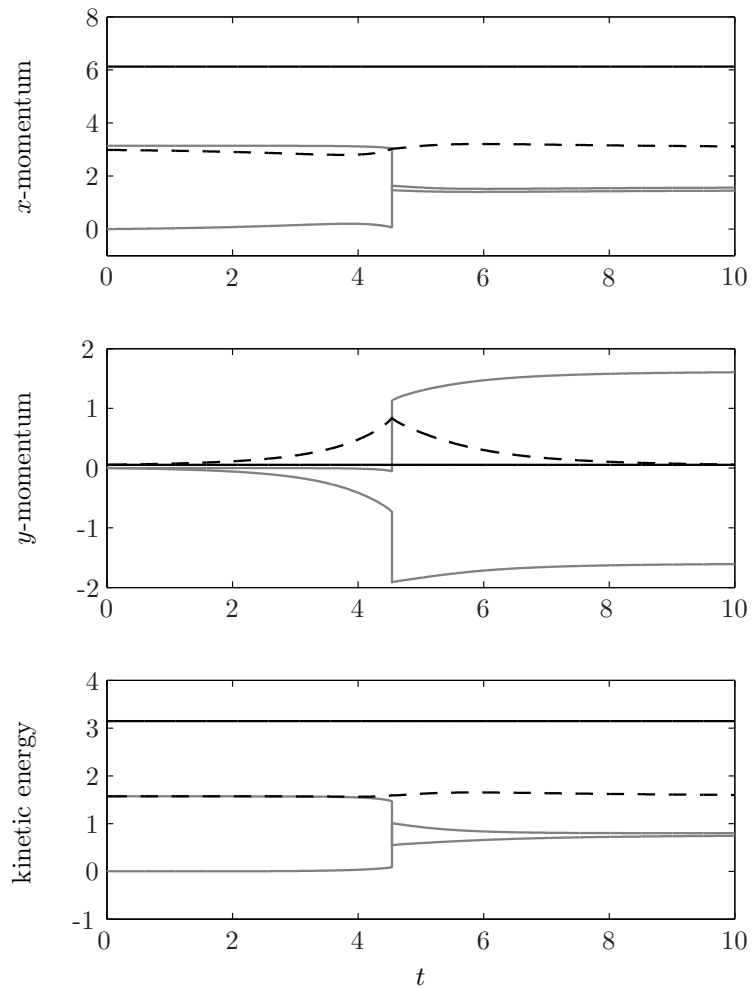
Figure 4.10: The momentum, P, and kinetic energy, E, of the fluid (dashed), each body (gray), and total system (black) are given for the oblique collision event presented in Figure 4.9. The collision occurs at $t = 4.45$.
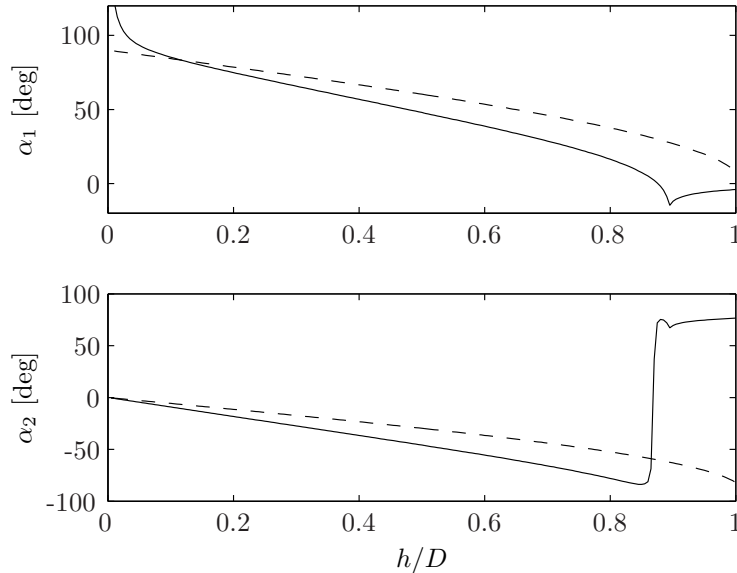
Figure 4.11: Angles, α_1 and α_2 that the cylinders are deflected versus h/D after an oblique collision with the second cylinder initially at rest. With fluid present (solid) and without the fluid present (dashed).

can never occur because the forces become increasingly large as the cylinders approach. The key contrast in the FSI case is that the bodies undergo deceleration as well and this in turn affects the forces on the body. Obviously, if one thinks of the notion of forces in this FSI case, they are counteracted by the inertia of the bodies, $m\dot{U}_k$, and remain bounded up until the moment of the modeled impact as seen in Figure 4.10. Thus it is hard to conclude from a prescribed interaction that there are any convincing trends for the FSI of multiple bodies.

Plotted in Figure 4.11 are $\alpha_1 = \arg(U_1(\infty))$ and $\alpha_2 = \arg(U_2(\infty))$, i.e. the angles that the post-collision velocity of the impinging and target bodies make with the horizontal versus an impinging obliqueness measure, h/D (see Figure 4.9 for definitions). When the two bodies have an inline impact, the impinging cylinder slightly rebounds at a very low speed and thus we see $\alpha_1 > 90°$ when $h/D < 0.1$. In these cases, nearly all the momentum is trasferred to the target cylinder. As Figure 4.11 demonstrates, when $0.1 < h/D < 0.8$, the difference between a collision without the fluid and with the fluid is that the impact is more shallow due to the fluid slightly moving the target cylinder away from the impact. In the region $0.845 < h/D < 0.895$, the collision is so shallow that the initially stationary cylinder actually begins to move to fill the void of fluid following the impinging
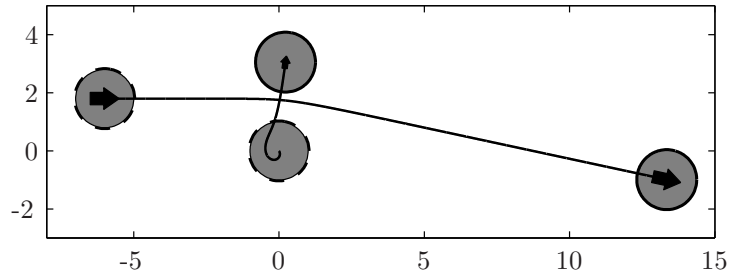
Figure 4.12: Cylinder paths for a near-collision event. The initial conditions are $U_1(0) = 1$, $U_2(0) = 0$, $z_1(0) = -6 + 1.8i$, and $z_2(0) = 0$).

cylinder, albeit at a very small resultant velocity, thus the tendency for the second cylinder to have a positive α_2. When $h/D > 0.895$, the incoming cylinder narrowly misses the target cylinder whereas when the fluid is absent the cylinders actually collide. In this sense, the fluid acts as a buffer to avoid a collision. However, the fluid facilitates a transfer of momentum between the two cylinders through the low pressure region existing between the bodies and thus, without any direct contact between the cylinders, the incoming cylinder is deflected downward quite substantially. In addition, the initially stationary cylinder gains a substantial amount of momentum thus propelling itself primarily in y-direction. This process is illustrated in Figure 4.12 and demonstrates a substantial hydrodynamic drift for the target cylinder in the direction transverse to the dominant motion in the fluid. For this specific case where $U_1(0) = 1$, $U_2(0) = 0$, $z_1(0) = -6 + 1.8i$, the resultant velocities of the bodies are $U_1(\infty) = 0.954 - 0.205i$ and $U_2(\infty) = 0.030 + 0.216i$. As h/D increases, the influence that the fluid has on the interaction of the two bodies begins to degrade rapidly.

4.5 A pair of flapping parallel plates

An additional example is given here to highlight the use of the method for more complex body shapes. Here a brief account of applying the method to a pair of flapping plates is given.

4.5.1 Conformal map

Consider two parallel flat plates defined by the two angles, χ and β, separation distance, l, plate chord length for each plate, c, and mid-point location, z_0, as depicted in Figure 4.13. The conformal
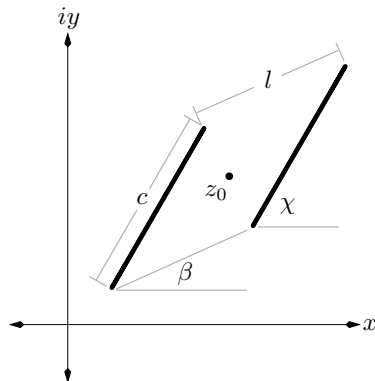
Figure 4.13: Geometric quantities defining the configuration of two parallel plates in z-plane.

map taking the annulus to the two parallel plates is given by

$$z = \tau\big(K(\zeta/\sqrt{\rho_2}, \rho_2) - \exp(2i\nu)K(\zeta\sqrt{\rho_2}, \rho_2) - K(-1, \rho_2) - \exp(2i\nu)K(-\rho_2)\big) + z_0 \qquad (4.32)$$

where

$$K(\zeta, \rho_2) = 1 - 2\zeta\frac{P'(\zeta, \rho_2)}{P(\zeta, \rho_2)}$$

and

$$P(\zeta, \rho_2) = (1 - \zeta)\prod_{j=1}^{\infty}(1 - \rho_2^{2j}\zeta)(1 - \rho_2^{2j}\zeta^{-1})$$

is the *Schottky-Klein prime function* for the annulus domain (Crowdy and Marshall, 2006). The parameters τ, ρ_2, and ν in Equation (4.32) are all functions of time and can be determined implicitly (e.g. using Netwon's method) by enforcing the geometric conditions on β, χ, c, and l defining Figure 4.13. Note that we can conveniently set $\theta_k = \chi$.

4.5.2 Sinusoidal flapping and pitching

Here, the configuration is restricted to $\beta = 0$ and $c = l = 1$ such that the plates are always stationed at the same y-location. A flapping-like wing motion is chosen such that the remaining geometric
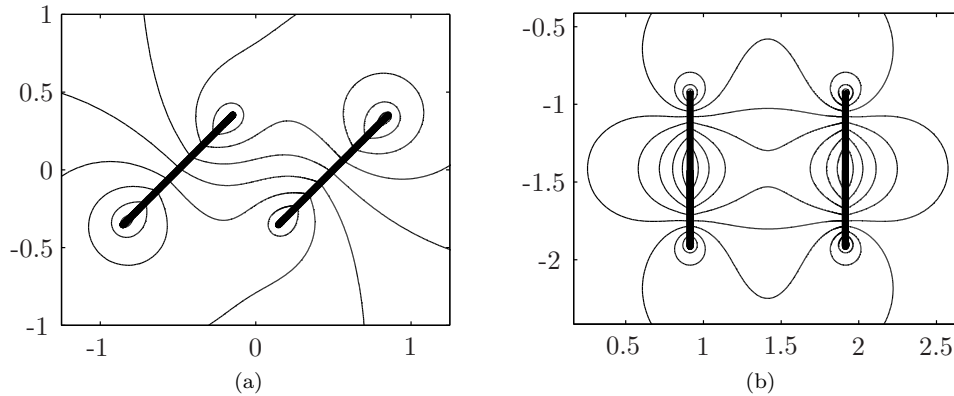
Figure 4.14: Instantaneous streamlines for the flapping motion of two parallel plates with motion prescribed by Equation (4.33). (a) $t = 0$. (b) $t = \pi/2$.

parameters are prescribed as follows:

$$z_0 = \exp\left(-\frac{i\pi}{4}\right)\sin(t),$$
(4.33a)

$$\chi = \frac{\pi}{2}\left(1 - \frac{1}{2}\cos(t)\right).$$
(4.33b)

The prescribed motion gives the downstroke a large angle of attack while the upstroke maintains a relatively small angle of attack (relative to the motion of the plates). Although idealized, the motion can be seen as a model of a dragonfly wing beating where the fore and hindwings are in phase.

The solution for the potential is given by (4.10) with the coefficients (4.15) determined numerically by the method discussed in 4.2.2. Figure 4.14 gives the streamlines during two instances of the flapping motion prescribed by (4.33). Figure 4.14(a) shows the streamlines at $t = 0$ where the angle of attack is $90°$ and $\Omega_1(0) = \Omega_2(0) = \dot\chi(0) = 0$. Alternatively, Figure 4.14(b) depicts the streamlines at $t = \pi/2$ when the plates are experiencing pitch reversal for the upstroke. Here, the angular velocity is at a maximum $\dot\chi(t)(\pi/2) = \pi/4$ while there is no translational velocity.

Care must be taken to integrate (4.18) and (4.19) since the mappings include four zeros on the annuli representing the four sharp edges in the physical plane. This in turn introduces four poles lying on the contours when attempting to integrate (4.18) and (4.19). To make progress, the integration contour is stretched slightly into the fluid domain avoiding the singularities. The resulting force and moment coefficients acting about the plate centroids, z_k, in addition to the sum

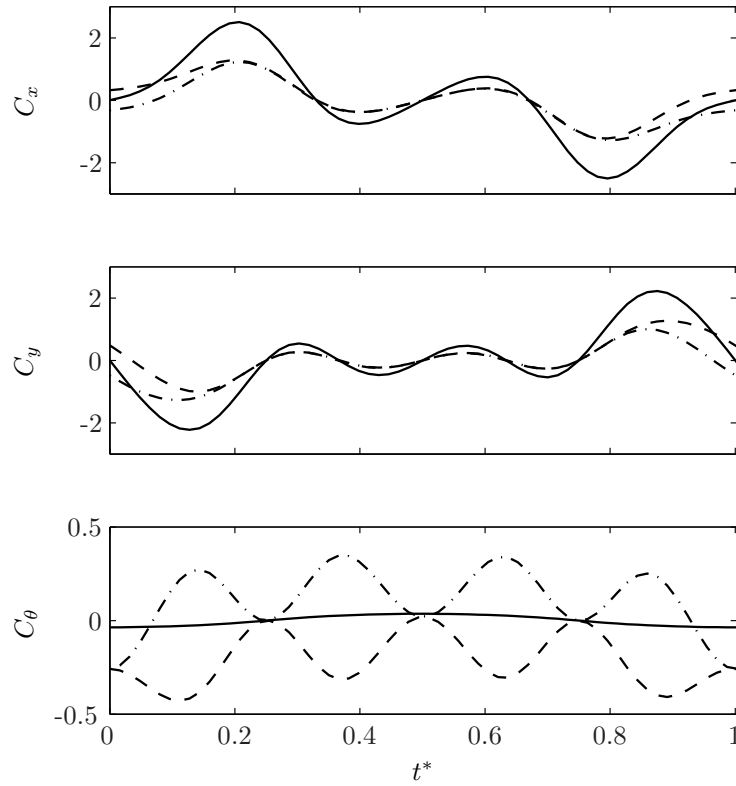Figure 4.15: Individual and total force and moment coefficients versus non-dimensinal time $t^* = t/(2\pi)$ of two plates undergoing motion prescribed by Equation (4.33) for one cycle. Lines indicate sum of $k = 1, 2$ (solid); $k = 1$ (dashed); $k = 2$ (dashed-dot). For C_θ, the solid line represents the sum of the total torque about z_0.

of each component (e.g. $C_x = C_{1,x} + C_{2,x}$) for a single cycle are given in Figure 4.15. A few observations can be made. Contrary to the potential flow around a single plate in the absence of circulation, each plate experiences a force and moment, and their sum is not simply zero. A net force and moment about z_0 may act on the entire system at any given instant in time, although the moment in this case is especially small. In addition, it appears that pitching in the positive χ-direction during pitch reversal affects the lift force substantially and actually decreases lift in pure potential flow. Furthermore, for this sinusoidal motion, the net lift and torque, $\int (C_x, C_y, C_\theta) \, \mathrm{d}t$, over one period is exactly zero. This suggests that although there are net forces and torques on the system at various instants in time, the sinusoidal motion restricts the net force and torque over one cycle to be zero.

4.6   Conclusion

A general method to solve for the complex potential of two bodies translating and rotating in a perfect fluid is derived. The formulation can be used to form the complex potential given the conformal map of an arbitrary doubly connected domain to the annulus domain. Having solved for the complex potential, generalized forms of the Blasius formulas from Sedov are used to calculate the forces and moments on both bodies by numerically evaluating contour integrals along each body in the annulus domain. The forces and moments can additionally be used to dynamically couple the two bodies to analyze their fluid-structure interaction.

This formulation can be used in various applications to study the dynamics of bodies that constitute a doubly connected domain with relative ease (e.g. Weis-Fogh mechanism, ground effect, dragon fly aerodynamics, etc). One specific case considered here is the problem of two interacting cylinders in a perfect fluid. Three subcases are studied. First, the motion of the cylinders is prescribed and the forces experienced by both cylinders are calculated to provide validation for this method. It is demonstrated that when one cylinder is forced to collide with a stationary cylinder, the forces experienced by both cylinders are in excellent agreement with previous published data. In addition, when both cylinders are prescribed to impact each other at equal and opposite velocities,

the agreement with previous data is also nearly exact.

In the second subcase the motion of one of the cylinders is prescribed and the second cylinder moves only subject to the fluid forces it experiences. The analysis of the "forced-free" interaction is applied in the context to the benefits of hydrodynamic drafting. It is shown, contrary to intuition, that drafting directly behind a second body leads to substantially increased induced drag for neutrally buoyant cylinders. When the body sits in a particular zone, the body is capable of receiving additional thrust to aid its ability to overcome an unmodeled viscous drag while experiencing very little adverse side force. For example, this coupling may help give more insight on why neonate dolphins, among other aquatic animals, follow obliquely as opposed to directly behind their mothers although we have neglected to model the effects of a possible separated flow (e.g. Weihs, 2004).

In the third subcase, two cylinders are allowed to dynamically interact with one another through their mutual induced forces specifically in oblique collision and near-collision events. It is seen that the fluid provides a buffering effect prior to collision by attempting to push the colliding cylinders away from each other, but not necessarily preventing collision. In some instances with the presence of the fluid the cylinders are capable of narrowly avoiding a collision, whereas in the absence of fluid the two cylinders experience a collision event. In addition to avoiding the collision, a substantial drift velocity in the direction normal to the motion of impinging body can be obtained.

Lastly, a brief example of a pair of flapping parallel plates is given to highlight the application of the proposed method in a more complicated domain. A dual wing configuration is further investigated in the context of flapping flight. It is found that the system is capable of sustaining a force or moment at any given instant of time, but under sinusoidal motion the net force and moment about the system centroid is exactly zero over an entire cycle. Though it is hard to draw any definitive conclusions without the inclusion of separated vortices in this high angle-of-attack application, it is clear that the sinusoidal pitching gives a hydrodynamic disadvantage in terms of producing net lift.

We would like to note that this two-dimensional study is highly idealized and does not capture many important effects of viscous, three-dimensional flows. Nevertheless, it is sensible to investigate this idealized system because it calls attention to several dynamical features that have remained

unexplored. Even in cases where bodies exhibit substantial three-dimensional effects, the method presented here can lead to important generalizations in an idealized configuration to give some intuition for fluid-structure interaction.

Chapter 5

Conclusion and future directions

5.1 Conclusions

This thesis has concentrated on developing several low-order techniques to study a variety of fluid-structure interaction (FSI) problems with one or two rigid bodies in a perfect fluid. In general, the techniques presented are based on potential flow theory with the possibility of point vortices in the flow and reduce to one or more ordinary differential equations that can be solved using standard time integrators. The techniques developed are general enough to apply to various applications ranging from aerodynamics of insect wings to the vortex-induced vibration of marine structures.

The first application area addressed is the FSI of an idealized flat-plate airfoil subject to a freestream flow. We assume that the airfoil is thin, at high Reynolds number, and does not experience any leading edge separation at any instant, thus a potential flow model with point vortices can be used to provide a low-order description of the wake dynamics in the fluid associated with the problem. In this case the aerodynamics model reduces to a single ordinary differential equation. Equations of lift and moment are derived from a conservation of linear and angular impulse argument and are adjusted for the effects of thickness and camber in the airfoil. The results of the model are compared to numerical and experimental results and are found to be quite reasonable given the simplicity of the model. The model is then used to show the application to the classical flutter problem. As an example several responses are given showing the unstable flutter phenomena resulting from the vortex-induced motion. It is also shown that for some regimes, multi-modal behavior is seen which

cannot be addressed using classical techniques. The model is further extended using the concept of trapped vorticity to model synthetic jet actuators for airfoil control. The extended model is validated with experiments and demonstrates relatively good agreement. We then use a lightly tuned, simple feedback algorithm to stabilize the system undergoing flutter. Further applications of the model with adaptive control is presented in Appendix B.

The second application considered is the coupled response of a general shaped body in the presence of point vortices and a freestream flow. The model developed for this case uses the Brown-Michael law for varying strength vortices shed from the body. If no varying strength vortices are present then the equation of motion for the vortices reverts back to the Kirchoff laws for vortex motion. Force and moment acting on the body is calculated using Sedov's integral formulas and then coupled to the rigid body dynamics of the body. The resulting system consist of $2N + 3$ real differential equations and possibly P algebraic equations for P varying strength vortices. Two examples are given here, both in context of the canonical mass-spring-damper system often studied for the characterization of vortex-induced vibrations. The circular cylinder is first considered in the absence of the freestream. It is seen that although the body motion seems chaotic, there is a limiting amplitude and its dependence versus initial vortex location is plotted. For more than one vortex, the chaotic motion makes it difficult to draw any concrete conclusions. We then allow a vortex street to impinge on the same canonical system but now in a freestream flow. We see that when the vortex street is spaced near the natural frequency of the structure, then the structure responds with large amplitude oscillations that can exceed $y_0/D = 3$. For vortex spacings shorter and longer than this, the response amplitude decreases. As another brief example, the model is applied to the flat plate geometry. Here a separation model is proposed and applied to a flat stationary plate and its Strouhal shedding frequency is found to be in a reasonable range. Additionally, an example of a spring-mass-damper system response is given to show the application of the method.

In the final application a general method is developed to solve the potential problem for two arbitrarily shaped bodies in rigid rotation and translation. Again, Sedov's equations are used to calculate the force and moment on both bodies. These forces are coupled with the body motion to

give two complex ordinary differential equations describing the dynamics if both bodies are allowed to act freely. We further study two geometries here as well. First, we study the case where both bodies are circular cylinders. For prescribed motion, the new method predicts the correct force (compared to previous studies) on the body for inline impacts. The analysis is also done where the motion of one body is prescribed and applied in the context of hydrodynamic drafting. It is found that for locations near the forced cylinder, but not directly behind the forced cylinder, the free cylinder can attain a substantial additional propulsive force. Furthermore, we examine the collision and near collision of two cylinders in a free-free simulation. It is seen that the fluid acts as a buffer, slightly deflecting the line of contact prior to collision. In some cases, a collision is avoided whereas in the absence of the fluid they would collide. As a final example, we briefly look at the interaction of two flat plates in a flapping like motion. It is found that the system can sustain a lift and moment at a given instant in time but for sinusoidal motion its net force and moment over a cycle is exactly zero.

5.2   Future directions

There is a myriad of applications for each model presented here. For the first model, it would be interesting to further study the flutter problem more rigorously. In particular, the linear model presented in Appendix B can be applied and a formal linear stability analysis could be conducted and compared to previous results of Theodoresen flutter theory. As far as the control problem is concerned, more work can be done to model the startup and release of the control vortex when actuation is turned on and off. In the current approach, the control vortex is instantaneously turned on based on the experimental evidence that suggests that the formation time is much faster than the convective time scale. A more accurate model of the starting process of the control vortex may lead to faster response times from the system when the model is used in a closed-loop adaptive controller.

We can also offer many future excursions for the model presented in chapter 3. Due to the large parameter space of the vortex-induced vibration cases, we have only presented a few examples of what can be done without rigorous analysis. More work is needed in characterizing and predicting

limiting amplitudes for both the circular cylinder and the flat-plate problem for various configurations of pre-existing and shed vortices. It is also appealing to analyze the onset of the free or constrained systems in the context of chaos. Furthermore, a vortex shedding model for smoothed bluff body flows may be of very important interest. Preliminary attempts seem to suggest that it is difficult to properly grow vortices from fixed separation points on the body. It may be necessary to apply an ad-hoc type model such as the one presented in Sarpkaya and Schoaff (1979) to properly model the vortex shedding off a circular cylinder for example. If a model of shedding off a smooth body could be successfully implemented, this would allow one to study vortex-induced vibrations for the canonical circular cylinder case and compare the results with experimental results.

There are many avenues for future research concerning the two-body potential flow problem. First and foremost, there are numerous doubly connected problems to investigate, ranging from Darrieus wind turbines to the flapping flight of small birds and insects. This method can be applied to all those instances to determine fluid-structure interaction in the absence of vortices. In particular, it would be interesting to examine and further analyze the two-wing model described in Section 4.5 for various motions of the airfoils (non-sinusoidal). This may elucidate the dynamics of flapping flight for dragonfly-like wing structures. Additionally, there is a need to determine a method to introduce vortices in this framework (unlike the integral representations used in Crowdy, 2010). This would open up many research topics in vortex dynamics for doubly connected domains. For example, one could use an unsteady vortex model like the one presented in Chapter 3 to describe the vortex shedding from sharp tips and apply it to flapping flight of the bi-wing geometry presented above.

Appendix A

Simulink models of the experimental apparatus

Given in Figures A.1, A.2, and A.3 are the three block diagrams that have been built to simulate the experimental facilities. These models have been originally built by Ali Turker Kutay at GTRI and have been modified by the thesis author. The complete Simulink model simulates the facilities in the configuration where the airfoil is allowed to only pitch about its quarter chord. The aerodynamic model of Chapter 2 has been included in the wing dynamics model as seen in Figure A.2.
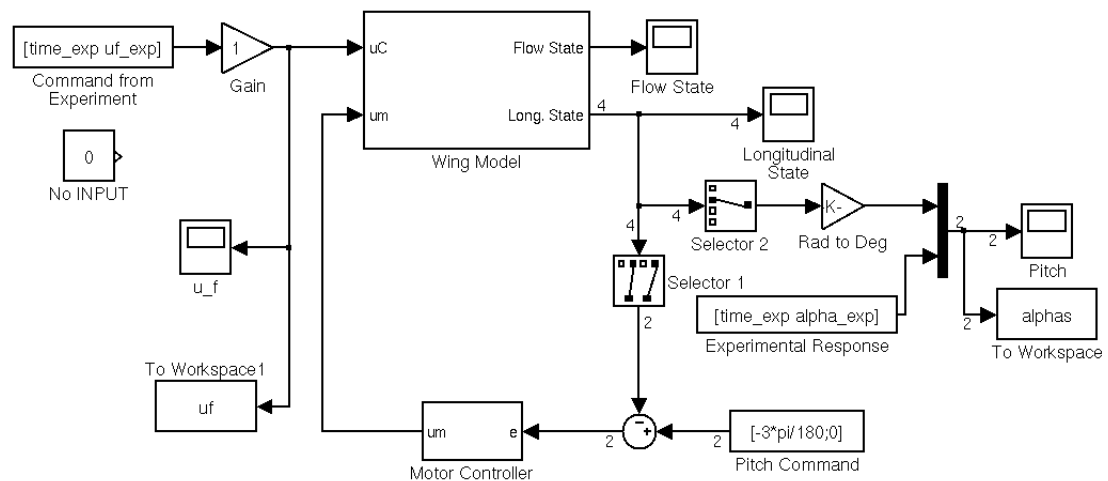

Figure A.1: Simulink model for the simulation of the experimental apparatus where the NACA 4415 airfoil is allowed to pitch only.
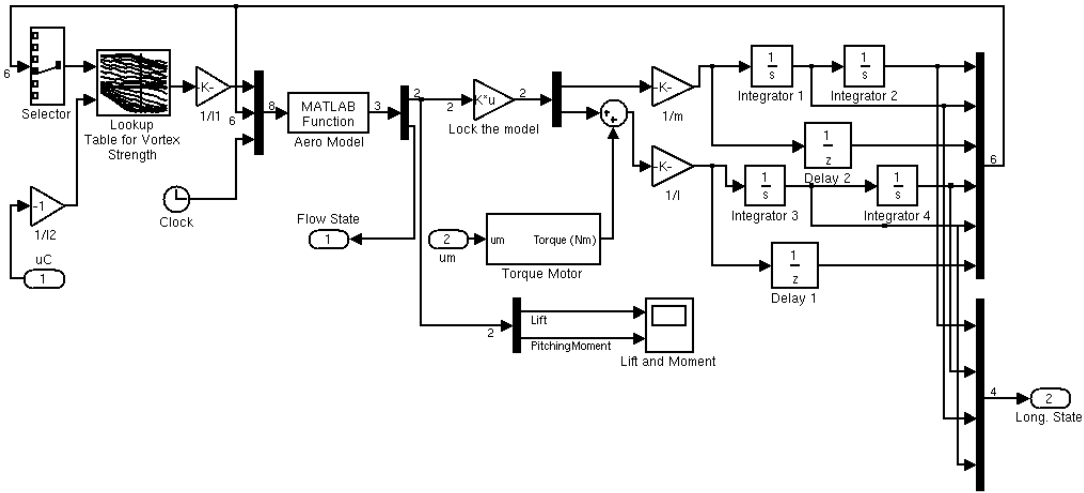
Figure A.2: Block diagram model for the wing aerodynamics and its structural response with the torque motor.
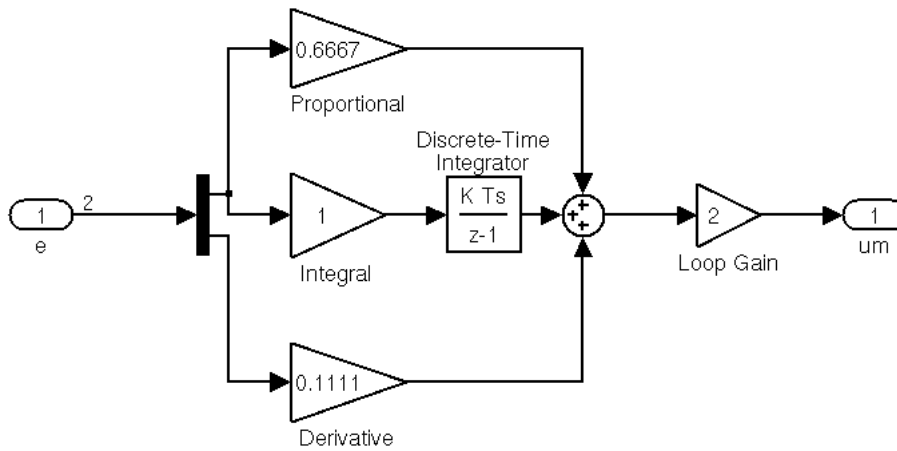
Figure A.3: Block diagram model for the torque motor that attempts to hold the wing at a constant AOA.

Appendix B

Vortex model based adaptive flight control using synthetic jets

This material, in part, was presented at the 2009 AIAA Guidance, Navigation, and Control Conference, in Chicago, Illinois (Muse et al., 2009) with the thesis author contributing as the second author. This appendix develops a simple linear model based on the results from chapter 2 and ties in control integration for the GTRI test bed. This section has its own notation due to the emphasis control design.

B.1   Introduction

The idea of using small, simple active flow control devices that directly affect the flow field over lifting surfaces sufficiently to create control forces and moments has attracted growing interest over the last decade. Compared to conventional control surfaces, flow control actuators have the potential benefits of reduced structural weight, lower power consumption, higher reliability, and faster output response. Significant work on open-loop flow control has already demonstrated control effectiveness on both static and rigidly moving test platforms. These studies have primarily focused on mitigation of partial or complete flow separation over stalled wing sections or flaps (Wu et al., 1998, Petz and Wolfgang, 2006). The lift and drag benefits associated with flow attachment enable control in a broader angle-of-attack range, however, these methods provide no direct control as they rely on conventional control surfaces for control actuation, and provide little benefit at moderate flight

conditions. A different approach to flow control that emphasizes fluidic modification of the apparent aerodynamic shape of the surface by exploiting the interaction between arrays of surface-mounted synthetic jet actuators and the local cross flow was recently developed (Smith and Glezer, 1998, Glezer and Amitay, 2002). With this approach bi-directional pitching moments can be induced by individually controlled miniature, hybrid surface actuators integrated with rectangular, high aspect ratio synthetic jets that are mounted on the pressure and suction surfaces near the trailing edge (DeSalvo and Glezer, 2004). An important attribute of this technique is that it can be effective not only when the baseline flow is separated but also when it is fully attached, namely at low angles of attack such as at cruise conditions.

Despite the amount of the effort devoted to active flow control technology in recent years, a majority of the work published depends on experience and intuition rather than on a fundamental understanding of the flow physics. This is due to the lack of an analytical formulation of the mechanism behind flow actuation. Even though various aspects of flow actuation have been investigated experimentally, mostly on steady models, it is still difficult to draw conclusions and predict performance on dynamic models. This presents a challenge for feedback controller design as the vast majority of control synthesis techniques are inapplicable.

In our recent studies, we demonstrated successful closed-loop control of pitch motion of a 1-DOF and 2-DOF wind tunnel model by using the aforementioned actuators with no moving control surfaces (Kutay et al., 2006, Muse et al., 2008a). First a linear controller was designed for the rigid body model of the test model by approximating the actuators as linear static devices. This controller worked well for slow maneuvers where the static actuator assumption holds. For faster maneuvers, requiring higher bandwidth controller design, interactions between the flow and vehicle dynamics get stronger and the linear rigid body model can no longer represent overall system behavior accurately. In these regimes, linear controllers that ignore effects of flow actuation have limited performance. A neural network (NN) based adaptive controller was introduced to improve the controller performance by compensating for the modeling errors in the design including the unmodeled dynamics of

actuation. It is assumed that the system dynamics can be written as

$$\dot{x} = Ax + B(u + \Delta(x, x_\mathrm{f}, u))$$

$$\dot{x}_\mathrm{f} = f(x, x_\mathrm{f}, u) \tag{B.1}$$

where x represents the rigid body states of the vehicle, x_f is the state vector associated with the dynamics of the flow, and $u = u_\mathrm{dc} - u_\mathrm{ad}$ is the control signal to the actuators with u_dc being the output of a linear dynamic compensator and u_ad the adaptive control signal. Matrices A and B form the linear system model used to design u_dc and Δ represents the modeling errors in rigid body dynamics and the couplings between the vehicle and unmodeled flow dynamics.

For slow maneuvers where changes in the flow field due to actuation occur much faster than the variations in the vehicle states, Δ remains comparatively small. In this case, the vehicle behavior approaches the linear design model and u_dc alone can control the system suffciently well. As the vehicle starts moving faster, vehicle-flow interactions get stronger and Δ becomes large enough to disturb the vehicles' predictable dynamics. The adaptive controllers proposed were shown on the experiment to successfully compensate for Δ for moderate bandwidths for a 1-DOF and a 2-DOF airfoil (Kutay et al., 2006, Muse et al., 2008a). The adaptive controller only used x and u feedback to compensate for Δ that is a function of x, u, and x_f . This is possible only if the x_f dependence of Δ is observable from x and u, which was evidently the case. For more aggressive maneuvers the observability assumption is likely to fail, or the dependence becomes much more complex. For such cases feedback from flow states is necessary to control the vehicle, which requires some information on $f(x, x_\mathrm{f}, u)$ and $\Delta(x, x_\mathrm{f}, u)$.

The objective of this research is to apply the low-order approximate flow model presented in chapter 2 to the wind tunnel setup at GTRI for simulation and control design. First, the low-order nonlinear model is linearized to allow for standard adaptive control practices. A unique feature of control designs using this model is that the control variable is a pseudo-control based on regulating the control vortex strength. The control design is based on an output feedback adaptive control

Δt	$\beta c/U$
5	0.406
10	0.360
20	0.333

Table B.1: Several values of β for various averaging times.

methodology that illustrates the effectiveness of using the model for achieving flight control at a higher bandwidth than achievable with a static actuator assumption. Since the linear model provides some information on f, this is incorporated into the linear part of the design (A and B matrices in (B.1)), effectively reducing the amount of modeling error that the adaptive controller must compensate. This provides superior results compared to conventional modeling techniques. Experimental examples on a unique dynamic wind tunnel traverse verify that tracking performance is indeed better than control designs employing standard actuator modeling assumptions. The reduced order model from our previous work will also be used to simulate the system with higher accuracy. This is crucial to allow for investigation of various control architectures without spending expensive wind tunnel time.

B.2   Control formulation

B.2.1   A simplified control design model

The vortex model by its nature captures some dynamics that are negligible on the time scales of a flight control system. From this perspective, it is reasonable to expect that it is possible to simplify the model further to make it appropriate for control design. When examining the lift and moment equations, (2.21) and (2.26), it is observed that they are a function of only the states of the rigid body (i.e. both the added mass and the quasi-steady terms) in addition to a term due to the wake. For example, consider the lift equation. In this case, the term due to the wake is simply

$$L_W = -\frac{\rho_{\mathrm{f}} U c}{2} \sum_{j=1}^{N} \frac{\Gamma_j}{\sqrt{x_j^2 - \frac{c^2}{4}}}.$$

Let us define a characteristic circulation due to the entire wake based on (B.2.1) as

$$\Gamma_W = c\sum_{j=1}^{N}\frac{\Gamma_j}{\sqrt{x_j^2 - \frac{c^2}{4}}}. \tag{B.2}$$

Even though the discontinuities of the flow (i.e. the startup of Γ_j and x_j) are included here, equation (B.2) is smooth. Hence, it is reasonable to model this term using an ordinary differential equation. To choose a satisfactory differential equation, we examine the startup problem where a only a single vortex is created. In this case

$$L = -\rho_f U\left(\Gamma_0 + \frac{\Gamma_W}{2}\right).$$

From classical theory, it is expected that half of the lift is attained at the moment the plate is impulsively started from rest. Thus, at $t = 0$, $\Gamma_W \approx \Gamma_0$. When $t \to \infty$, the lift term due to the wake term should disappear as the wake vortices move further and further away. Therefore we propose using the model

$$\frac{\mathrm{d}\Gamma_W}{\mathrm{d}t} = -\frac{\mathrm{d}\Gamma_0}{\mathrm{d}t} - \beta\Gamma_W$$

where β is a constant. Note that this introduces an exponential decay of Γ_W given a constant Γ_0. This is contrary to the classical square root like growth for the lift. The parameter β is chosen based to agree, in a least-squares sense, with the original nonlinear low-order model for a given non-dimensional time, Δt. Given in table B.1 are several values of β. In what follows, $\beta c/U = 0.406$ so that the more dynamic aspects of the wake circulation are maintained. From this, a linear model can be formed consisting of geometrical parameters and the derivatives of y_b and α. The differential equation governing the fluid dynamics reduces to a simple first order differential equation

$$\dot{\Gamma}_W + \beta\Gamma_W = -\pi c\left(\ddot{y}_b + \left(a + \frac{c}{4}\right)\ddot{\alpha} + U\dot{\alpha}\right) \tag{B.3}$$

with the initial condition

$$\Gamma_W(t_0) = -\pi c\left(\dot{y}_b + \left(a + \frac{c}{4}\right)\dot{\alpha} + U\alpha\right)_{t=t_0}.$$

Furthermore, the lift and moment expression simplify to read

$$L = -\rho_f \pi \left(\frac{c^2}{4} \ddot{y}_b + U c \dot{y}_b \right) + \rho_f \pi \left(\frac{ac^2}{4} \ddot{\alpha} + U c \left(a + \frac{c}{2} \right) \dot{\alpha} + U^2 c \alpha \right) - \frac{\rho_f U}{2} \Gamma_W - \rho_f U \Gamma_C \qquad \text{(B.4)}$$

and

$$M = aL + \frac{\rho_f \pi U c^2}{4} \dot{y}_b + \rho_f \pi \left(\frac{ac^2}{128} \ddot{\alpha} - \frac{U ac^2}{4} \dot{\alpha} - \frac{U^2 c^2}{4} \alpha \right) + \frac{\rho_f U c}{8} \Gamma_W - \rho_f U \Gamma_C x_C. \qquad \text{(B.5)}$$

B.2.2   Linear control algorithm

For control design it is desirable to rewrite the simplified equations of motion as a matrix quadruple. To this end, we can combine equations (B.4), (B.5), (2.38), and (2.39) to form the rigid body differential equations as

$$M \begin{bmatrix} \ddot{y}_b \\ \ddot{\alpha} \end{bmatrix} + D \begin{bmatrix} \dot{y}_b \\ \dot{\alpha} \end{bmatrix} + K \begin{bmatrix} y_b \\ \alpha \end{bmatrix} + A \Gamma_W = B \Gamma_C \qquad \text{(B.6)}$$

where the mass, damping, and stiffness matrices are given by

$$M = \begin{bmatrix} m + \frac{\rho_f \pi c^2}{4} & -S_x + \frac{\rho_f \pi ac^2}{4} \\ -S_x + \frac{\rho_f \pi ac^2}{4} & I_\alpha + \frac{\rho_f \pi a^2 c^2}{4} + \frac{\rho_f \pi c^4}{128} \end{bmatrix},$$

$$D = \begin{bmatrix} b_y + \rho_f \pi U c & \rho_f \pi U c \left(a + \frac{c}{2} \right) \\ \rho_f \pi U c \left(a - \frac{c}{4} \right) & b_\alpha + \rho_f \pi U a \left(a + \frac{c}{4} \right) \end{bmatrix},$$

and

$$K = \begin{bmatrix} k_y & \rho_f U^2 c \\ 0 & k_\alpha - \rho_f \pi U^2 c \left(\frac{c}{4} - a \right) \end{bmatrix}.$$

The aerodynamics coupling matrix and control matrix are given respectively as

$$
A = \begin{bmatrix} \frac{\rho_f U}{2} \\ \rho_f U \left(\frac{4a-c}{8} \right) \end{bmatrix}, \quad B = \begin{bmatrix} -\rho_f U \\ -\rho_f U \left(x_C + a \right) \end{bmatrix}.
$$

The governing relation for aerodynamics in equation (B.3) combined with (B.6) is used to form the required matrix quadruple

$$
\dot{\overline{x}} = \overline{A}\overline{x} + \overline{B}\Gamma_C
$$

$$
y = \overline{C}\overline{x} + \overline{D}\Gamma_C \tag{B.7}
$$

where the system state is $\overline{x} = [y_b, \ \alpha, \ \dot{y}_b, \ \dot{\alpha}, \ \Gamma_W]^T$ and

$$
\overline{A} = \begin{bmatrix} 0 & I_\alpha & 0 \\ -M^{-1}K & -M^{-1}D & -M^{-1}A \\ \pi c \left(1 + \left(a + \frac{c}{4} \right) \right) M^{-1}K & \pi c \left(1 + \left(a + \frac{c}{4} \right) \right) M^{-1}D & \pi c \left(1 + \left(a + \frac{c}{4} \right) \right) M^{-1}A - \beta \end{bmatrix},
$$

$$
\overline{B} = \begin{bmatrix} 0 \\ M^{-1}B \\ -\pi c \left(1 + \left(a + \frac{c}{4} \right) \right) M^{-1}B \end{bmatrix}, \quad \overline{C} = \begin{bmatrix} 1 & 0 & 0 & 0 & 0 \\ 0 & 1 & 0 & 0 & 0 \\ 0 & 0 & 1 & 0 & 0 \\ 0 & 0 & 0 & 1 & 0 \end{bmatrix}, \quad \overline{D} = \begin{bmatrix} 0 \\ 0 \\ 0 \\ 0 \end{bmatrix}.
$$

Note that the control term Γ_C is a physical variable that is related to control voltage and the system states. This relationship will be explored in more detail later in the Appendix. Also, not all of the states are measurable. If all of the states are measurable, it is easy to formulate a control design based on linear-quadratic-regulator (LQR) theory. In this paper, the nominal control design consists of a robust servomechanism LQR control law with augmented feed forward term to improve transient

error tracking response. Consider the linear time invariant state space model

$$\dot{x} = Fx + Gu + Ew$$

$$y = Hx \tag{B.8}$$

where $x \in \mathcal{R}^n$, $u \in \mathcal{R}^m$, $w \in \mathcal{R}^m$, and $y \in \mathcal{R}^l$. Furthermore, it is assumed that w is an immeasurable disturbance. Next the command input vector, $r \in \mathcal{R}^p$ is defined such that r satisfies the differential equation given by

$$r^{(p)} = \sum_{j=1}^{p} a_j r^{(p-j)}. \tag{B.9}$$

Assuming that $p < l$ and defining the error signal as

$$e = y_b - r$$

and given the control objective that the command error $e(t) \to 0$ as $t \to \infty$ in the presence of undisturbed disturbances satisfiying equation (B.9), it is possible to design an optimal stabilizing control law for the plant dynamics given in (B.8). The solution of this standard formulation is derived in Wise (2007) and yields that nominal control signal of the form

$$u = -K_e \int_0^t e(\tau)\, d\tau - K_x x. \tag{B.10}$$

Letting r satisfy $\dot{r} = 0$, the LQR based technique yields an integral action on the tracing error that allows for robust tracking of commands with zero steady state error. Augmenting the control law in (B.10) with a feed-forward term, Z, and allowing for an additional augmenting control input for adaptive control design, Δu, the final nominal control law is given by

$$u = -K_e \int_0^t e(\tau)\, d\tau - K_x x + Zr + \Delta u. \tag{B.11}$$

Graphically this can be represented as the simulation diagram shown in figure B.1.
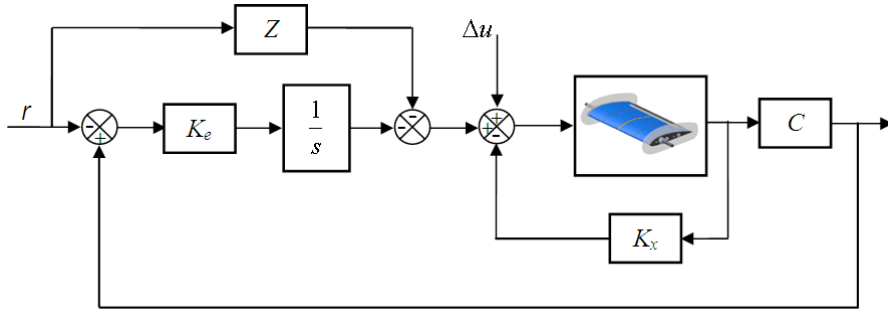
Figure B.1: Robust servo LQR with feed-forward element and added control signal.

The effect of the feed-forward term is to help speed up the transient response of the control law. From a frequency domain standpoint, the eigenvalues of the closed loop system remain fixed under a constant gain Z. In a single-input/single-output system, this is equivalent to adding an adjustable zero that allows the designer to cancel a slow pole in closed loop transfer function $Y(s)/R(s)$.

Since the system is not full state feedback, we use the static projective control technique of Wise (2007) to formulate an output feedback law without feedback of the flow state. Augmenting the model dynamics with the control law dynamics, the closed loop system is given by

$$
\begin{bmatrix} e \\ \dot{x} \end{bmatrix} = \begin{bmatrix} 0 & C_t \\ -\overline{B}K_e & \overline{A} - \overline{B}K_x \end{bmatrix} \begin{bmatrix} \int e \\ x \end{bmatrix} + \begin{bmatrix} -1 \\ \overline{B}Z \end{bmatrix} r
$$

$$
y_t = \begin{bmatrix} 0 & C_t \end{bmatrix} \begin{bmatrix} e \\ x \end{bmatrix}
$$

where C_t is a matrix that multiplied by x that gives the plunge position, z . Since we are not using the flow state in feedback we can retain all but two of the closed loop eigenvalues. Let $K = [K_e, K_x]$ and X_y be the eigenvectors corresponding to the closed loop eigenvalues we wish to retain. Then the required output feedback gain is computed as

$$
\overline{K} = K X_y \left(\overline{C_{\text{meas}}} X_y \right)^{-1}
$$

where $\overline{C}_{\text{meas}}$ corresponds to measured states of x such that $y_{\text{meas}} = \overline{C}_{\text{meas}} x = \begin{bmatrix} \int e, \ y, \ \alpha, \ \dot{y}, \ \alpha \end{bmatrix}^T$.

The projective control effort is then defined by

$$\Gamma_{\mathrm{C}} = -\overline{K} \begin{bmatrix} \int e \\ y_{\mathrm{meas}} \end{bmatrix} + Zr.$$

Though the technique does not guarantee closed-loop stability, in practice, closed-loop stability is easily satisfied.

B.2.3   Augmenting output feedback adaptive control

The assumed linear dynamics of the model (B.7) ignores nonlinearities and unmodeled dynamics associated with the flow actuation process. It is assumed that the true dynamics of the system can be represented as

$$\dot{x} = \overline{A}x + \overline{B}\Lambda(\Gamma_{\mathrm{C}} + f(x, \Gamma_{\mathrm{C}}))$$

$$y = Cx \tag{B.12}$$

where C is a matrix capturing the system output, $A \in \mathcal{R}^{n \times n}$, $B \in \mathcal{R}^{n \times m}$, and $C \in \mathcal{R}^{m \times n}$ are known matrices. $\Lambda \in \mathcal{R}^{m \times m}$ is unknown but is constant and positive definite, $x \in \mathcal{R}^n$ is the system state, $u \in \mathcal{R}^m$ is the control input, $y \in \mathcal{R}^m$ is the system output, and $f : \mathcal{R}^n \times \mathcal{R}^m$ is a Lipschitz continuous function that is unknown. The nominal vortex control law has the form

$$\Gamma_{\mathrm{C,n}} = -K_y y + K_r r$$

where $K_y \in \mathcal{R}^{m \times m}$ and $K_r \in \mathcal{R}^{m \times r}$ are chosen such that the following reference system achieves the desired tracking characteristics

$$\dot{x}_m = A_m x_m + B_m r$$

$$y_m = C x_m \tag{B.13}$$

where $A_m = A - BK_r$ is Hurwitz and $B_m = BK_r$. For the purposes of adaptive design, assume that A_m satisfies the following Lyapunov equation

$$A_m^T P + P A_m = -Q, \quad Q = Q^T > 0, \quad Q \in \mathcal{R}^{n \times n}.$$

To introduce an adaptive signal to compensate for $f(x, \Gamma_C)$, the control effort is redefined as

$$\Gamma_C = \Gamma_{C,n} - \Gamma_{C,ad}.$$

By inserting the control law given in (B.11) into the open loop dynamics (B.12) the closed-loop dynamics can be written as

$$\begin{bmatrix} \dot{e} \\ \dot{x} \end{bmatrix} = \begin{bmatrix} 0 & C \\ -\overline{B}K_I & \overline{A} - \overline{B}K_X \end{bmatrix} \begin{bmatrix} e \\ x \end{bmatrix} + \begin{bmatrix} -1 \\ \overline{B}Z \end{bmatrix} r + \begin{bmatrix} 0 \\ \overline{B} \end{bmatrix} (-u_{ad} + \Delta(x, x_a, \Gamma_C)),$$

$$\dot{x}_a = g(x, x_a, \Gamma_C),$$

$$y = \begin{bmatrix} 0 & C \end{bmatrix} \begin{bmatrix} e \\ x \end{bmatrix}.$$

One can rewrite the closed loop system in a more compact form as

$$\dot{x} = A_m x + B_m r + B \left[\delta A \Gamma_C + \Lambda f(x, \Gamma_C) - \Gamma_{C,ad} \right].$$

We wish to approximate $\Lambda f(x, \Gamma_C)$ by a neural network. To construct such an approximation in an output feedback setting, we reconstruct the system states via delayed values of system outputs and inputs (Calise et al., 2002, Yang, 2004, Yang et al., 2004, 2003, Volyanskyy et al., 2008). If the number of delayed values for each output is s, the number of delayed values for each input is t, and

the length of the time delay time is d, the delayed value vector, $\eta(t)$, is given by

$$\eta(t) = \Big[[y_1(t), y_1(t-d), \dots, y_1(t-sd), \dots, y_m(t), y_m(t-d), \dots, y_m(t-sd)]^T ;$$

$$[\Gamma_{C,1}(t-d), \dots, \Gamma_{C,1}(t-sd), \dots, \Gamma_{C,m}(t-d), \dots, \Gamma_{C,m}(t-sd)]^T\Big] \qquad (B.14)$$

where $\eta(t) \in \mathcal{R}^w$ and $w = (s+t)m$. Note that the current control output is not included in $\eta(t)$. This is to prevent implementation issues associated with realizing the control. Using $\eta(t)$, we assume that the function $f(x, \Gamma_C)$ can be approximated over a compact set $\mathcal{D}_x \times \mathcal{D}_{\Gamma_C}$ to an arbitrary degree of accuracy such that

$$\Lambda f(x, \Gamma_C) = W^T \overline{\sigma}(V^T \eta(t)) + \epsilon(x, \Gamma_C)$$

where $\|\epsilon(x, \Gamma_C)\| < \epsilon^* < \infty$, $\overline{\sigma}(q) = [1, \ \sigma_1(q_1), \dots, \sigma_l(q_l)]$, l being the number of your hidden layer neurons, $\sigma_j(z) = 1/(1 + \exp(-z))$ and $W \in \mathcal{R}^{(l+1) \times m}$ and $V \in \mathcal{R}^{w \times l}$ are unknown but constant neural network ideal weights. The closed-loop system can then be equivalently expressed as

$$\dot{x} = A_m x + B_m r + B\left[\delta\Lambda\Gamma_C + W^T\overline{\sigma}V^T\eta - \Gamma_{C,\mathrm{ad}}\right] + B\epsilon.$$

To develop the complete output feedback algorithm an error observer must be introduced. Consider the following error observer

$$\dot{\xi} = A_m \xi + L(y - y_\xi - y_m)$$

$$y_\xi = C\xi$$

such that $\tilde{A} = A_m - LC$ is Hurwitz and satisfies the following Lyapunov equation

$$\overline{A}^T \tilde{P} + \tilde{P}\tilde{A} = -\tilde{Q}, \ \ \tilde{Q} = \tilde{Q}^T > 0, \ \ \tilde{Q} \in \mathcal{R}^{n \times n}.$$

The adaptive signal is given as

$$u_{\mathrm{ad}} = \left[I_m + \delta\hat{\Lambda} \right]^{-1} \left[\delta\hat{\Lambda} u_n + \hat{W}^T \overline{\sigma} \left(\hat{V}^T \eta(t) \right) \right]. \tag{B.15}$$

The adaptive update laws are defined as

$$\dot{\hat{W}}(t) = -\Gamma_W \mathrm{proj} \left[\hat{W}(t), \tilde{\sigma} \left(\hat{V}(t), \eta(t) \right) \xi(t)^T PB \right]$$

$$\dot{\hat{V}}(t) = -\Gamma_V \mathrm{proj} \left[\hat{V}(t), \eta(t)\xi^T PBH \left((\hat{W}(t), \hat{V}(t), \eta(t)) \right) \right] \tag{B.16}$$

$$\delta\hat{\Lambda}^T(t) = -\Gamma_\delta \mathrm{proj} \left[\delta\Lambda(t), u(t)\xi^T PB \right]$$

where

$$\tilde{\sigma} \left(\hat{V}(t), \eta(t) \right) = \overline{\sigma} \left(\hat{V}(t), \eta(t) \right) - \overline{\sigma}' \left(\hat{V}(t), \eta(t) \right) \hat{V}^T(t)\eta(t)$$

$$H \left(\hat{W}(t), \hat{V}(t), \eta(t) \right) = \hat{W}^T(t)\overline{\sigma}' \left(\hat{V}(t), \eta(t) \right) \tag{B.17}$$

and

$$\overline{\sigma}' \left(\hat{V}(t), \eta(t) \right) = \begin{bmatrix} 0 & \cdots & 0 \\ \frac{\mathrm{d}\sigma_1}{\mathrm{d}q} & \cdots & 0 \\ \vdots & \ddots & \vdots \\ 0 & \cdots & \frac{\mathrm{d}\sigma_l}{\mathrm{d}q} \end{bmatrix}$$

where q_j is the jth row of q. It is easy to show with a standard Lyapunov candidate that the adaptive weights are bounded and that the system tracking error is uniformly ultimately bounded.

The modeling error $f(x, \Gamma_{\mathrm{C}})$ is a function of unmodeled flow dynamics as well. In the absence of an analytical model for flow actuation dynamics and devices to measure the related states, we can only use measurable states in the adaptive controller. In the relatively low bandwidth maneuvers performed in our experiments, the effects of flow dynamics on rigid body dynamics are expected to be small. In addition, we also assume that such effects are observable from rigid body states. With these assumptions, the adaptive signal defined in (B.15) can be used to approximate $f(x, \Gamma_{\mathrm{C}})$.
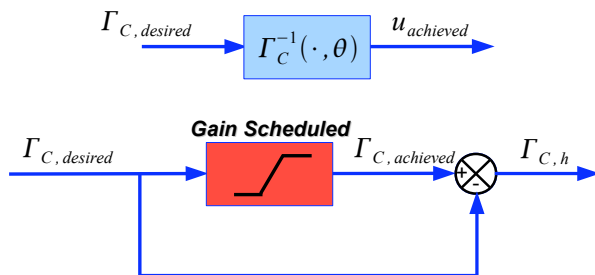
Figure B.2: Control hedging diagram.

B.2.4 Control hedging

In order to prevent adaptation effects due to control saturation, control hedging has been applied to modify the reference model (B.13). The difference between the commanded control and the control applied to the plant is defined as the hedge signal. The hedge signal is then subtracted from the input to the plant model of the reference model as shown in figure B.2. This modification effectively moves the reference model backwards by an estimate of the amount the controlled system did not move due to saturation and produces a reachable command within the capabilities of actuation. With this modification during periods of full saturation tracking error remains small, preventing winding up of the NN weights.

Applying control hedging to the adaptive vortex control algorithm here requires the hedging algorithm to be gain scheduled. The reference model is modified as

$$\dot{x}_m = A_m x_m + B_m r + B_h \Gamma_{\mathrm{C,h}}$$

where B_h is the modeled control effectiveness matrix. The hedge signal is computed as

$$\Gamma_{\mathrm{C,h}} = g(u_{\mathrm{f}}, \alpha) - \Gamma_{\mathrm{C}}$$

where $g(u_{\mathrm{f}}, \alpha)$ models the saturation limits of the actuator and Γ_{C} is the ideal control action. This process is illustrated graphically in figure B.2.

B.3 Model and control design validation

Experimental results and numerical simulations are used for verification of the model under open loop excitation as discussed in 2.3 and 2.5.4. In this section, the model developed in our previous research is used to validate control design efforts under high bandwidth, free flight conditions. Additionally, wind tunnel experiments conducted on a novel traverse capable of simulating free flight are used to further validate the control algorithms.

B.3.1 Regulating control vortex strength

The relationship between Γ_C and the input control voltage is assumed to be of the form $\Gamma_C = \Gamma_C(u, \alpha)$. This results in a system model of the form

$$\dot{\bar{x}} = \overline{A}\bar{x} + \overline{B}\Gamma_C(u, \alpha).$$

For control, if Γ_C is invertible in terms of u, then the system can be inverted as well. This is the case for the simple structure of $\Gamma_C(u, \alpha)$ presented in figure 2.16. It can be seen that both the control voltage can saturate and the magnitude of Γ_C can saturate. When the input voltage increases above a point, Γ_C no longer increases in magnitude (it indicates control reversal). If the control is restricted, the curve for fixed α is monotonic on a compact set which implies invertibility over the restricted domain. It is also seen that depending on α, the maximum and minimum Γ_C shrinks in magnitude. Therefore, there is an angle of attack saturation dependence. This information is used to develop the following feedback linearization strategy:

- Use control law formulation to compute required Γ_C.

- Use interpolation over α to determine $[\max\{\Gamma_C\}, \min\{\Gamma_C\}]$ If Γ_C is achievable, compute the corresponding control voltage. If not, apply the *best* control voltage possible and appropriate control hedge signal.
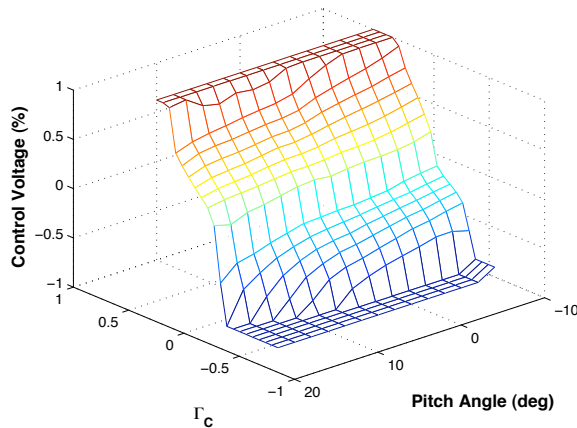
Figure B.3: Γ_C with control voltage saturation limits.

This strategy can be realized in a lookup table and precomputed. This precomputed lookup table is shown in figure B.3 where the inverse map is saturated. Note that since Γ_C is a continuous signal, the corresponding control voltage will also be continuous.

B.3.2   Experimental results

The control strategy for the experiments is as follows. First, the traverse is operated in position control mode where a tracking control design is used to drive the model to a desired position and attitude. Then position control is transferred to the flow actuator loop while the traverse is switched to the force control mode. In this mode, the traverse maintains the forcing derived from the required system dynamic properties while the outer loop controller, based on the control laws described previously, forces the modified dynamics of the wing model to track the given reference trajectory. A variable force is applied to the model via the force control law to remove only the effect of gravity and friction. The outer loop control design assumes that ideal force tracking is achieved in the plunge axis and makes no account for the presence of the traverse. This assumption has proved suffcient in Muse et al. (2008b). It is also assumed that rigid body state information is available consisting of vertical position, pitch attitude, and their derivatives. State estimation is achieved using a Kalman filter to blend sensed angular position and angular acceleration in the pitch axis, and by differentiation, of sensed vertical positions in plunge. The flow state is unknown

in all designs.

Simulating free flight

Force control is a technique commonly used in robotics to control the position of a manipulator and its applied force. Here we control the forces and moments that are applied to a wind tunnel model in order to simulate the complete longitudinal dynamics of an arbitrary aircraft configuration. The techniques used in this application are different than those used in robotics because the force must be applied on a system while in motion and the control system must restrict the model to stay in the longitudinal plane regardless of the commanded and applied disturbance forces on the plunge axis. The control objective is achieved by manipulating the forces applied by two servo driven ball screws and the moment applied by a servo motor in the pitch axis. Applying a prescribed force to the model is difficult due to the large mass and high friction of the linear drives in relation to the model. The limitations in force control arise from the lack of compliance between the model and the linear actuator. Having a stiff coupling between the actuator and the point of force application can cause a chattering effect. This is due to a large stiffness at the force measurement point. Furthermore, a stiff coupling results in poor force tracking. This is due to the actuators not being able to respond quickly enough to maintain an acceptable level in force tracking error. To overcome these limitations, linearly compliant springs are mounted between the model and each ball screw carriage as shown in figure B.4. The contact force between the actuator and the model can then be precisely regulated through control of the spring deflections.

In order to study aircraft flight in a wind tunnel on a traverse heavy enough to carry all of the support and measurement equipment, the control system must serve three fundamental purposes: removing the effect of the high traverse mass, modifying the stability characteristics of the model, and restricting the motion of the traverse to the longitudinal plane. To meet these requirements, a three-loop control architecture is used. This consists of the carriage control loop, the force control loop, and the stability modification loop. A distinguishing feature of the latter loop is the ability to actively compensate for the effect of the center of gravity offset from the model pivot. A full
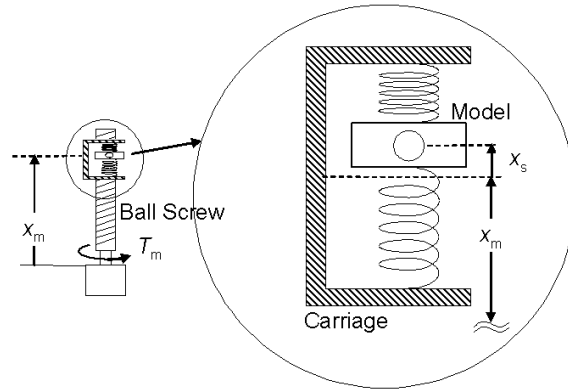
Figure B.4: Diagram illustrating how the spring system interfaces to the wind tunnel model.

description of the force tracking control law used here is described in Muse et al. (2008b).

Results

In this section we present typical results from application of the control designs described previously. All linear control designs are tuned to have a theoretical response that is similar in behavior. We fixed the overshoot and required the response to have the same shape. To evaluate improvements in performance, we slowly decreased the response rise time until each model failed. Each model is tuned based solely on the linear design model. No further tuning is performed. Figure B.5 illustrates the behavior of the static model using a torque motor to simulate the assumed response of the actuators. The torque motor output is scaled to have the same control effectiveness as the measured actuator gain. The same control gains and are used to control the model. As seen in the figure the response closely matches the expected ideal response. Hence, the traverse is functioning as expected. Figure B.6 compares the response of the vortex model based linear control design to a control design using the static model for a rise time of 0.39 seconds (rise time is defined as 10 percent to 90 percent os the final command). The gains for the static model based control law are the same ones used for the torque motor in figure B.5. The linear control law in this case exhibits a limit cycle type behavior that does not decay. However, the vortex model response remains quite close to the ideal response. In figure B.7, the bandwidth of the nominal vortex control law is increased further, in this case the system rise time is 0.19 sec. The vortex model seems to be stable but suddenly loses
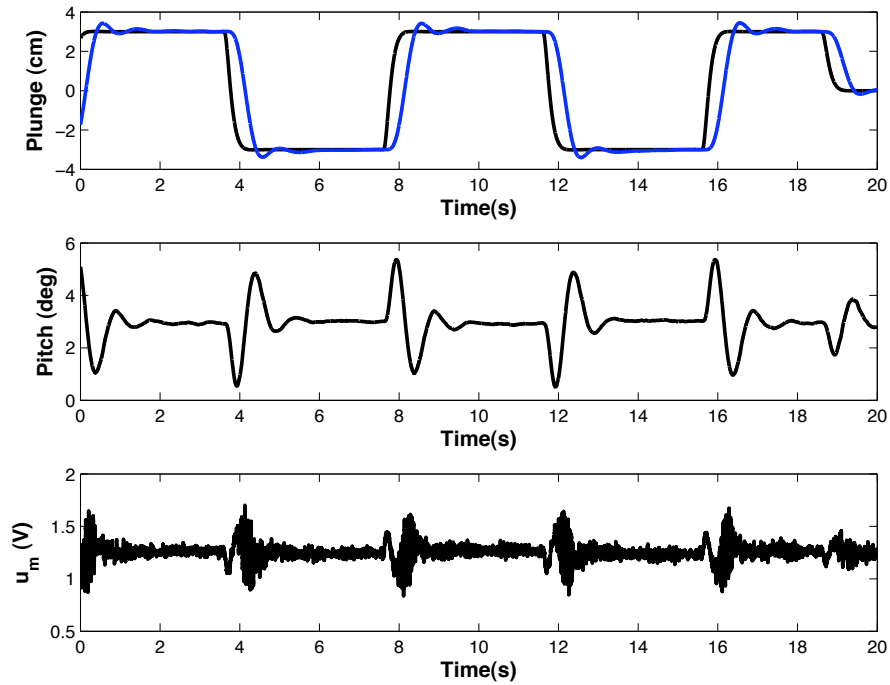
Figure B.5: Verification that the static model models response with torque motor accurately. Top: ——, command signal; ——, experimental response.

stability. However, the adaptive control law is able to maintain stable ideal tracking. Figure B.8 gives a visual comparison between the responses of the each design at the limit of each models' closed loop performance.

B.4 Conclusion

A novel low-order model is developed to facilitate flight control design using synthetic jets. To the authors' knowledge, this is the first model developed for control design that is based solely on first principles based modeling. Though the model used for a linear control design helps achieve higher control bandwidths than achievable with conventional modeling assumptions, as the control bandwidth increases, the nonlinearities in the flow become large requiring adaptive control methods to maintain tracking performance and stability. The adaptive architecture uses a single hidden layer neural network with delayed system output and control values to observe and compensate for the unmodeled system dynamics and nonlinearities. Control designs are verified on a novel wind tunnel

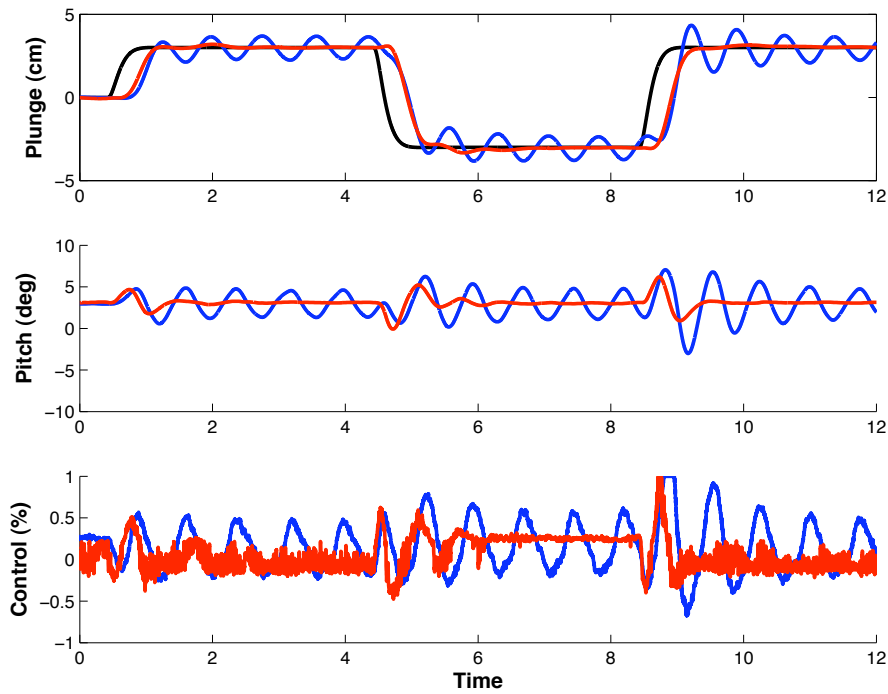Figure B.6: Comparison between the vortex model and static model when the static model assumption fails. ——, command signal; ——, static model; ——, vortex model.
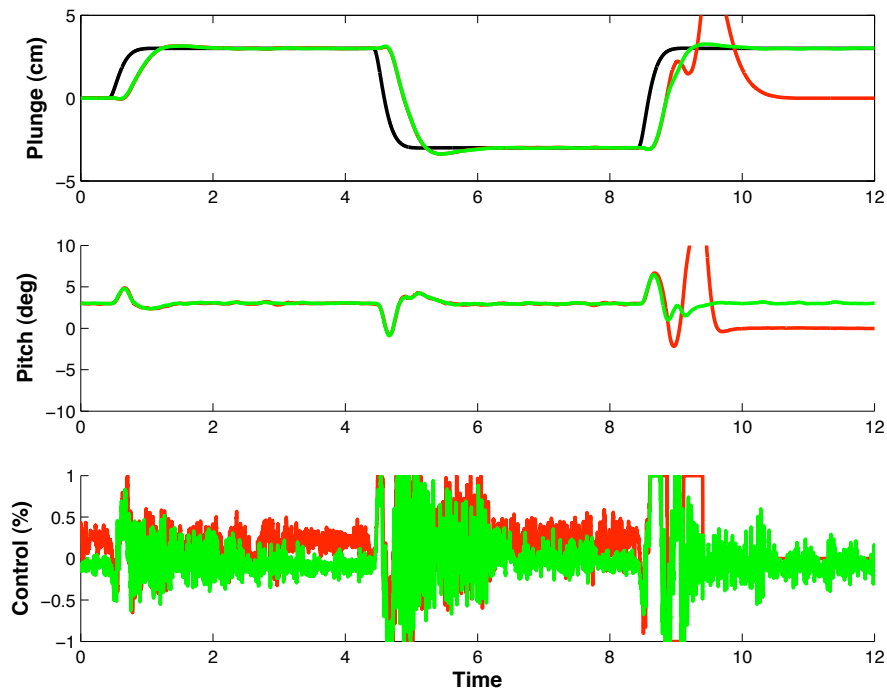

Figure B.7: Comparison between vortex model and adaptive control law when the vortex model fails. ——, vortex model; ——, adaptive control.
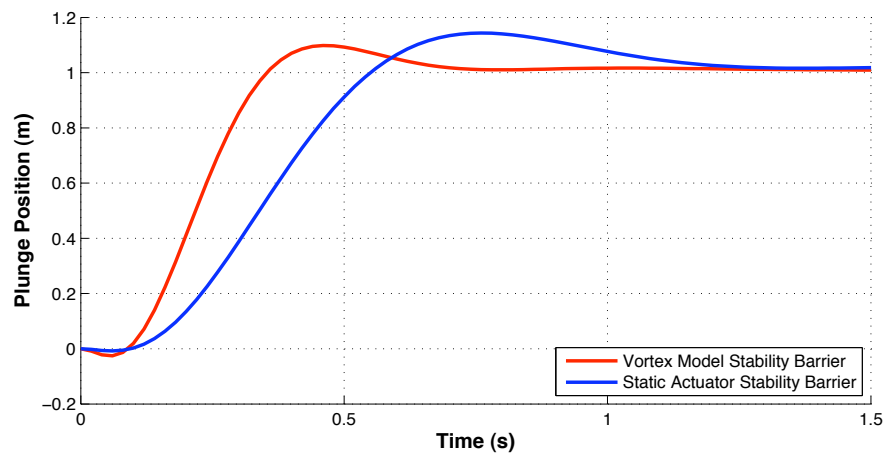
Figure B.8: Comparison of the rise time stability barriers.

traverse capable of simulating free flight in a wind tunnel.

Appendix C

Example translation and rotation potentials

Here we find forms of the potential W_t, W_r satisfying Equations (3.3) and (3.5). Consider conformal transformations of the form

$$z = z_0 + \mathrm{e}^{i\theta} g(\zeta). \tag{C.1}$$

For any general $g(\zeta)$ such that $g(\zeta) \sim \zeta$ as we approach $\zeta = \infty$, we must enforce the boundary condition on the surface as well as satisfy the condition at infinity that the potential is at most a constant. Thus we have the boundary condition

$$\mathrm{Im}\,[W_\mathrm{t}] = \mathrm{Im}\,\left[\dot{\bar{z_0}}\,(z - z_0)\right]$$

$$= \mathrm{Im}\,\left[\dot{\bar{z}}_0\,\mathrm{e}^{i\theta} g(\zeta)\right] \tag{C.2}$$

where a constant has been added to Equations (3.2). Let us denote the term in (C.2) as $U = -\dot{\bar{z_0}}\,\mathrm{e}^{i\theta}$. Here we have a Schwarz problem and can use Cauchy's integral formula and perform a complex integration to determine a general form for the potential. As an alternative, we note that the function inside the square brackets, $-Ug(\zeta)$, is well behaved and a good candidate for the function except that the potential does not decay at infinity as the boundary conditions require. Thus we

use the following trick: by adding a linear term $U\zeta$ to $-Ug(\zeta)$ we have

$$\text{Im}\left[W_\text{t}\right] = \text{Im}\left[-U\left(g(\zeta) - \zeta\right) + \frac{a^2}{\zeta}\overline{U}\right]$$

where we have used the geometric relation $\text{Im}\left[-U\zeta\right] = \text{Im}\left[\overline{U}a^2/\zeta\right]$. We can now simply equate

$$W_\text{t} = U\left(\zeta - g(\zeta)\right) + \frac{a^2}{\zeta}\overline{U}$$

since it satisfies both the boundary condition on the body's surface as well as the condition at infinity. This is true for any transformation $g(\zeta)$ as long as $g(\zeta) = \zeta + \mathcal{O}\left(1\right)$.

Rotational potential is more difficult to deal with and no single formula can be derived for a general form of $g(\zeta)$ that satsifies the aforementioned conditions. We point out two examples in literature where the rotational potential has been determined for a class of $g(\zeta)$. One special case of interest are the Joukowski airfoil forms (including the flat plate transformation), i.e.

$$g(\zeta) = \zeta + \zeta_c + \frac{b^2}{\zeta + \zeta_c}.$$

Streitlien (1994) used the well-known circle theorem to derive the rotational potential (Milne-Thomson, 1968). The potential for this form is given by

$$W_\text{r} = -i\,\Omega\left(\frac{\zeta_c a^2}{\zeta} + \frac{b^2 a^2 - \overline{\zeta_c}\zeta}{\zeta(\zeta + \zeta_c)} + \frac{b^4\zeta_c}{(a^2 + |\zeta_c|^2)(\zeta + \zeta_c)}\right)$$

where $a = |b - \zeta_c|$ and the complex parameter ζ_c and real parameter b control the camber and thickness of the airfoil. For the special case of a flat plate, $b = a$ and $\zeta_c = 0$ thus the rotational potential reduces to

$$W_\text{r} = -\frac{i\Omega a^4}{\zeta^2}.$$

Furthermore, as another example, Michelin (2009) takes a look at

$$g(\zeta) = \sum_{j=-1}^{M} \frac{G_j}{\zeta^j}$$

where $G_{-1} = 1$. The rotational potential for this case has the form

$$W_{\mathrm{r}} = i\Omega \sum_{l=0}^{M+1} \frac{R_l}{\zeta^l}, \text{ where } R_l = \sum_{k=-1}^{M-l} \frac{\overline{G_k} G_{k+l}}{a^{2k}}.$$

Appendix D

Details on integrating the two body FSI problem

Care must be taken when numerically integrating the coupled FSI problems presented in (4.20) and (4.21). For example, in (4.20) we cast the equations in the following form

$$\frac{\mathrm{d}P_k}{\mathrm{d}t} = G_k, \tag{D.1a}$$

$$\frac{\mathrm{d}z_k}{\mathrm{d}t} = U_k \tag{D.1b}$$

where

$$P_k = (\varrho_b - \varrho_f)A_k U_k - i\varrho_f \oint_{|\zeta|=\rho_k} z(\zeta)\frac{\mathrm{d}w}{\mathrm{d}\zeta} \, \mathrm{d}\zeta, \tag{D.2a}$$

$$G_k = \overline{\frac{i\varrho_f}{2} \oint_{|\zeta|=\rho_k} \left(\frac{\mathrm{d}w}{\mathrm{d}\zeta}\right)^2 \left(\frac{\mathrm{d}z}{\mathrm{d}\zeta}\right)^{-1} \mathrm{d}\zeta}. \tag{D.2b}$$

The integrals represented in (D.2) are implicitly functions of the physical variables $z_1(t)$, $z_2(t)$, $U_1(t)$, and $U_2(t)$. One can integrate (D.1) with any adequate time-integrator but it must be ensured that the term (D.2a) is satisfied. To do so, one must solve (D.2a) for a suitable U_k, e.g. via Newton iterations, for the use in (D.2b) and subsequently in (D.1).

Bibliography

Abbott, I. and Deonhoff, A., 1959. *Theory of Wing Sections*. Dover Publications, Inc.

Akhiezer, N., 1990. *Elements of the Theory of Elliptic Functions*, volume 79 of *Translation of Mathematical Monographs*. Providence: American Mathematical Society.

Alassar, R. S. and El-Gebeily, M. A., 2009. Inviscid flow past two cylinders. *Journal of Fluids Engineering-Transactions of the ASME*, 131(5).

Alben, S., 2008. An implicit method for coupled flow-body dynamics. *Journal of Computational Physics*, 227(10):4912–4933.

Amitay, M., 2000. Images on formation of synthetic jets.

Amitay, M. and Glezer, A., 2002. Role of actuation frequency in controlled flow reattachment over a stalled airfoil. *AIAA Journal*, 40(2):209–216.

Bampalas, N. and Graham, J. M. R., 2008. Flow-induced forces arising during the impact of two circular cylinders. *Journal of Fluid Mechanics*, 616:205–234.

Benaroya, H. and Gabbai, R. D., 2008. Modelling vortex-induced fluid-structure interaction. *Philosophical Transactions of the Royal Society A-Mathematical Physical and Engineering Sciences*, 366(1868):1231–1274.

Bisplinghoff, R. L., Ashley, H., and Halfman, R. L., 1955. *Aeroelasticity*. Reading, MA: Wesley Publishing Company, Inc.

Borazjani, I., Ge, L., and Sotiropoulos, F., 2008. Curvilinear immersed boundary method for simulating fluid structure interaction with complex 3d rigid bodies. *Journal of Computational Physics*, 227:7587–7620.

Borazjani, I., Ge, L., and Sotiropoulos, F., 2010. High-resolution fluid-structure interaction simulations of flow through a bi-leaflet mechanical heart valve in an anatomic aorta. *Annals of Biomedical Engineering*, 38(2).

Borisov, A. V., Mamaev, I. S., and Ramodanov, S. M., 2005. Dynamics of a circular cylinder interacting with point vortices. *Discrete and Continuous Dynamical Systems-Series B*, 5(1):35–50.

Borisov, A. V., Mamaev, I. S., and Ramodanov, S. M., 2007a. Dynamic interaction of point vortices and a two-dimensional cylinder. *Journal of Mathematical Physics*, 48(6).

Borisov, A. V., Mamaev, I. S., and Ramodanov, S. M., 2007b. Dynamics of two interacting circular cylinders in perfect fluid. *Discrete and Continuous Dynamical Systems*, 19(2):235–253.

Brown, C. E. and Michael, W. H., 1954. Effect of leading-edge separation on the lift of a delta-wing. *Journal of the Aeronautical Sciences*, 21(10):690–&.

Bryson, A. E., 1959. Symmetric vortex separation on circular cylinders and cones. *Journal of Applied Mechanics*, pages 643–648.

Brzozowski, D., 2009. Rapid modification of the flow field about a free moving airfoil by controlled, trapped vorticity concentrations. In *5th AIAA Flow Control Conference*.

Calise, A. J., Yang, B. J., and Craig, J. I., 2002. Augmentation of an existing linear controller with an adaptive element. In *Proceedings of the American Control Conference*.

Cheng, H. K., 1954. Remarks on nonlinear lift and vortex separation. *Journal of the Aeronautical Sciences*, 21(3):212–214.

Clements, R. R., 1973. An inviscid model of two-dimensional vortex shedding. *Journal of Fluid Mechanics*, 57:321–336.

Cortelezzi, L., 1992. A theoretical and computational study on active wake control. Ph.D. thesis.

Cortelezzi, L., 1995. On the unsteady separated flow past a semiinfinite plate - exact solution of the brown-and-michael model, scaling, and universality. *Physics of Fluids*, 7(3):526–529.

Cortelezzi, L., 1996. Nonlinear feedback control of the wake past a plate with a suction point on the downstream wall. *Journal of Fluid Mechanics*, 327:303–324.

Cortelezzi, L. and Leonard, A., 1993. Point vortex model of the unsteady separated flow past a semiinfinite plate with transverse motion. *Fluid Dynamics Research*, 11(6):263–295.

Cortelezzi, L., Leonard, A., and Doyle, J. C., 1994. An example of active circulation control of the unsteady separated flow past a semiinfinite plate. *Journal of Fluid Mechanics*, 260:127–154.

Crighton, D. G., 1985. The kutta condition in unsteady-flow. *Annual Review of Fluid Mechanics*, 17:411–445.

Crowdy, D., 2008. Conformal mappings from annuli to canonical doubly connected bell representations. *Journal of Mathematical Analysis and Applications*, 340(1):669–674.

Crowdy, D., 2009. The spreading phase in lighthill's model of the Weis-Fogh lift mechanism. *Journal of Fluid Mechanics*, 641:195–204.

Crowdy, D., 2010. A new calculus for two-dimensional vortex dynamics. *Theoretical and Computational Fluid Dynamics*, 24:9–24.

Crowdy, D. and Marshall, J., 2006. Conformal mappings between canonical multiply connected domains. *Computational Methods and Function Theory*, 6(1):59–76.

Crowdy, D. G., Surana, A., and Yick, K. Y., 2007. The irrotational motion generated by two planar stirrers in inviscid fluid. *Physics of Fluids*, 19(1).

DeSalvo, M. and Glezer, A., 2004. Aerodynamic performance modification at low angles of attack by trailing edge vortices.

DeSalvo, M. and Glezer, A., 2005. Airfoil aerodynamic performance modifications using hybrid surface actuators.

Edwards, J. W., Ashley, H., and Breakwell, J. V., 1979. Unsteady aerodynamic modeling for arbitrary motions. *AIAA Journal*, 17(4):365–374.

Edwards, R. H., 1954. Leading-edge separation from delta-wings. *Journal of the Aeronautical Sciences*, 21(2):134–135.

Eldredge, J. D. and Pisani, D., 2008. Passive locomotion of a simple articulated fish-like system in the wake of an obstacle. *Journal of Fluid Mechanics*, 607:279–288.

Eloy, C., Souilliez, C., and Schouveiler, L., 2007. Flutter of a rectangular plate. *Journal of Fluids and Structures*, 23(6):904–919.

Furber, S. B. and Ffowcswilliams, J. E., 1979. Is the Weis-Fogh principle exploitable in turboma-chinery. *Journal of Fluid Mechanics*, 94:519–540.

Gabbai, R. D. and Benaroya, H., 2005. An overview of modeling and experiments of vortex-induced vibration of circular cylinders. *Journal of Sound and Vibration*, 282(3-5):575–616.

Garrick, I. E., 1936. Propulsion of a flapping and oscillating airfoil. Technical report, NACA.

Glauert, H., 1929. The force and moment on an oscillating aerofoil. Technical report.

Glezer, A., 2005. Fluidic-based virtual aerosurface shaping.

Glezer, A. and Amitay, M., 2002. Synthetic jets. *Annual Review of Fluid Mechanics*, 34:1–36.

Goluzin, G. M., 1969. *Geometric Theory of Functions of a Complex Variable*. Providence, RI: American Mathematical Society.

Graham, J. M. R., 1980. The forces on sharp-edged cylinders in oscillatory flow at low keulegan–carpenter numbers. *Journal of Fluid Mechanics*, 97:331–346.

Graham, J. M. R., 1983. The lift on an aerofoil in starting flow. *Journal of Fluid Mechanics*, 133:413–425.

Greenblatt, D. and Wygnanski, I. J., 2000. The control of flow separation by periodic excitation. *Progress in Aerospace Sciences*, 36(7):487–545.

Jones, K. D., Bradshaw, C. J., Papadopoulos, J., and Platzer, M. F., 2005. Bio-inspired design of flapping-wing micro air vehicles. *Aeronautical Journal*, 109(1098):385–393.

Jones, M. A., 2003. The separated flow of an inviscid fluid around a moving flat plate. *Journal of Fluid Mechanics*, 496:405–441.

Jones, R. T., 1938. Operational treatment of the nonuniform-lift theory in airplane dynamics. Technical report.

Kanso, E., Marsden, J. E., Rowley, C. W., and Melli-Huber, J. B., 2005. Locomotion of articulated bodies in a perfect fluid. *Journal of Nonlinear Science*, 15(4):255–289.

Kanso, E. and Newton, P. K., 2009. Passive locomotion via normal-mode coupling in a submerged spring-mass system. *Journal of Fluid Mechanics*, 641:205–215.

Kassner, R. and Fingado, H., 1936. Das ebene problem der fluügelschwingung. *Luftfahrtforsch*, 13(11).

Kiya, M. and Arie, M., 1977. Contribution to an inviscid vortex-shedding model for an inclined flat-plate in uniform-flow. *Journal of Fluid Mechanics*, 82(SEP7):223–&.

Klamo, J. T., 2007. Effects of damping and reynolds number on vortex-induced vibrations. Ph.D. thesis.

Küssner, H. G., 1936. Zusammenfassender bericht über den instationären auftrieb von flügeln. *Luftfahrtforsch*, 13(12).

Kutay, A. T., Calise, A. J., and Muse, J. A., 2006. A 1-DOF wind tunnel experiment in adaptive flow control. In *AIAA Guidance, Navigation, and Control Conference*.

Lagally, M., 1929. Die reibungslose stromung im aubengebiet zweier kreise. *Zeitschrift Fur Angewandte Mathematik Und Mechanik*, 9:299–305.

Lamb, H., 1945. *Hydrodynamics*. New York: Dover Publications, Inc.

Landweber, L. and Shahshahan, A., 1991. Added masses and forces on two bodies approaching central impact in an inviscid fluid. Technical report, Iowa Institute of Hydraulic Research.

Leonard, A. and Roshko, A., 2001. Aspects of flow-induced vibration. *Journal of Fluids and Structures*, 15:415–425.

Lewin, G. C. and Haj-Hariri, H., 2005. Reduced-order modeling of a heaving airfoil. *AIAA Journal*, 43(2):270–283.

Lighthill, M. J., 1973. Weis-Fogh mechanism of lift generation. *Journal of Fluid Mechanics*, 60(AUG21):1–17.

Lopez, O., 2009. Computational study of a NACA4415 airfoil using synthetic jet control. Ph.D. thesis.

Michelin, S., 2009. Falling, flapping, flying, swimming,...: high-Re fluid-solid interactions with vortex shedding. Ph.D. thesis.

Michelin, S. and Smith, S. G. L., 2009a. Resonance and propulsion performance of a heaving flexible wing. *Physics of Fluids*, 21(7).

Michelin, S. and Smith, S. G. L., 2009b. An unsteady point vortex method for coupled fluid-solid problems. *Theoretical and Computational Fluid Dynamics*, 23(2):127–153.

Michelin, S., Smith, S. G. L., and Glover, B. J., 2008. Vortex shedding model of a flapping flag. *Journal of Fluid Mechanics*, 617:1–10.

Milne-Thomson, L., 1968. *Theoretical Hydrodynamics*. New York: Dover Publications, 5th edition.

Mittal, R. and Iaccarino, G., 2005. Immersed boundary methods. *Annual Review of Fluid Mechanics*, 37:239–261.

Muse, J., Kutay, A., Brzozowski, D., Culp, J., Calise, A., and Glezer, A., 2008a. Dynamic flight maneuvering using trapped vorticity flow control.

Muse, J., Kutay, A., and Calise, A., 2008b. Novel force control traverse for simulating UAV flight in wind tunnel.

Muse, J. A., Tchieu, A. A., Kutay, A. T., Chandramohan, R., Calise, A. J., and Leonard, A., 2009. Vortex model based adaptive flight control using synthetic jets. In *AIAA Guidance, Navigation, and Control Conference.* Chicago, Illinois: AIAA.

Muskhelishvili, N., 1953. *Singular Integral Equations.* New York: Dover Publications, 2nd edition.

Nair, S. and Kanso, E., 2007. Hydrodynamically coupled rigid bodies. *Journal of Fluid Mechanics*, 592:393–411.

Naudascher, E. and Rockwell, D., 1994. *Flow-Induced Vibrations, An Engineering Guide.* A.A. Balkema Publishers.

Newman, J. N., 1977. *Marine Hydrodynamics.* Cambridge: The MIT Press.

Peskin, C. S., 1972. Flow patterns around heart valves: a numerical method. *Journal of Computational Physics*, 10:252–271.

Peters, D. A., 2008. Two-dimensional incompressible unsteady airfoil theory - an overview. *Journal of Fluids and Structures*, 24(3):295–312.

Petz, R. and Wolfgang, R., 2006. Active control of seperation on two and three-dimensional high lift configurations. In *25th International Congress of the Aeronautical Sciences.*

Pullin, D. I., 1978. Large-scale structure of unsteady self-similar rolled-up vortex sheets. *Journal of Fluid Mechanics*, 88(OCT):401–430.

Ramodanov, S. M., 2002. Motion of a circular cylinder and n point vortices in a perfect fluid. *Regular & Chaotic Dynamics*, 7(3):291–298.

Roenby, J. and Aref, H., 2010. Chaos in body-vortex interactions. *Proceedings of the Royal Society A: Mathematical, Physical and Engineering Science*, pages 1–21.

Rott, N., 1956. Diffraction of a weak shock with vortex generation. *Journal of Fluid Mechanics*, 1(1):111–128.

Saff, E. and Snider, A., 2003. *Fundamentals of Complex Analysis.* Upper Saddle River, New Jersey: Prentice Hall, third edition edition.

Saffman, P. G., 1992. *Vortex Dynamics.* Cambridge University Press.

Sarpkaya, T., 1975. An inviscid model of two-dimensional vortex shedding for transient and asymptotically steady separated flow over an inclined plate. *Journal of Fluid Mechanics*, 68:109–128.

Sarpkaya, T. and Schoaff, R. L., 1979. Inviscid model of 2-dimensional vortex shedding by a circular-cylinder. *AIAA Journal*, 17(11):1193–1200.

Sears, W. R., 1941. Some aspects of non-stationary airfoil theory and its practical applications. *Journal of the Aeronautical Sciences*, 8(3):104–108.

Sedov, L., 1965. *Two-Dimensional Problems in Hydrodynamics and Aerodynamics.* New York: John Wiley and Sons, Inc.

Shashikanth, B. N., 2005. Poisson brackets for the dynamically interacting system of a 2d rigid cylinder and n point vortices: The case of arbitrary smooth cylinder shapes. *Regular & Chaotic Dynamics*, 10(1):1–14.

Shukla, R. K. and Eldredge, J. D., 2007. An inviscid model for vortex shedding from a deforming body. *Theoretical and Computational Fluid Dynamics*, 21(5):343–368.

Smith, B. L. and Glezer, A., 1998. The formation and evolution of synthetic jets. *Physics of Fluids*, 10(9):2281–2297.

Streitlien, K., 1994. Extracting energy from unsteady flows through vortex control. Ph.D. thesis.

Taira, K. and Colonius, T., 2007. The immersed boundary method: A projection approach. *Journal of Computational Physics*, 225(2):2118–2137.

Tchieu, A. A., Leonard, A., Kutay, A. T., Muse, J. A., and Calise, A. J., 2008. Validation of a low-order model for closed-loop flow control enable flight. In *4th AIAA Flow Control Conference.*

Theodorsen, T., 1935. General theory of aerodynamic instability and the mechanism of flutter. Technical report.

Triantafyllou, M. S. and Triantafyllou, G. S., 1995. An efficient swimming machine. *Scientific American*, 272(3):64–70.

Volyanskyy, K. Y., Haddad, W. M., and Calise, A. J., 2008. A new neuroadaptive control architecture for nonlinear uncertain dynamical systems: Beyond and E-modifications. In *47th IEEE Conference on Decision and Control.*

von Kármán, T. and Edson, L., 1967. *The Wind and Beyond, Theodore von Kármán, Pioneer in Aviation and Pathfinder in Space.* Little, Brown and Co.

von Kármán, T. and Sears, W. R., 1938. Airfoil theory for non-uniform motion. *Journal of the Aeronautical Sciences*, 5(10):379–390.

Wagner, H., 1925. Concerning the dynamic ascending force formation of aeorofoils. *Zeitschrift Fur Angewandte Mathematik Und Mechanik*, 5:17–35.

Wang, Q. X., 2004. Interaction of two circular cylinders in inviscid fluid. *Physics of Fluids*, 16(12):4412–4425.

Wang, Z. J., 2000. Vortex shedding and frequency selection in flapping flight. *Journal of Fluid Mechanics*, 410:323–341.

Wang, Z. J. and Russell, D., 2007. Effect of forewing and hindwing interactions on aerodynamic forces and power in hovering dragonfly flight. *Physical Review Letters*, 99(14).

Weihs, D., 2004. The hydrodynamics of dolphin drafting. *Journal of Biology*, 3(2):8.

Williamson, C. H. K. and Govardhan, R., 2004. Vortex-induced vibrations. *Annual Review of Fluid Mechanics*, 36:413–455.

Wise, K. A., 2007. A trade study on missile autopilot design using optimal control theory. In *AIAA Guidance, Navigation and Control Conference and Exhibit*. Hilton Head, South Carolina, USA.

Wu, J. Z., Lu, X. Y., Denny, A. G., Fan, M., and Wu, J. M., 1998. Post-stall flow control on an airfoil by local unsteady forcing. *Journal of Fluid Mechanics*, 371:21–58.

Yang, B. J., 2004. Adaptive output feedback control of flexible systems. Ph.D. thesis.

Yang, B. J., Calise, A. J., and Craig, J. I., 2003. Adaptive output feedback control with input saturation. In *Proceedings of the American Control Conference*.

Yang, B. J., Calise, A. J., and Craig, J. I., 2004. Adaptive output feedback control of a flexible base manipulator. In *AIAA Guidance, Navigation, and Control Conference*.